

**DESIGN & FABRICATION OF ORGANIC PHOTOVOLTAIC  
DEVICES**



**DESIGN, FABRICATION & CHARACTERIZATION OF ORGANIC  
PHOTOVOLTAIC DEVICES**

by

AVERY P. YUEN, B.Eng.Mgt.

A Thesis

Submitted to the School of Graduate Studies

in Partial Fulfilment of the Requirements

for the Degree

Doctor of Philosophy

McMaster University

©Copyright by Avery P. Yuen, 2010.

DOCTOR OF PHILOSOPHY (2010)  
(Dept. of Engineering Physics)

McMaster University  
Hamilton, Ontario

TITLE: Design, Fabrication & Characterization of Organic Photovoltaic Devices

AUTHOR: Avery P. Yuen, B.Eng.Mgt. (McMaster)

SUPERVISOR: Dr. Rafik O. Loutfy & Dr. John S. Preston

NUMBER OF PAGES: xviii, 145

# Abstract

In this thesis, several methods of material integration into organic photovoltaic devices are investigated by fabricating solution processed and vacuum coated devices. Each of these methods is aimed at examining and improving one or more of the four critical factors that determine solar cell efficiency: (1) photovoltage, (2) light absorption, (3) exciton separation, and (4) charge collection. To investigate and improve photovoltage, the photovoltaic properties of different M-Phthalocyanine/Fullerene (M-Pc/C<sub>60</sub>) blends are measured and demonstrate an improved open circuit voltage ( $V_{oc}$ ) using trivalent-metal phthalocyanine. Rubrene is also added to the M-Pc/C<sub>60</sub> cells and shown to systematically increase the  $V_{oc}$ . To improve light absorption, two new device structures are developed: the parallel tandem cell and the heteromorphic cell. The parallel tandem cell is demonstrated using both all-vacuum coated materials as well as a combination of vacuum and solution processed materials. Results show definitive and significant current contribution from the near-infrared (NIR) wavelengths, and concomitant increase in photocurrent and power conversion efficiency (PCE). The heteromorphic cell demonstrates the integration of two polymorphs of the same M-Pc, yielding a broader external quantum efficiency (EQE) spectrum in the NIR region and an increase in the overall PCE. To investigate exciton separation and charge collection, time of flight photoconductivity studies are performed on varying compositions of solution processed polymer/fullerene films as well as pristine and blended M-Pc:C<sub>60</sub> films. Results verify the necessity for balanced carrier transport in blended systems, and the importance of carrier mobility for achieving high fill factors. Finally, the stability of a relatively new polythiophene (PQT-12) in an organic solar cell is investigated, and shown to significantly increase the device lifetime as compared to the standard P3HT polymer.

# Acknowledgements

I would like to gratefully acknowledge the following for their help and support, not just during the time this thesis was written but during my entire time at McMaster:

To my supervisors, Ah-Mee Hor, John Preston, and Rafik Loutfy, for providing me with the opportunity to work freely and for providing me guidance in my project and career. Many thanks for your years of help.

To the Xerox Research Centre of Canada and its staff, especially Vlad Skorokhod and Giuseppa Baranyi, for providing me with invaluable lab space, resources, and advice on my project. This project would not have been possible without XRCC.

To Agilent Technologies, the Natural Sciences and Engineering Research Council of Canada, and the Ontario Centres of Excellence, for providing financial assistance that allowed me to live and work.

To my excellent colleagues, Nathan Bamsey and Richard Klenkler, for fruitful discussions, ideas, advice, and listening to my rants about football.

To my summer students, Stephen Jovanovic and Kent Fisher, for doing the dirty work that not even a graduate student wants to do. *Gratias vobis ago. Labor omnia vincit. haec olim meminisse iuvabit.*

To my parents, Peter & Agnes, for encouraging my scientific curiosity at a young age, and for always believing in me and supporting me. Thank you for the many sacrifices you have made so that I could be successful. *doh jeh sai.*

To my brother, Conrad, for always looking out for me and providing the answers that only a big brother could give.

To all my friends, especially Sean Hurley and Darryl Wallace, for providing me an escape from work, and for constant encouragement in times I needed it most.

And finally, to the staff at the Westdale Café and Second Cup, for allowing me to work countless hours over the past 4 years for only an occasional \$2 purchase.

*To my family, for their unwavering support.*

# Table of Contents

<b>Abstract</b>	<b>iii</b>
<b>Acknowledgements</b>	<b>iv</b>
<b>List of Figures</b>	<b>x</b>
<b>List of Tables</b>	<b>xiii</b>
<b>List of Abbreviations</b>	<b>xiv</b>
<b>Preface</b>	<b>xvi</b>
<b>1 Introduction &amp; Theory</b>	<b>1</b>
1.1 History & Motivation . . . . .	1
1.2 Photovoltaic Theory . . . . .	3
1.2.1 Current-Voltage Response . . . . .	4
1.2.2 External Quantum Efficiency . . . . .	6
1.3 Design Considerations for PV devices . . . . .	7
1.4 Organic vs. Inorganic Semiconductors . . . . .	8
1.4.1 Weak vs. Strong Bonding . . . . .	8
1.4.2 Long Range Order . . . . .	11
1.5 Organic PV Devices and Fabrication . . . . .	12
1.5.1 Difference between Organic and Inorganic PV . . . . .	12
1.5.2 Method of Operation & OPV Design . . . . .	13
1.5.3 Solution Processed Materials & Fabrication . . . . .	16
1.5.4 Vacuum Coated Materials & Fabrication . . . . .	20
1.5.5 Pre and Post Production Considerations . . . . .	22
1.6 Current Challenges & Research . . . . .	23
1.6.1 Spectral Mismatch & Low Band Gap Materials . . . . .	24
1.6.2 Hybrid Structures . . . . .	25
1.6.3 Tandem Structures . . . . .	25
1.6.4 Degradation & Long Term Stability . . . . .	27

1.6.5	Large Area Uniformity . . . . .	28
1.6.6	Economic Challenges & Balance of System . . . . .	28
1.7	Thesis Objectives & Scope . . . . .	29
<b>2</b>	<b>Equipment &amp; Characterization</b>	<b>32</b>
2.1	Common Materials & Preparation . . . . .	32
2.1.1	Substrates . . . . .	32
2.1.2	Cleaning Procedure . . . . .	33
2.1.3	Device Structure & Sample Holder . . . . .	34
2.2	Equipment for Solution Processing . . . . .	35
2.2.1	Glovebox & Spin Coater . . . . .	36
2.2.2	Bell Jar Evaporator . . . . .	36
2.3	Equipment for Vacuum Processing . . . . .	37
2.3.1	Train Sublimation Purifier . . . . .	37
2.3.2	Thermal Evaporator . . . . .	38
2.4	Electrical & Material Characterization . . . . .	39
2.4.1	Solar Spectrum Current-Voltage Measurements . . . . .	39
2.4.2	External Quantum Efficiency . . . . .	42
2.4.3	Long Term Decay . . . . .	43
2.4.4	Time-of-Flight Photoconductivity . . . . .	43
2.4.5	Other Characterization . . . . .	46
<b>3</b>	<b>Solution Processed Organic Photovoltaic Devices</b>	<b>48</b>
3.1	Materials . . . . .	48
3.2	Fabrication Techniques . . . . .	51
3.3	P3HT/PCBM Solar Cells . . . . .	52
3.3.1	Solution Temperature . . . . .	53
3.3.2	Solution Concentration . . . . .	54
3.3.3	Spin Speed . . . . .	55
3.3.4	Annealing . . . . .	56
3.3.5	Lithium Fluoride Buffer Layer . . . . .	57
3.4	Blend Composition Study of PQT-12/PCBM Organic PV Devices . . . . .	60
3.4.1	Experimental Details . . . . .	60
3.4.2	Current-Voltage . . . . .	62
3.4.3	UV-visible Absorption & EQE . . . . .	63
3.4.4	Photoconductive TOF . . . . .	65
3.4.5	AFM Imaging . . . . .	66
3.4.6	Summary . . . . .	68
3.5	Decay Study of PQT-12 based solar cells . . . . .	68
3.5.1	Experimental Details . . . . .	70
3.5.2	Current-Voltage Decay . . . . .	71
3.5.3	Fluorescence Decay . . . . .	72

3.5.4	Summary . . . . .	75
<b>4</b>	<b>Vacuum Coated Organic Photovoltaic Devices</b>	<b>76</b>
4.1	Materials & Purification . . . . .	76
4.2	Fabrication Techniques . . . . .	77
4.3	Photovoltaic Properties of M-Pc:C <sub>60</sub> . . . . .	78
4.3.1	Experimental Details . . . . .	79
4.3.2	Absorption Spectra . . . . .	80
4.3.3	Current-Voltage . . . . .	81
4.3.4	Lateral Time-of-Flight . . . . .	84
4.3.5	SEM Imaging . . . . .	85
4.3.6	Summary . . . . .	87
4.4	Rubrene as an additive in M-Pc:C <sub>60</sub> Cells . . . . .	87
4.4.1	Experimental Details . . . . .	89
4.4.2	Current-Voltage . . . . .	91
4.4.3	Decay Study . . . . .	95
4.4.4	Summary . . . . .	96
4.5	Organic Parallel Tandem Cells . . . . .	97
4.6	Parallel Tandem Cells using M-Pc . . . . .	99
4.6.1	Experimental Details . . . . .	99
4.6.2	Current-Voltage . . . . .	102
4.6.3	EQE & UV-vis . . . . .	104
4.6.4	Summary . . . . .	105
4.7	Solvent Treatment & Heteromorphic Tandems . . . . .	106
4.7.1	Experimental Details . . . . .	107
4.7.2	Current-Voltage . . . . .	107
4.7.3	EQE & Absorption . . . . .	109
4.7.4	Summary . . . . .	111
4.8	Combined Polymer & Small Molecule Tandems . . . . .	111
4.8.1	Experimental Details . . . . .	112
4.8.2	Current-Voltage . . . . .	113
4.8.3	TiOPc/PQT-12:PCBM tandems . . . . .	114
4.8.4	Summary . . . . .	116
<b>5</b>	<b>Conclusions &amp; Future Work</b>	<b>117</b>
5.1	Thesis Summary . . . . .	117
5.2	Suggestions for Future Work . . . . .	119
	<b>Bibliography</b>	<b>121</b>

<b>A</b>	<b>Software Programs</b>	<b>139</b>
A.1	MATLAB code for solving equation (1.2) . . . . .	139
A.2	LabVIEW Virtual Instrument for EQE . . . . .	141
A.3	LabVIEW Virtual Instrument for Long Term Decay . . . . .	142
A.4	MATLAB code for formatting decay data . . . . .	143

# List of Figures

1.1	Typical I-V response for a solar cell . . . . .	4
1.2	Equivalent Circuit of a Solar Cell . . . . .	5
1.3	Formation of molecular orbitals in organic semiconductors . . . . .	9
1.4	Energy levels in organic and crystalline inorganic solids . . . . .	10
1.5	Flat band conditions for a simple organic solar cell . . . . .	14
1.6	Modified band diagram incorporating hole and electron blocking layers	16
1.7	Molecular structure of P3HT, MDMO-PPV, MEH-PPV and PCBM .	17
1.8	Solvent dependency of P3HT:PCBM films . . . . .	18
1.9	Inkjet patterned PQT-12/PCBM on flexible ITO-coated Mylar substrate	19
1.10	Molecular structure of M-Pc and C <sub>60</sub> . . . . .	22
1.11	Absorption profiles of P3HT and ClInPc, with the AM1.5 solar spectrum	24
1.12	Tandem cells fabricated by vacuum and solution processing . . . . .	26
1.13	Current challenges in OPV . . . . .	30
2.1	Etched ITO pattern for standard substrate . . . . .	33
2.2	Common device structure for organic photovoltaic devices . . . . .	35
2.3	Three-zone train sublimator for material purification . . . . .	38
2.4	Thermal evaporator used for vacuum processing . . . . .	39
2.5	Measured spectral output from Oriel 96000 solar simulator . . . . .	40
2.6	Block diagram for measuring of I-V response . . . . .	41
2.7	Vertical TOF sample and ideal transient for TOF . . . . .	44
2.8	Circuit diagram for TOF measurements . . . . .	44
2.9	Diagram and optical micrograph of LTOF Sample . . . . .	46
3.1	Molecular structure of PQT-12 and P3HT . . . . .	49
3.2	UV-vis spectra for hot solution, cold solution, and cast film of PQT-12	50
3.3	Varying solution temperature and the resultant J-V response . . . . .	53
3.4	Varying solution concentration and the resultant J-V response . . . . .	54
3.5	Varying spin speed and the resultant J-V response . . . . .	55
3.6	Varying annealing conditions and the resultant J-V response . . . . .	57
3.7	Effects of the insertion of a thin buffer layer of LiF on J-V response .	58

3.8	Effect of the insertion of a thin buffer layer of LiF on PV performance stability . . . . .	59
3.9	Device structure for I-V, EQE and TOF samples . . . . .	61
3.10	TEM cross section of a completed device . . . . .	61
3.11	J-V response and normalized I-V response for varying PQT-12 wt% . . . . .	62
3.12	Series resistance approximation as a function of the PQT-12 wt% loading . . . . .	63
3.13	UV-visible absorption of PQT-12/PCBM films and PQT-12 solutions and pristine films . . . . .	64
3.14	EQE of completed devices for different wt% of PQT-12 . . . . .	65
3.15	Sample transient for TOF measurements . . . . .	66
3.16	AFM image of the surface of a 15wt% PQT-12/PCBM film . . . . .	67
3.17	AFM image of the surface of a 50wt% PQT-12/PCBM film . . . . .	68
3.18	Absorption, fluorescence and molecular structure of PQT-12 . . . . .	70
3.19	Photovoltaic response of PQT-12 and P3HT based solar cells as a function of time . . . . .	72
3.20	Normalized fluorescence yield of bare PQT-12 and P3HT films in vacuum and ambient storage . . . . .	74
3.21	Fluorescence decay of P3HT & PQT-12 after UV exposure . . . . .	75
4.1	Bilayer and blend M-Pc/C <sub>60</sub> device structures . . . . .	80
4.2	Absorption spectra for M-Pc/C <sub>60</sub> Films . . . . .	81
4.3	V <sub>oc</sub> and PCE for M-Pc/C <sub>60</sub> bilayer and blended cells . . . . .	82
4.4	J-V response for bilayer and blended devices . . . . .	84
4.5	SEM image of a pristine ClInPc thin film . . . . .	86
4.6	SEM image of a 1:1 blended ClInPc:C <sub>60</sub> thin film . . . . .	86
4.7	Molecular structure and absorption coefficient of rubrene and ClInPc . . . . .	88
4.8	Device diagrams for M-Pc, C <sub>60</sub> and rubrene structures . . . . .	90
4.9	Energy level diagram for a layered ClInPc/rubrene/C <sub>60</sub> device . . . . .	93
4.10	EQE of varying rubrene, ClInPc and C <sub>60</sub> devices . . . . .	95
4.11	Absorption and photocurrent decay of rubrene . . . . .	96
4.12	Structure and energy level diagram for parallel tandem cells . . . . .	98
4.13	Structure diagram of a ZnPc/ClInPc:C <sub>60</sub> parallel tandem cell . . . . .	101
4.14	Energy level diagram for simple parallel tandem cell . . . . .	102
4.15	J-V response for simple tandem device . . . . .	103
4.16	EQE and absorption spectra for simple tandem device . . . . .	105
4.17	Device structures for solvent treatment study . . . . .	108
4.18	J-V response of different device structures incorporating ClInPc . . . . .	109
4.19	EQE and absorption spectra for heteromorphous tandem cell . . . . .	110
4.20	Device structure for PQT-12/M-Pc tandem cell . . . . .	113
4.21	JV response for M-Pc/PQT-12 tandem devices . . . . .	114
4.22	EQE & UV-vis for PQT-12/PCBM and TiOPc treated and untreated . . . . .	115

A.1	Screenshot of LabVIEW program used to measure EQE . . . . .	141
A.2	Screenshot of LabVIEW program used to measure long term decay I-V	142

# List of Tables

1.1	Differences between organic and inorganic crystalline semiconductors	8
3.1	J-V parameters for varying P3HT/PCBM solution temperature . . .	54
3.2	J-V parameters for varying P3HT/PCBM solution concentration . . .	55
3.3	J-V parameters for varying P3HT/PCBM solution spin speed . . . .	56
3.4	J-V parameters for varying P3HT/PCBM annealing conditions . . . .	57
3.5	J-V parameters for varying P3HT/PCBM cells with LiF/Al cathodes, before and after annealing . . . . .	59
3.6	J-V parameters for different compositions of PQT-12/PCBM . . . . .	63
4.1	J-V parameters for M-Pc/C <sub>60</sub> cells with and without rubrene . . . . .	92
4.2	J-V parameters for M-Pc parallel tandem study . . . . .	104
4.3	J-V parameters for Heteromorphic Tandem . . . . .	109
4.4	J-V parameters for PQT-12/PCBM solar cells with M-Pc underlayers	114

# List of Abbreviations

AM1.5G	Air Mass 1.5 Global, the solar reference spectrum
BCP	Bathocuproine (2,9-Dimethyl-4,7-diphenyl-1,10-phenanthroline)
BHJ	Bulk Heterojunction, a donor-acceptor blend of 2 or more materials
CB	chlorobenzene, a solvent used for the dissolution of PQT-12, P3HT and PCBM
ClInPc	Chloroindium Phthalocyanine
CuPc	Copper Phthalocyanine
DCB	1,2-dichlorobenzene, a solvent used for the dissolution of PQT-12, P3HT and PCBM
EHP	Electron-Hole Pair
EQE	External Quantum Efficiency, the number of electrons output to the external circuit per incident photon
H <sub>2</sub> Pc	Metal free Phthalocyanine
FF	Fill Factor, a measure of the squareness of a J-V curve, i.e. the maximum power divided by ( $I_{sc} \times V_{oc}$ )
HOMO	Highest Occupied Molecular Orbital in an organic semiconductor, analogous to the valence band of an inorganic semiconductor
$I_{sc}$	Short Circuit Current, the current generated when the terminals of the device are short circuited
ITO	Indium Tin Oxide, a transparent electrical conductor
$J_{sc}$	Short Circuit Current Density, i.e. short circuit current divided by area
LiF	Lithium Fluoride, a buffer layer that acts as a hole blocker
LTOF	Lateral Time-of-Flight Photoconductivity
LUMO	Lowest Unoccupied Molecular Orbital in an organic semiconductor, analogous to the conduction band of an inorganic semiconductor

M-Pc	Metallo-Phthalocyanine, a family of pigment molecules
MoO <sub>3</sub>	Molybdenum oxide, a buffer layer that can replace PEDOT:PSS
NIR	Near-Infrared
OLED	Organic Light Emitting Device
OPV	Organic Photovoltaics
OTFT	Organic Thin Film Transistor
PCBM	[6,6]-Phenyl C <sub>61</sub> butyric acid methyl ester, a soluble fullerene derivative
PCE	Power conversion efficiency
PEDOT:PSS	Poly(3,4-ethylenedioxythiophene)-poly(styrenesulfonate), a water-soluble hole conductor used as a buffer layer in OPV
P3HT	poly(3-hexylthiophene), a conjugated semiconducting polymer
PQT-12	poly(3,3''-didodecylquaterthiophene), a conjugated semiconducting polymer similar to P3HT
PV	Photovoltaics
R <sub>s</sub>	Series Resistance
R <sub>sh</sub>	Shunt Resistance
THF	Tetrahydrofuran, a solvent used to induce a polymorphic shift
TiOPc	Titanyl Phthalocyanine
TOF	Time-of-Flight Photoconductivity
V <sub>oc</sub>	Open Circuit Voltage, the voltage generated by the device under no load
VOPc	Vanadyl Phthalocyanine
ZnPc	Zinc Phthalocyanine

# Preface

This thesis includes 5 chapters, which are outlined as follows:

Chapter 1 establishes the research motivation, describes current work by other groups in the world, and presents a discussion on the theoretical basis of organic photovoltaics (OPV). Further, it provides the overall objectives of the thesis, and describes how the work in subsequent chapters relate to the overall design of OPV.

Chapter 2 describes the equipment and characterization techniques that were required to fabricate and characterize OPV devices at the Xerox Research Centre of Canada, where I conducted all of my lab work. Much of this equipment had to be procured and set up, since there was no active OPV research lab at the beginning of this project.

Chapter 3 describes the work I did on solution processed photovoltaic devices. It consists of some of the data from a study involving spin coating of P3HT:PCBM solar cells, followed by two scientific papers: A. “Blend composition study of poly(3,3'' - didodecylquaterthiophene) / [6,6]-phenyl-C<sub>61</sub>-butyric acid methyl ester solution processed organic solar cells” (Journal of Applied Physics, v. 105, p. 016105 (2009)) and B. “Improved stability of solution processed photovoltaic devices using PQT-12” (Solar Energy Materials & Solar Cells, v.94, p. 2455 (2010)). In both papers, I was the first author and lead researcher. The co-authors assisted me by providing guidance and editing the manuscript prior to submission.

Chapter 4 describes the work I did on vacuum coated photovoltaic devices. It consists primarily of 5 documents (both papers and patents): C. “Photovoltaic Properties of M-Phthalocyanine/Fullerene Organic Solar Cells” (submitted to Journal of Applied Physics), D. “Rubrene as an additive in M-Phthalocyanine/Fullerene Organic Solar Cells” (submitted to Solar Energy Materials & Solar Cells), E. “A simple parallel tandem organic solar cell based on M-Phthalocyanines” (patent pending by Xerox Corp., ‘Photovoltaic Device’, U.S. Ser. No. 12/910,056, filed Oct. 22, 2010),

F. “Heteromorphic Chloroindium Phthalocyanine Films for Improved Photovoltaic Performance” (patent pending by Xerox Corp., ‘Photovoltaic Device’, U.S. Ser. No. 12/910,005, filed Oct. 22, 2010), and G. “Improved Spectral Coverage with the Integration of M-Phthalocyanines into PQT-12/ PCBM Photovoltaic Cells” (patent pending by Xerox Corp., ‘Photovoltaic Device’, U.S. Ser. No. 12/910,028, filed Oct. 22, 2010). In document C,D, and E, I was the first author and lead researcher. The co-authors assisted me by providing guidance, helping to explain trends in data, and editing of the manuscript for logical flow prior to submission. In F and G, I was the second author (behind N. Bamsey), but was actively involved in the design and execution of experiment and data acquisition and analysis. The text that appears in the sections describing F and G are not taken from the letters written by N. Bamsey, but rather is my description and analysis.

Chapter 5 gives a summary of the research work presented in chapters 3 and 4, and further presents the overall implications for the thesis as a whole. Future work is also suggested.

Below is a summary of the documents that are described in detail in various sections of this thesis.

- A “Blend composition study of poly(3,3'' - didodecylquaterthiophene) / [6,6]-phenyl C<sub>61</sub> butyric acid methyl ester solution processed organic solar cells”, Journal of Applied Physics v. 105, p. 016105 (2009), A.P. Yuen, A.M. Hor, R.A. Klenkler, J.S. Preston, E.R.Q. Macabebe, E.E. van Dyk, R.O. Loutfy.
- B “Improved stability of solution processed photovoltaic devices using PQT-12”, accepted in Solar Energy Materials & Solar Cells (2010), A.P. Yuen, A.M. Hor, S.M. Jovanovic, J.S. Preston, R.A. Klenkler, N.M. Bamsey, R.O. Loutfy.
- C “Photovoltaic Properties of M-Phthalocyanine/Fullerene Organic Solar Cells”, submitted to Journal of Applied Physics, A.P. Yuen, A.M. Hor, S.M. Jovanovic, R.A. Klenkler, J.S. Preston, G.A. Devenyi, R.O. Loutfy.
- D “Rubrene as an additive in M-Phthalocyanine/Fullerene Organic Solar Cells”, submitted to Solar Energy Materials & Solar Cells, A.P. Yuen, N.M. Bamsey, A.M. Hor, J.S. Preston, R.A. Klenkler, S.M. Jovanovic, R.O. Loutfy.
- E “A simple parallel tandem organic solar cell based on M-Phthalocyanines”, patent filed by Xerox Corp. on Oct. 22, 2010 (‘Photovoltaic Device’, N.M. Bamsey, R.A. Klenkler, A.P. Yuen, U.S. Ser. No. 12/910,056)
- F “Heteromorphic Chloroindium Phthalocyanine Films for Improved Photovoltaic Performance”, patent filed by Xerox Corp. on Oct. 22, 2010 (‘Photovoltaic Device’, N.M. Bamsey, R.A. Klenkler, A.P. Yuen, U.S. Ser. No. 12/910,005)
- G “Improved Spectral Coverage with the Integration of M-Phthalocyanines into PQT-12/ PCBM Photovoltaic Cells”, patent filed by Xerox Corp. on Oct. 22, 2010 (‘Photovoltaic Device’, N.M. Bamsey, R.A. Klenkler, A.P. Yuen, U.S. Ser. No. 12/910,028)

# Chapter 1

## Introduction & Theory

### 1.1 History & Motivation

Due in part to an increased demand for environmentally friendly energy sources, organic photovoltaics (OPV, see list of abbreviations) have been the subject of much interest recently. Unlike its silicon based counterparts, OPV has the advantage of being not only cheaper to produce, but can also be fabricated on flexible substrates and in ambient conditions. Further, OPV has several other commercially advantageous characteristics, such as low weight, semitransparency, and abundance of source materials. However, organic materials do possess the inherent disadvantage of having much lower carrier mobility, strong film morphology dependence, and most notably, lower overall power conversion efficiency (PCE). To date, the most efficient organic solar cells are in the range of 5-8% [1–7], clearly demonstrating the present limitations in this technology towards further application. There has been significant work directed towards a basic understanding of charge transport and light absorption in a variety of organic materials [8–13]. For some of the more established and well studied materials (ex. polythiophene, polyphenylenevinylene, phthalocyanine and fullerene derivatives), much effort has also gone into studying device physics [13–16].

Early work in OPV in the 1970's involved using chlorophyll in single layer devices [17], as well as other pigments mixed with compound inorganic semiconductors, with efficiencies in the order of 0.001% - 0.1% [18–20]. Conductive polymers were also

discovered in the 1970's [21], and led to a whole new class of materials to integrate into OPV devices. The common characteristic of organic semiconducting polymers is that they are all *conjugated*, i.e. they have alternating single-double bonds along the backbone of the polymer chain. Tang made a notable contribution in 1986 with the fabrication of a 1% efficient device based on a bilayer structure consisting of copper phthalocyanine (electron donor) and a perylene derivative (electron acceptor) [22]. One promising category of OPV that has gained much attention is the so-called bulk heterojunction cell, first developed in 1995 concurrently by Yu [23] and Halls [24]. This form of OPV has the ability to be made through solution processing, which has the potential to be low cost due to high volume reel-to-reel processing.

In order to be realistically implemented on a large scale, efficiencies need to be increased to  $\sim 13\%$ , while keeping the cost low enough such that the cost per watt of the devices is competitive with its silicon counterparts. The target cost per watt in order to be competitive with conventional energy sources is in the order of 0.50 USD/W, however at prices higher than this, OPV can still find niche applications in portable power and in areas where grid connected electricity is not a viable option. However, for large scale implementation (ex. solar farms), if the efficiency is not high enough then the balance-of-system costs outweigh the potential benefits of the low cost per watt. Though the theoretical maximum efficiency of OPV has been quoted as high as 30% [25] based on a Shockley-Queisser limit [26] with polaron losses, the realized efficiencies are much lower. However, some groups have outlined techniques that could realistically lead to a PCE of over 10% within a few years [15].

Several applications of OPV have been envisioned. One possible application of OPV is their use in subsidizing energy costs for office buildings, since their semi-transparency can be used as a partial shade to lower air conditioning requirements while also producing power to further offset energy costs. While semi-transparency is obviously not a good feature for a maximum efficiency solar cell, the purpose of this application is not for maximum power production, but rather as an architectural component of an overall energy saving strategy. If this thin film technology could be mass produced on standard office building windows, the impact that an entire building face covered in solar cells could have on energy costs would be quite significant.

Indeed, for Building Integrated PV (BIPV), calculations have shown an energy savings of between 33-50% [27].

At the moment, startup OPV companies are targeting applications that take advantage of the inherent flexibility, such as OPV-integrated backpacks and tents for charging mobile phones, laptops, and music players [28]. Another application that various researchers have studied has been photovoltaic textiles, with the idea being that clothes could be worn with built-in PV power sources. There have already been reports of the integration of photovoltaics into garments [29].

## 1.2 Photovoltaic Theory

In order to understand the device physics for an organic solar cell, it is first important to discuss how the traditional inorganic crystalline silicon solar cell functions. In a pure, undoped single crystal silicon wafer, there exists a bandgap that is a result of a difference in the energy levels in the bonding and anti-bonding states of the valence electrons. Consequently, the lower energy states are mostly filled, and upper energy states are mostly empty with the exception of a few occupied states as a result of thermal excitation according to Fermi-Dirac statistics [30].

When a crystalline semiconductor is doped with p or n type dopants, the Fermi level is shifted from the middle of the bandgap towards the valence band or conduction band, respectively. If these two doped regions are brought in intimate contact with each other, excess mobile electrons and holes recombine, leaving behind uncompensated charges in the form of immobile nuclei. Consequently, a built-in electric field with a direction pointing from the n-side to the p-side forms within the depletion region of the junction.

If a photon of energy  $h\nu \geq E_g$  is incident on the crystal, a free electron-hole pair (EHP) is generated with the hole in the valence band and the electron in the conduction band. If this EHP is generated within a diffusion length (10-100  $\mu\text{m}$  for Si) of the depletion region, the electron and hole can be separated by the built-in field and collected at opposite electrodes. This is important because the photovoltaic effect requires an asymmetry for charge separation and collection.

### 1.2.1 Current-Voltage Response

In the absence of an external load, as optical excitation and charge separation builds up, the electric field that separates the EHP will be reduced until an equilibrium exists such that the rate of charge separation equals the rate of charge recombination across the junction. At this point, the potential difference between the two electrodes is referred to as the open-circuit voltage,  $V_{oc}$ .

If the two electrodes are externally short circuited, then the current that flows through the device is a result of the optically generated electron-hole pairs. This current is referred to as the short-circuit current,  $I_{sc}$ .

Of course, there exists a maximum power point somewhere between the conditions of  $I_{sc}$  and  $V_{oc}$ . The maximum power point on the I-V curve is the point at which the product of current and voltage is maximized. This gives rise to a third important parameter in solar cell research, the fill factor. It is defined as:

$$FF = \frac{P_{max}}{V_{oc} \cdot I_{sc}} \quad (1.1)$$

The FF is essentially a measure of the “squareness” of the I-V curve of the cell. Figure 1.1 shows a typical I-V response of a solar cell, with the important points along the curve noted.

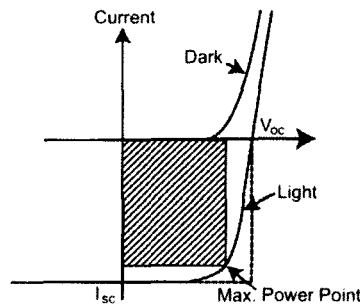


Figure 1.1: Typical I-V response for a solar cell

From (1.1), it becomes immediately evident that in order to increase the maximum power output of a cell, one must increase  $FF$ ,  $I_{sc}$ , or  $V_{oc}$ .  $I_{sc}$  is the most varying of

the parameters, as it is directly tied to light absorption, charge separation and charge collection.  $V_{oc}$  is mostly a function of the bandgap of the material being used. Lastly, Fill Factor is dependent on parasitic resistances in the form of a shunt resistance,  $R_{sh}$ , and a series resistance,  $R_s$ . These are modeled in the equivalent circuit of a solar cell, as shown in Figure 1.2, where the model describes a light-dependent DC current source in parallel with an ideal diode.

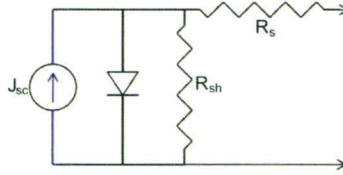


Figure 1.2: Equivalent Circuit of a Solar Cell

The I-V characteristic equation can be modified to incorporate these parasitic resistances, and for a fourth quadrant curve (as in Figure 1.1), is expressed as [31]:

$$J = -J_{sc} + J_s \left( e^{\frac{nq}{kT}(V - JAR_s)} - 1 \right) + \frac{V - JAR_s}{AR_{sh}} \quad (1.2)$$

where  $J_{sc}$  is the short circuit current density,  $J_s$  is the dark current density,  $\frac{kT}{q}$  is the thermal voltage,  $n$  is the diode ideality factor,  $R_s$  is the series resistance,  $R_{sh}$  is the shunt resistance, and  $A$  is the active area. Since this is a non-trivial function, even if all parameters are known, the J-V response has to be numerically calculated (see appendix A.1). A brief examination of (1.2) demonstrates that in order to deliver more power to the load for a given current, the shunt resistance should approach  $\infty$  and the series resistance should approach 0. Further, it can be shown that the inverse slope of the J-V curve at the  $V_{oc}$  can be used to estimate the  $R_s$ . Similarly, the inverse slope of the J-V curve at the  $J_{sc}$  can be used to estimate  $R_{sh}$  [31]. These are useful approximations when comparing different J-V curves, but to calculate the actual resistance values, a numerical iterative approach is required.

### 1.2.2 External Quantum Efficiency

A very useful measurement for the characterization of solar cells is the external quantum efficiency (EQE). It is a measure of the fraction of electrons made available to the external circuit, divided by the incident photons at any given photon energy. The EQE at any photon energy  $E$  can be found by measuring the short circuit photocurrent density at that incident photon energy, which is described as:

$$EQE(E) = \frac{J_{sc}(E)}{qI(E)} \quad (1.3)$$

where  $J_{sc}(E)$  is the measured short circuit current density in  $A/m^2$ ,  $I(E)$  is the monochromatic photon flux in  $photons \cdot m^{-2} s^{-1}$ , and  $q$  is the elemental charge. From the EQE, the total expected short circuit current can be found with:

$$J_{sc} = q \int_0^{\infty} EQE(E) b_s(E) dE \quad (1.4)$$

where  $J_{sc}$  is the total short circuit current density in  $A/m^2$ , and  $b_s(E)$  describes the solar spectral photon flux, or the number of photons in the range of energy  $E$  to  $E + dE$ , in  $photons \cdot m^{-2} s^{-1} eV^{-1}$  [31]. This integral of the product of EQE and solar irradiance is often compared against the actual measured  $J_{sc}$  as a verification, and is in good agreement with theory. The EQE is a very important figure of merit, though it is often misinterpreted as a power conversion efficiency (PCE). In the context of OPV, despite monochromatic EQE being achieved at greater than 70% [32, 33], PCE is still around 5%. The main discrepancy between the PCE and EQE comes from the fact that reported EQE is for a narrow band of wavelengths, with the EQE sometimes dropping precipitously to near zero at wavelengths beyond 650 nm for many polymer based OPV due to poor photon absorption. However, for wavelengths within the absorption spectrum, the high EQE is an indication that light absorption, charge separation and charge transport can be efficiently achieved in an organic film. The EQE values are also deceptive because they are a measure of the photon to electron

conversion efficiency, and do not take into account the photovoltage of the collected electrons.

### 1.3 Design Considerations for PV devices

For any PV device, whether organic or inorganic, there are 4 factors to consider to design an efficient solar cell:

- (1) Photovoltage of separated charges
- (2) Absorption efficiency of light
- (3) Separation efficiency of excited states into free holes and electrons
- (4) Collection efficiency of separated charges at opposite electrodes

This generalized approach is applicable to both organic and inorganic cells. The first factor is mainly determined by the bandgap of the material being used. For single material inorganic solar cells, which are the majority of PV cells fabricated today, factor (1) and (2) are intrinsically linked and pull in opposite directions. That is, for a higher photovoltage, the material absorbs correspondingly less solar light due to the higher bandgap. This is not the case for organic solar cells, and will be discussed in Section 1.5.2. Factor (3) is a device design issue, and has to do with the average distance that an exciton needs to travel before it can be separated into a hole and electron. If this distance is longer than the diffusion length, then on average the exciton will recombine and the optical excitation is wasted. Factor (4) is determined by the ability of the material to conduct both holes and electrons efficiently while limiting leakage in the diode. These four factors manifest themselves in the electrical parameters of the J-V curve. Specifically,  $V_{oc}$  is related directly to factor (1),  $I_{sc}$  is related to both factor (2) and (3), and FF is related to factor (4). Therefore, using these measurable parameters, one can gain insight into how design choices affect each of these four factors.

## 1.4 Organic vs. Inorganic Semiconductors

There are several key differences between the conduction physics involved in organic vs. inorganic semiconductors, and these must be discussed before examining OPV device structures. A summary of these differences is listed in Table 1.1, and is followed by a discussion on the effects of those differences.

	Organic	Inorganic Crystalline
Bonding	Weak	Strong
Long Range Order	None to Very Little	Yes
Carrier Localization	Localized ( $\sim 10$ nm)	Delocalized ( $\sim 10$ $\mu\text{m}$ )
Carrier Mobility	$10^{-5}$ - $10^0$ $\text{cm}^2\text{V}^{-1}\text{s}^{-1}$	$10^2$ - $10^3$ $\text{cm}^2\text{V}^{-1}\text{s}^{-1}$
Temp. Dependence	Temp. $\uparrow$ , Conductivity $\uparrow$	Temp. $\uparrow$ , Conductivity $\downarrow$

Table 1.1: Differences between organic and inorganic crystalline semiconductors

### 1.4.1 Weak vs. Strong Bonding

In an inorganic semiconductor, atoms are bound to their nearest neighbour by strong covalent bonds with short ( $\sim \text{\AA}$ ) distances between them that are smaller than the de Broglie wavelength of electrons. Due to barrier lowering from interacting potentials, an excited electron is mostly delocalized across large distances (10-100  $\mu\text{m}$ ) relative to the lattice constant. As a result, the wavefunctions of many excited electrons overlap and interact, and band theory is used to describe the occupation of available states. Band theory can be used to accurately predict transport properties, and the high level of delocalization gives rise to a high mobility in the order of  $10^3$   $\text{cm}^2\text{V}^{-1}\text{s}^{-1}$  for materials such as single crystal silicon. Further, in doped semiconductors, carrier mobility at room temperature decreases with increasing temperature as a result of phonon scattering. In solar cells, this is particularly important since the efficiency of a Si cell can drop by a significant fraction on a hot day vs. a cold day.

For organic semiconductors, the valence band and conduction band models do not strictly apply due to the weaker  $\pi$  bonding as opposed to  $\sigma$  bonding. Atoms are indeed bound to their nearest neighbour within a polymer chain or small molecule,

giving rise to an energy gap, but the energy bands (see Figure 1.3) are local to the molecule [34]. In the case of polymers, the  $\pi$  bonding in conjugated polymers (i.e. polymers with alternating double and single bonds along the backbone) allows for conduction along the backbone, and disruption of the conjugation results in the loss of its semiconducting nature [35]. The energy gap exists between what are called the  $\pi$  and  $\pi^*$  band, which arise from the highest occupied molecular orbital (HOMO) and lowest unoccupied molecular orbital (LUMO), respectively. The so-called  $\pi - \pi^*$  transition is similarly a way of expressing an electron in a  $\pi$  bond (HOMO) transitioning to an antibonding (LUMO) orbital. This is analogous to the band gap between the valence and conduction bands in inorganic crystals, as this separation in molecular orbitals mostly dictates the optical absorption edge.

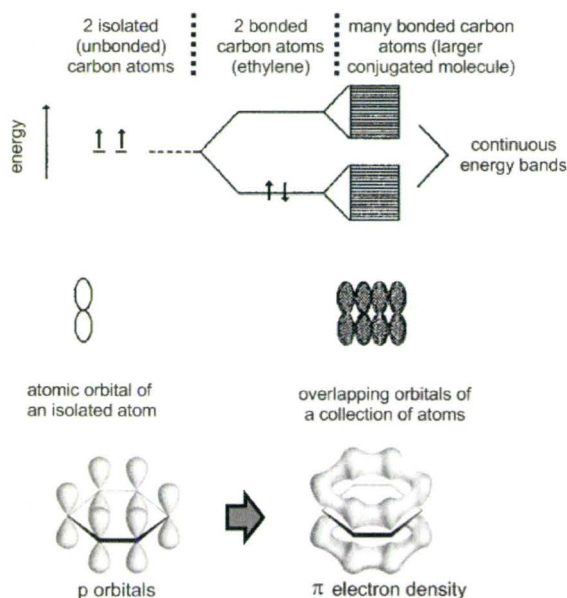


Figure 1.3: Formation of molecular orbitals in organic semiconductors. Image modified from [36]

While the treatment of bonding and anti-bonding orbitals can be applied to inorganic crystals by treating the crystal as an infinitely large “molecule”, the fundamental difference with organic semiconductors is that these molecular orbitals are spatially separated from the molecular orbitals of the nearest molecular neighbour

due to weak Van der Waals forces [34]. As a result of the large spatial separation, the molecular potential wells only weakly interact, resulting in highly localized carriers (see Figure 1.4) due to a lack of barrier lowering. This is somewhat similar to an individual isolated molecule in a vacuum, and therefore the energy levels in individual molecules closely resemble the energy levels in the bulk [34]. Indeed, organic semiconducting solids can be thought of as a collection of mostly independent point source conductors. This is the basis for many organic transport theories, including the very commonly used Bässler formalism [8].

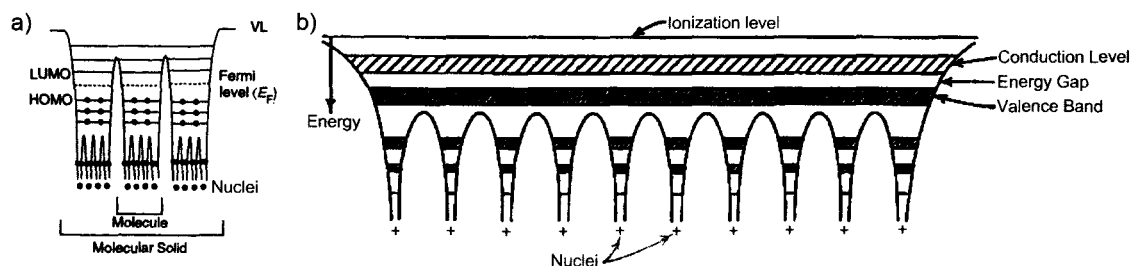


Figure 1.4: Energy levels in a) organic solid and b) crystalline inorganic solid. Images modified from [34] and [37].

The high degree of localization has several consequences. First, the carrier mobility becomes very low ( $10^{-5}$ - $10^0$   $\text{cm}^2\text{V}^{-1}\text{s}^{-1}$ ) compared to crystalline inorganics. Second, charge carriers now must propagate by moving from molecule to molecule through phonon assisted charge hopping. The result of this is that at higher temperatures, the increase in phonons actually increases conductivity in organic semiconductors [37]. Indeed, organic PV devices actually have a positive temperature coefficient [38]. Finally, since carriers are highly localized and few in number, there is relatively little interaction between electron wavefunctions. This implies that Fermi level equilibration at interfaces between separate organic materials occurs over very small distances, resulting in very sharp, almost abrupt, band bending [34]. As a result, the local electric field at the interface can be very high but does not extend over a large distance.

Another very important consequence of localized carriers is the effect of the film morphology on the overall conductive properties of the film. Studies have

shown a variation in hole mobility over many orders of magnitude depending on the crystallinity of the polymer [39]. Further, because these molecules can be highly anisotropic, especially for polymers, mobilities in certain directions can be many orders of magnitude higher or lower than in an orthogonal direction. Therefore, it is very important to note that the structure and order of the film is critical in determining the electrical properties of the film.

### 1.4.2 Long Range Order

In an inorganic crystal such as single crystal silicon, the long range order of the atoms is many times larger than the de Broglie wavelength of an electron and thus a nearly free electron model with a periodic lattice is a reasonably accurate model for the behaviour of an electron in an inorganic crystal solid. Solving for Schrödinger's equation, this periodicity of the lattice gives rise to a series of bands that describe the available energy states. In a semiconductor, there is a set of forbidden energies for a propagating electron in the lattice that are within the band gap. In the case of silicon, the top of the valence band and the bottom of the conduction band are energetically separated by 1.1 eV. However, they exist at different points in k-space. This implies that in order for a photon to excite an electron from the valence band to the conduction band, there must also be a phonon present in order to conserve crystal momentum. This is termed an indirect band gap, and results in relatively low optical absorption ( $\alpha \approx 10^3 - 10^4 \text{ cm}^{-1}$ ).

In an organic solid, molecules (whether small molecule or polymer) are weakly bound by Van der Waals forces and have no long range order since they are generally amorphous [34]. Since there is no long range order, conservation of crystal momentum does not apply, meaning that amorphous organic semiconductors behave like direct band gap materials and therefore have strong optical absorption ( $\alpha \approx 10^5 - 10^6 \text{ cm}^{-1}$ ). This is a direct consequence of Noether's theorem, which states that for every conservation law in nature, there exists an associated symmetry [40]. In this case, conservation of linear momentum is associated with translational symmetry, which exists in crystalline Si since the lattice is approximated as extending infinitely, but

does not exist in organic solids due to the mostly random nature of the polymer or molecules.

## 1.5 Organic PV Devices and Fabrication

### 1.5.1 Difference between Organic and Inorganic PV

In terms of charge transport, the main difference between organic and crystalline inorganic solar cells is that OPV is often achieved using heterojunctions as opposed to doped homojunctions. This arises from the fact that very few organic materials are capable of ambipolar transport, and doped homojunctions in the traditional sense require delocalized bands. As a result, materials that preferentially conduct holes (donors) or electrons (acceptors) act as p and n-type material, and there is often no reference to an “intrinsic” semiconductor since there is no doping.

In terms of optical absorption and charge separation, there is a large difference between organics and inorganics. In crystalline Si, optical excitation results in the creation of a Wannier exciton, where the exciton radius is larger than the atomic separation. The binding energy of this type of exciton is in the order of 10 meV, which is smaller than the thermal energy at room temperature (25 meV). As a result, optical excitation in Si can be approximated as the generation of an immediately free electron in the conduction band and hole in the valence band [41]. For organic solids, the optical  $\pi - \pi^*$  transition in a polymer or pigment results in the formation of a Frenkel exciton, whose radius is often smaller than the molecular separation [42]. This binding energy varies, but is generally much larger than 25 meV and so the exciton is tightly bound. This exciton, however, can dissociate at the interface of two materials with different HOMO/LUMO levels. In other words, an electron in an excited state will preferentially reside in the material with the energy level further from vacuum. Since fullerene ( $C_{60}$ ) is a good electron conductor and has a LUMO level further from vacuum than the LUMO level for most conducting polymers/pigments of interest, fullerene and its derivatives are the predominant acceptor in OPV. When an electron donating polymer is brought into intimate contact with  $C_{60}$ , the result is a positive

polaron species on the polymer that is stable and delocalized intramolecularly [43]. A similar argument can be used with the holes if the exciton is generated on the acceptor. As a result of this charge transfer at the interface between the polymer and  $C_{60}$ , the charge transport can be separated by phase and carrier types can be preferentially conducted by different materials. Consequently, the charge transfer can be seen as a redox reaction occurring at the donor-acceptor interface. Indeed, this ultrafast ( $\sim 100$ ps) photoinduced electron transfer from a conjugated polymer to a fullerene was demonstrated [44–46] and served as a catalyst for the beginning of solution-processed organic photovoltaics.

### 1.5.2 Method of Operation & OPV Design

There are several design considerations for OPV devices that depend on the four factors described earlier. Light is absorbed by the polymer/pigment, depending on its energy gap. The introduction of an electron accepting fullerene provides the interface necessary for charge separation, and provides the required asymmetry in the form of phase separated conduction. The next most important concept is the collection of electrons and holes at the electrodes to do work. In order for these separated charges to remain apart there must be an electric field to overcome coulombic attraction. The field also causes charges to hop towards opposite electrodes, depending on the polarity of charge. Unlike in inorganic junctions, the built-in electric field is a result of two electrodes with different work functions sandwiching the active layer. Indium Tin Oxide (ITO) is a suitable high work function anode ( $\sim 4.7$ - $5.1$  eV), and has the added benefit of being highly transparent. This is important, since the traditional metallic finger/busbar configuration would not be suitable for OPV due to the extremely low lateral conductivity, resulting from the very small diffusion length ( $\sim 10$  nm) due to localized carriers. As a result of using a semitransparent electrode, carriers have orders of magnitude smaller distance to travel before encountering an electrode. Often, aluminum or silver is used as the cathode due to their lower work functions ( $\sim 4.3$  eV) and high electrical conductivity. Calcium is another low work function material (2.7 eV), but is not ideal due to its high reactivity with atmospheric moisture.

Although this difference in work function is thought to be the driving force behind the collection of charges at opposite electrodes, it does not dictate directly the open circuit voltage. Brabec et al demonstrated in 2001 that the open circuit voltage is more strongly correlated to the difference in the HOMO of the donor and the LUMO of the acceptor, and had very little dependence on the cathode material over a wide range of work functions [47]. Figure 1.5 represents a simplified band diagram for a donor/acceptor blend.

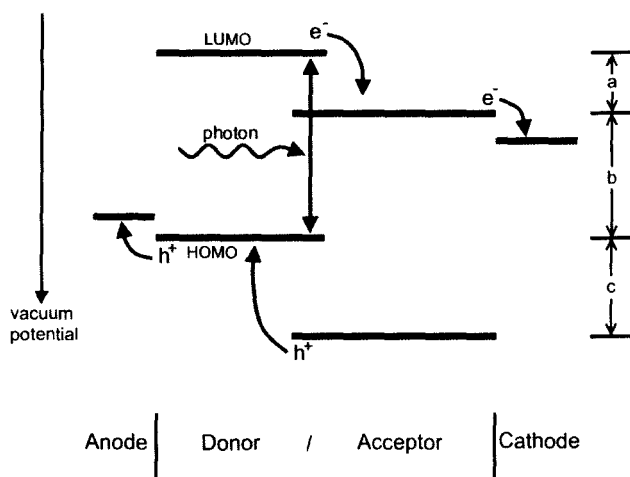


Figure 1.5: Flat band conditions for a simple organic solar cell

The method of operation can be summarized as follows:

- Step 1 Generation of an exciton by absorption of a photon
- Step 2 Diffusion of exciton to a donor-acceptor interface
- Step 3 Separation of exciton into a  $h^+$  in the donor and  $e^-$  in the acceptor
- Step 4 Phase separated conduction of holes and electrons
- Step 5 Collection of electrons in cathode and holes in anode

Another particular advantage does arise, however, from heterojunctions. Since there are now two separate materials, different optical absorption profiles can be mixed to yield a larger spectral coverage. Further, the relative positioning of the donor and acceptor energy levels with respect to vacuum can be significant. In Figure 1.5, although optical absorption is mostly determined by the bandgaps of the two

materials ( $E_g(\text{donor}) = a + b$ ,  $E_g(\text{acceptor}) = b + c$ ), the  $V_{oc}$  is determined mostly by the size of spacing  $b$ . For an organic heterostructure, two materials can be chosen with  $b$  maximized while  $a$  &  $c$  are tuned such that  $E_g(\text{donor})$  and  $E_g(\text{acceptor})$  absorb complementary portions of the solar spectrum, i.e.  $a \neq c$ . In essence, the optical absorption and photovoltage can be partially de-coupled, which is not possible in homojunctions since  $E_g(\text{donor}) = E_g(\text{acceptor})$  in a homojunction. Given the near-infinite number of combinations of organic molecules and their corresponding energy levels, there are theoretically a near-infinite number of possible materials for OPV. That being said, fullerenes are one of the very few electron acceptors in use, and they have the unfortunate property of having an absorption profile that is mostly in the blue/UV region. As a result, most OPV cells use pigments and polymers that absorb in the green/red/NIR region to act as the primary photon absorber. It may also be possible to introduce a third component [48], a sensitizer, with an  $E_g(\text{sensitizer}) \approx b$ , a HOMO level matched to the HOMO(donor) and a LUMO level matched to the LUMO (acceptor). This would result in a narrow energy gap material (redshifting the absorption edge), while maintaining the voltage.

When considering the limitations on charge collection, on first glance it would seem that organic materials are not suitable for solar cell applications. However, due to their high optical absorption, very thin ( $\sim 100\text{nm}$ ) layers are required to absorb a large portion of the light, which partially makes up for the short carrier diffusion length. When examining Si, the opposite is true, since the low optical absorption necessitates large diffusion lengths in order to operate as a solar cell. From this, one can conclude that the optical absorption and conductivity cannot be examined independently to determine the feasibility for solar cell applications. Rather, it is the ratio of the optical absorption depth to the carrier diffusion length that is important, since this determines the fraction of total incident photons that can be converted to external electrons, regardless of thickness. For this reason, OPV cells are inherently a thin-film technology.

A further consideration is avoiding the undesirable recombination of electrons in the anode and holes in the cathode. In order to mitigate this, an electron blocking layer is inserted between the anode (ITO) and the active layer, and a hole blocking

layer is inserted between the cathode (Al, Ag, Ca) and active layer. This is somewhat analogous to a back surface field in traditional Si cells. To act as a hole or electron blocking layer, the material can either be a highly preferential conductor (hole and electron mobilities many orders of magnitude apart) or can have HOMO/LUMO energies that make it energetically unfavorable for either holes or electrons to transfer to it. A modified band diagram, with hole and electron blockers, can be seen in Figure 1.6.

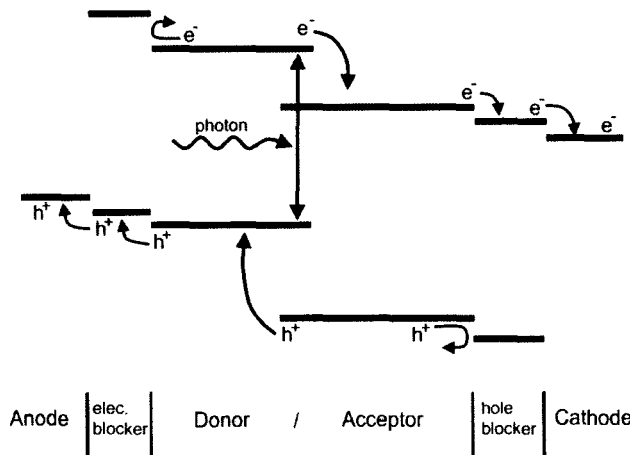


Figure 1.6: Modified band diagram incorporating hole and electron blocking layers

### 1.5.3 Solution Processed Materials & Fabrication

Solution processed OPV are predominantly of one structure: the bulk heterojunction (BHJ). The BHJ uses a blended donor-acceptor matrix to allow for a thick layer (high optical absorption), yet a much higher interfacial area (efficient exciton separation) compared to the traditional bilayer structure. If there are near bi-continuous pathways, reasonable charge transport efficiency can also be attained. Another advantage of polymer based cells is that they can be solution coated at ambient conditions, drastically improving its potential for scale up.

To date, the most popular polymer hole conductors for OPV have been polythiophene (PT) and polyphenylenevinylene (PPV) derivatives. These polymers have

demonstrated field-effect hole mobilities in the order of  $10^{-1} \text{ cm}^2\text{V}^{-1}\text{s}^{-1}$  in a pure film [49, 50]. Within these groups of materials, the derivatives that are most commonly used for donors are poly(3-hexylthiophene) (P3HT), poly[2-methoxy-5-(3,7-dimethyloctyloxy)-p-phenylene vinylene] (MDMO-PPV), and poly[2-methoxy, 5-(2'-ethylhexyloxy)-1,4-phenylenevinylene] (MEH-PPV). Fullerene derivatives, which have functional groups attached to them that allow them to be dissolved in solvents, are used as acceptors. The most common derivative is [6,6] Phenyl-C<sub>61</sub>-butyric acid methyl ester (PCBM). Molecular structures are shown in Figure 1.7. In particular, P3HT is likely the most commonly studied material, and generally yields high efficiencies in many research labs. A particularly fortuitous property of P3HT is that it has a tendency to self-organize into molecular crystals that aid hole conduction. This was demonstrated in 2004, when Li et al allowed the P3HT:PCBM film to self-organize during a 20 minute drying period. The effect was a drastically increased power conversion efficiency by improving the charge carrier mobility balance [1].

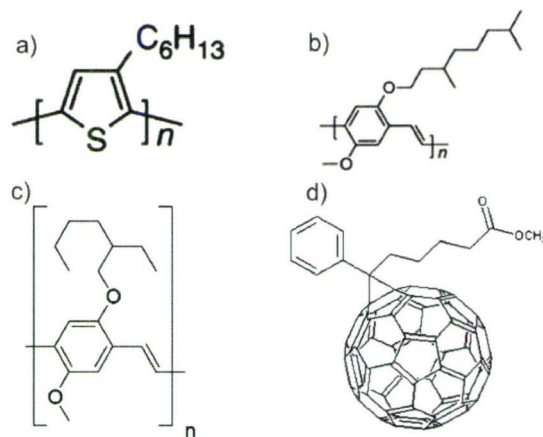


Figure 1.7: Molecular structures of a) P3HT, b) MDMO-PPV, c) MEH-PPV and d) PCBM

Fabrication of polymer devices is much more flexible than for small molecule devices, since solution processing allows for more options, including: spin coating, spray coating, and blade coating. These generally eliminate the need for large capital investment facilities, such as those required to produce traditional silicon devices

(clean rooms, photolithography, ion implanters, diffusion ovens, etc). However, the difficulty arises from the fact that there are many variables involved in the production of these composite films in ambient conditions. For instance, Kim et al have shown that composite films of P3HT and PCBM using chlorobenzene as a solvent produce a higher power conversion efficiency than films using dichlorobenzene [51]. A much larger difference has also been shown for chlorobenzene and toluene [43], as shown in Figure 1.8. These discrepancies are the result of a difference in the film morphologies, which in turn has a direct effect on the mobilities of the charge carriers as well as an effect on the interfacial area [52].

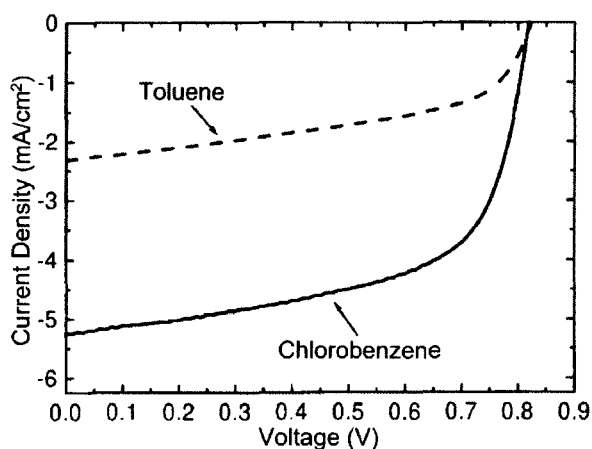


Figure 1.8: J-V curves of P3HT:PCBM films spun from chlorobenzene or toluene solvent. Image modified from [53].

One of the main methods for solution processing is spin coating, which has the ability to yield high quality, uniform thin films. It is particularly useful in developing prototypes for research and development, however it is difficult to make quality films over large areas due to the nature of the method. Spin coating requires that the donor-acceptor blend is dispersed or dissolved in a solvent with a relatively low boiling point. As the substrate spins, the blend will spread to cover the entire surface of the substrate and the solvent will evaporate, leaving behind the blend that comes out of solution. There are three main parameters that affect the results of the spin: viscosity of the blend, spin speed, and the solvent temperature. The viscosity, in turn, is a

function of the donor and acceptor concentration, as well as the temperature of the blend while spinning. Naturally, a larger concentration and lower temperature will lead to a larger viscosity and a thicker layer for all other conditions being equal. A slower spin speed will also result in a thicker film. The solvent, in addition to the previously mentioned effect on the film morphology, also needs to be examined for boiling point. This is due to the fact that the composite blend needs to come out of solution either during spinning or shortly thereafter, and the boiling point will affect the required duration of the spin. Further, the substrate temperature will have a similar effect as the solvent temperature, with a hot substrate yielding a thinner film. While spin coating is ideal for making quality films on a small scale, it is not suitable for large scale production. Economically, spin coating is a very wasteful process, as most of the material dropped on the substrate is lost during the spinning.



Figure 1.9: Inkjet patterned PQT-12/PCBM on flexible ITO-coated Mylar substrate

Although spin coating is the de-facto standard for producing lab scale OPV, spray coating, web coating, and dip coating are all actively explored for the purposes of scale-up. Spray coating a polymer solution is conceptually identical to spray painting, and in many cases the same equipment can be used to form the film. Unfortunately, the spray produces a very fine mist with a wide distribution of droplet size, and this droplet size partially determines the domain size of the donor-acceptor (D-A) blends when the solvent evaporates. It is therefore very difficult to control the morphology

of the coated layer, and consequently the repeatability of spray coat deposition is not as high as for spin coating. Web coating, on the other hand, is much more repeatable and is the method preferred for the OPV industry. It involves dragging a substrate within microns of a blade or drum, and as the substrate passes, the solvent evaporates, leaving behind a film. Unlike in spin coating, the remaining solution that is not deposited on the substrate is either pushed along, or falls into a drum for later use. This results in drastically less waste, and is a proven method in the coating of camera film and photoreceptors. Dip coating is a similarly low-waste process, whereby the substrate is literally dipped into a container of solution, then pulled at a rate that determines the thickness of the leftover film. Inkjet printing is also possible for patterning OPV [54,55], and was demonstrated using equipment available at the Xerox Research Centre of Canada (XRCC) (see Figure 1.9). Inkjet printing is not an efficient method of covering large areas, however it does have the advantage of being able to monolithically integrate series-connected cells into complete modules with minimal material waste. This would be particularly advantageous if the inkjetted active layer could be combined with solution processed electrodes.

#### 1.5.4 Vacuum Coated Materials & Fabrication

Small molecule based solar cells utilize photoconductive pigments to act as a donor and are often used in conjunction with fullerenes or inorganic nanoparticles to form OPV heterojunctions. There are two general classes of device structures for small molecule-based OPV: Layered Heterostructures and Co-Evaporated Heterostructures.

Layered heterostructures are conceptually very similar to traditional Si p-n junctions. The photon absorption occurs mostly in the donor (p-type), and excitons diffuse to the donor-acceptor (D-A) interface where they are dissociated into free electrons in the acceptor (n-type) and free holes in the donor. However, given the very short diffusion length, these layers are necessarily very thin ( $\sim 10$  nm) so that the majority of excitons can reach the interface. While these organics are highly absorbing, a large portion of the light still passes through the cell because 10 nm is simply not enough material for complete absorption.

Co-evaporated heterostructures are conceptually similar to bulk heterojunction cells, and involve donors and acceptors in one uniform blended layer. In this case, even if the overall active layer is much thicker than the exciton diffusion length, since the donors and acceptors are blended together on the scale of nm's, the average distance that an exciton must travel before encountering a D-A interface is still in the order of the exciton diffusion length. The advantage of this structure is that if charges can efficiently hop from donor to donor or acceptor to acceptor, charge collection can still be efficient and the active layer can be made thicker to increase optical absorption. There is a tradeoff between high absorption and efficient carrier collection, but if the film is structured such that there would be percolation pathways for both holes and electrons, the blended structure can still yield acceptable collection efficiencies.

When comparing layered and blended structures, one must examine factors (2)-(4) from Section 1.3 (absorption, separation, and collection). Layered heterostructures show low absorption, low separation, and good collection whereas co-evaporated heterostructures show high absorption, good separation, and moderate collection. Indeed, for many classes of materials, D-A co-evaporated blends outperform layered devices due to higher absorption and better separation. There are cases, however, where a bilayer structure outperforms the blend, and this is shown in the experimental section of this thesis.

There are many options for donor materials in small molecule OPV. The phthalocyanine group of materials [56, 57] were the first to show efficiencies above 1%, and are indeed still of interest to research groups. These have a common ring structure, but substitution of the central moiety with hydrogen ( $H_2$ ), metals (Cu, Mg, Zn), chlorinated metals (Cl-In, Cl-Al), or oxygenated metals (Ti=O, V=O) can change the energy levels, absorption profiles, and transport properties. The acceptor molecule, as expected, is often fullerene. Figure 1.10 shows the molecular structure of both M-Phthalocyanine and  $C_{60}$ .

In order to fabricate these devices, the thin films are evaporated or sublimed at high vacuum since small molecules are often not soluble and are difficult to disperse in a solvent without the use of an inert polymer binder. This tends to limit the

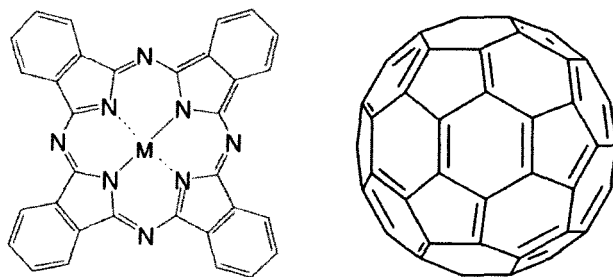


Figure 1.10: Molecular structure of (L) M-Phthalocyanine and (R) C<sub>60</sub>

throughput of said devices, since vacuum coating is a batch process. The morphology of the thin film layers is also highly dependent on substrate temperature and deposition rate, with fast deposition generally yielding disordered films [58]. This poses a further problem to the scale up of these devices, and takes away from the economic advantage that is the main reason to pursue OPV in the first place. However, the substrate temperature ( $< 200\text{ }^{\circ}\text{C}$ ) does not need to be nearly as high as in crystalline inorganic devices, and so can be processed on flexible plastics.

### 1.5.5 Pre and Post Production Considerations

Since the surface conditions of the ITO electrodes can vary with humidity and contamination, it is important to pretreat the ITO in order to achieve optimal spin coating conditions. Based on surface energy studies of ITO for the fabrication of OLED's, it has been determined that cleaning the ITO with an oxygen or argon plasma can greatly increase adhesion and consequently increase lifetime and electroluminescent efficiency [59, 60]. For many solution processed polymer OPV, an electron blocking buffer layer of poly(ethylenedioxythiophene):poly(styrenesulfonate) (PEDOT:PSS) is added, and has shown to greatly increase the OPV performance [61]. This polymer has the advantage of being soluble in water, yet not soluble in most organic solvents that the active layers are dissolved in. This is important, because sequential solution coating requires that already-deposited layers are not soluble in the solvent for the subsequent process. However, since the ITO-(PEDOT:PSS) inter-

face is not stable [62], various transition metal (Mo, V) oxides have been attempted as buffer layers, with similar performance benefits as PEDOT:PSS and a more stable interface [63]. Similarly, a thin ( $\sim 1\text{nm}$ ) thermally evaporated LiF hole blocking layer can be inserted between the active layer and the aluminum, increasing the fill factor from 0.5 to 0.6. This is a result of a reduction of the series resistance and work function of aluminum [64] due to the formation of a dipole moment when the  $\text{Li}^+$  selectively adheres to the organic and the  $\text{F}^-$  adheres to the metal. This is a result discovered from OLED studies, where the barrier is lowered for electron injection from the cathode [65].

Annealing can also have a large effect on the performance of the OPV, since it allows for the possibility of further ordering of the polymer and hence increased mobility. Interestingly, there has been no consensus on the optimal annealing conditions, even for a single material. For example, even in P3HT:PCBM blends, reported optimal annealing temperatures have ranged from  $75^\circ\text{C}$  to  $140^\circ\text{C}$  [32, 51]. Padinger et al have also suggested the application of an external field larger than the  $V_{oc}$ , which they believe burns out short circuits (thus increasing shunt resistance) as well as enhances crystallization of the polymer [32], which would aid in hole transport. Li et al have also suggested annealing the device after the electrode has been deposited, as they postulate that the Al acts as a cap to prevent vertical movement of the polymer chains and results in better lateral alignment [66].

## 1.6 Current Challenges & Research

Before large scale commercialization of OPV can be attained, there are several notable challenges that must be overcome. Naturally, the largest and often most cited drawback to OPV is the low efficiency, with cutting edge technology still yielding only 5-8% [1–5] efficient cells, compared to production volume Si solar cells at 24.2% [67] and laboratory grade Si solar cells recently measured at 25% [68, 69]. However, efficiency is only one of the challenges, and a few of the active areas of research will be discussed here.

### 1.6.1 Spectral Mismatch & Low Band Gap Materials

Despite OPV having high monochromatic EQE near 500nm, the power conversion efficiency is limited severely by the spectral mismatch, particularly in the NIR region. Fortunately, there is flexibility in the synthesis of the different organic semiconductors, with slight variations in side chains yielding different absorption spectra. Several groups have developed low-band gap conjugated polymers to capture the near IR portion of the solar spectrum [4, 6, 7, 70–75] and this seems to be the preferred direction of research given the difficulty of sequential solution processing for tandem structures. In addition, Wienk et al demonstrated an increased absorption from C<sub>70</sub>-based PCBM (PC<sub>70</sub>BM), which they attribute to the asymmetry of C<sub>70</sub> compared to C<sub>60</sub> [76]. Another possible venue for extending absorption is to use narrow band gap phthalocyanine molecules as a sensitizer for polymer/fullerene systems in either a donor-sensitizer-acceptor configuration or in dispersion in the polymer/fullerene blended film. Figure 1.11 shows the complementary absorption profiles of P3HT and a trivalent metal phthalocyanine (ClInPc). Other groups have been successful with ZnPc and MDMO-PPV [77]. Section 4.8 describes the efforts by our group to integrate a solution processed polythiophene with a vacuum coated phthalocyanine.

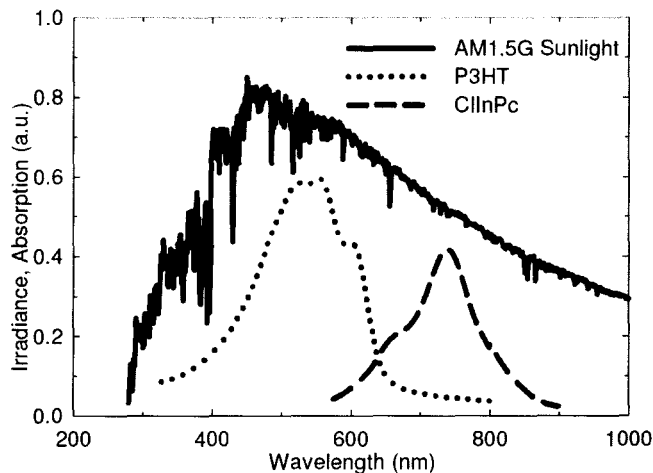


Figure 1.11: Absorption profiles of P3HT and ClInPc, with the AM1.5 solar spectrum

## 1.6.2 Hybrid Structures

In addition to polymer/fullerene OPV, some groups have investigated hybrid organic/inorganic systems by blending hole conducting polymers with inorganic nanocrystals [78, 79]. The advantage of nanocrystals is three-fold: 1) inorganic nanocrystals tend to have a higher electron mobility than fullerene, 2) inorganic semiconductors tend to have broader absorption profiles over the visible region, and 3) absorption profiles can be tuned over a fairly wide range depending on the size of the nanocrystal. Thus far, full spectrum power conversion efficiencies as high as 1.8% have been demonstrated in a PPV/CdSe nanorod system ( $\text{OC}_1\text{C}_{10}$ -PPV:CdSe), demonstrating broad absorption in the CdSe with absorption peaks tunable from 520-590 nm [80]. Hybrid organic-inorganic devices have also been fabricated with PbS quantum dots, showing tunable photocurrent spectra peaks from 1000-1400 nm [81].

## 1.6.3 Tandem Structures

Another possibility for increasing the efficiency of OPV is the vertical stacking of cells into a tandem structure to capture complementary portions of the solar spectrum, similar to what is done in III-V materials [2, 82]. In these III-V systems, low bandgap substrates (typically Ge) are used with deposited thin films of GaAs and  $\text{GaInP}_2$  to absorb complementary portions of the solar spectrum. The stacking of these materials also results in an addition of the photovoltage, since they are connected in series via tunnel diodes. However, the performance of these series tandem cells is very dependent on the thicknesses of the layers, since the currents generated in each layer have to be equal to each other in a series configuration [83]. When considering the solar spectrum, in addition to the absorption profiles and carrier mobility in each material, current matching by tuning deposition conditions and thicknesses becomes a non-trivial problem. These cells have yielded power conversion efficiencies of  $\sim 40\%$ , but the fabrication cost has restricted them to applications where area is at a premium (i.e. concentrators, satellites/rovers, solar vehicles). The high cost per watt of these cells is due not only to the rarity of Ge, Ga, and In, but also to the difficult fabrication of quality films and tunnel diodes via metal organic vapor phase

epitaxy. Simply, the fabrication of III-V tandem cells is too complicated to be cheap.

Organic series tandem cells are also possible, but the design considerations for III-V tandems do not directly apply to organic tandems. While organic materials do have the advantage of very high peak absorption coefficients, the absorption profiles are relatively narrow in comparison to materials used for inorganic photovoltaics (ex. Si, GaAs, CdTe). This is because the  $\pi$ - $\pi^*$  absorption is a discrete energy level transition attributable to an individual molecule, and the width of the absorption profile for the entire thin film is a reflection of the random interaction between molecules in the film. Therefore, it is not a strict band-to-band absorption, and the width of available states is considerably less than for an inorganic crystal. In order to extend absorption, some attempts at fabricating organic series tandems have been made [84, 85]. These have the same general structure as III-V tandems, with an interfacial recombination layer in between two active layers. Note that traditional III-V tandem structures always have the lowest band gap materials at the bottom, but this is not always a necessity in organic cells since the absorption spectra of organic materials are usually quite narrow, with little overlap. Current matching is still required for organic series tandems, but with the nearly complementary absorption profiles the tuning of thicknesses is not as complicated as for III-V tandems.

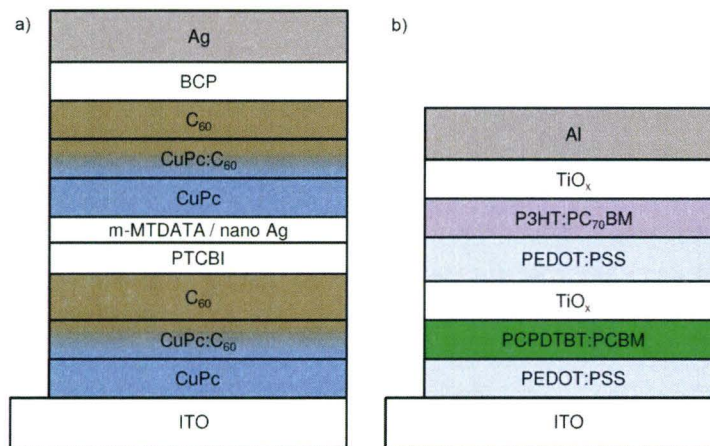


Figure 1.12: Tandem cells fabricated by (a) vacuum coating [2] and (b) solution processing [4]

Xue et al have demonstrated power conversion efficiencies of 5.7% using dual copper phthalocyanine:fullerene (CuPc:C<sub>60</sub>) layers, with the front cell being rich in CuPc (donor, red/yellow absorption) and the back cell being rich in C<sub>60</sub> (acceptor, blue absorption) [2]. The tandem structure has also been explored in solution processed devices as well, which is particularly impressive because sequential solution processing is often difficult due to complications arising from solvents dissolving the solid layers that were previously deposited. Kim et al overcame this by depositing TiO<sub>x</sub> using sol-gel techniques, resulting in an all solution cast cell yielding 6.5% efficiency [4]. Figure 1.12 demonstrates both the vacuum deposited and solution coated tandem cells.

#### 1.6.4 Degradation & Long Term Stability

Unlike bulk silicon, which cannot be easily oxidized or reduced at ambient temperatures, polymers can easily oxidize. Consequently, in the presence of a group VI element such as oxygen, the polymer will donate an electron to the oxygen, thus leaving behind a hole. This is a form of doping of the polymer, and while it may increase its conductivity it also distorts the backbone of the polymer. In the presence of an energy source such as light, the oxygen can bond with the polymer at a carbon site, thus changing the conjugation and potentially affecting its semiconducting nature. As a result, OPV cells tend to require encapsulation of the working device to prevent photo-oxidation. Even if a cell is completely hermetically sealed, degradation can still occur inside the device itself. Of particular note is aggregation of the donors or acceptors. If larger domains form, the interfacial donor-acceptor surface area also decreases, thus reducing the exciton separation efficiency. This problem is much more difficult to solve than atmospheric degradation, and is still an ongoing challenge for the research community. Some groups have attempted to improve this by developing block copolymers consisting of the donor and acceptor, and have shown that phase aggregation can be slowed by the addition of around 20% of block copolymer to the donor-acceptor blend [86].

### 1.6.5 Large Area Uniformity

One of the main problems that many OPV technologies face is the ability to produce highly uniform thin films across large areas. In technologies such as organic thin film transistors (OTFT) and organic light emitting devices (OLED), the 2D patterning of the thin films is such that the individual active areas can be quite small, often the size of a pixel for a display or a few  $\text{mm}^2$  for an RFID tag. As such, irregularities in the surface of the film play a far less dramatic role in the production yield of the devices as a whole, since it is much easier to get a pinhole-free small area than a perfect film over a large area. However, this luxury cannot be afforded for OPV, which is by its very nature a maximal area device. Ideally, in order to be commercially viable, these thin films would have to be able to function pinhole-free over areas of several  $\text{m}^2$ . However, one way of avoiding a short circuit could be to pattern many smaller devices on a surface and monolithically connecting the small devices together in series. This is in essence the same technique used in the production of practical solar modules, however it also adds in the complication of needing to connect the top of each small device to the bottom of the next at high speed and volume. This also reduces the total photovoltaic area, as the interconnects occupy module area, similar to the effect of grid-shading in traditional Si cells.

### 1.6.6 Economic Challenges & Balance of System

Although some of these rather complicated materials are currently expensive, it is assumed that economies of scale will result in a much lower price for refined carbon-based materials such as conjugated polymers and fullerenes. However, one often overlooked element of cost is the price of ITO. The problem arises from the fact that ITO is one of the very few choices for a suitable transparent electrode, and recent prices have been driven up as a result of increased demand for LCD and plasma displays. Also, with the dependence of this material on the availability of indium, a rare element, the reduction in price of ITO with production volume is somewhat minimal. Consequently, groups have attempted to use carbon nanotubes as a replacement for ITO. Preliminary results in OLED's [87] have shown promise,

but the technology is still in its infancy.

In addition, though OPV proponents will often tout the importance of a low cost per watt, there is a threshold requirement for efficiency, since too low of an efficiency will result in the balance of systems (support structure, land cost, etc) becoming the dominant cost factor for large scale solar power farms. However, for applications that put a premium on mechanical flexibility, organic PV is quite suitable even at lower efficiencies.

## 1.7 Thesis Objectives & Scope

There are currently many outstanding challenges in the field of OPV before they can begin to be a significant player in the photovoltaics market. These challenges, along with some of the explored techniques to overcome those challenges, are depicted in Figure 1.13. The issues that this thesis addresses are also highlighted, with device efficiency challenges receiving the majority of the attention. Device efficiencies are primarily a scientific research concern at this point in the life-cycle of OPV technology, and hence was the main area of focus in this academic thesis. Therefore, this thesis fits well within the framework of the current direction of OPV technology.

The main objective of this thesis is to explore the integration of materials into organic photovoltaic devices. As previously discussed, the performance of a solar cell is ultimately controlled by 4 factors: (1) the photovoltage of separated charges, (2) the ability to absorb light, (3) the exciton separation efficiency, and (4) the collection of charges. Understanding the effects that new materials or structures have on these 4 aspects is crucial to the improvement of the photovoltaic performance as a whole. These aspects are all examined in this thesis, and techniques for improvement are explored. Both solution processed and vacuum coated organic PV devices are investigated, since the 4 aspects above apply equally to both classes of devices. Although the chemical synthesis and engineering of new materials is crucial for the advancement of this technology, these aspects are beyond the scope of this thesis and are not covered.

To improve the photovoltage of devices, a new device structure integrating rubrene

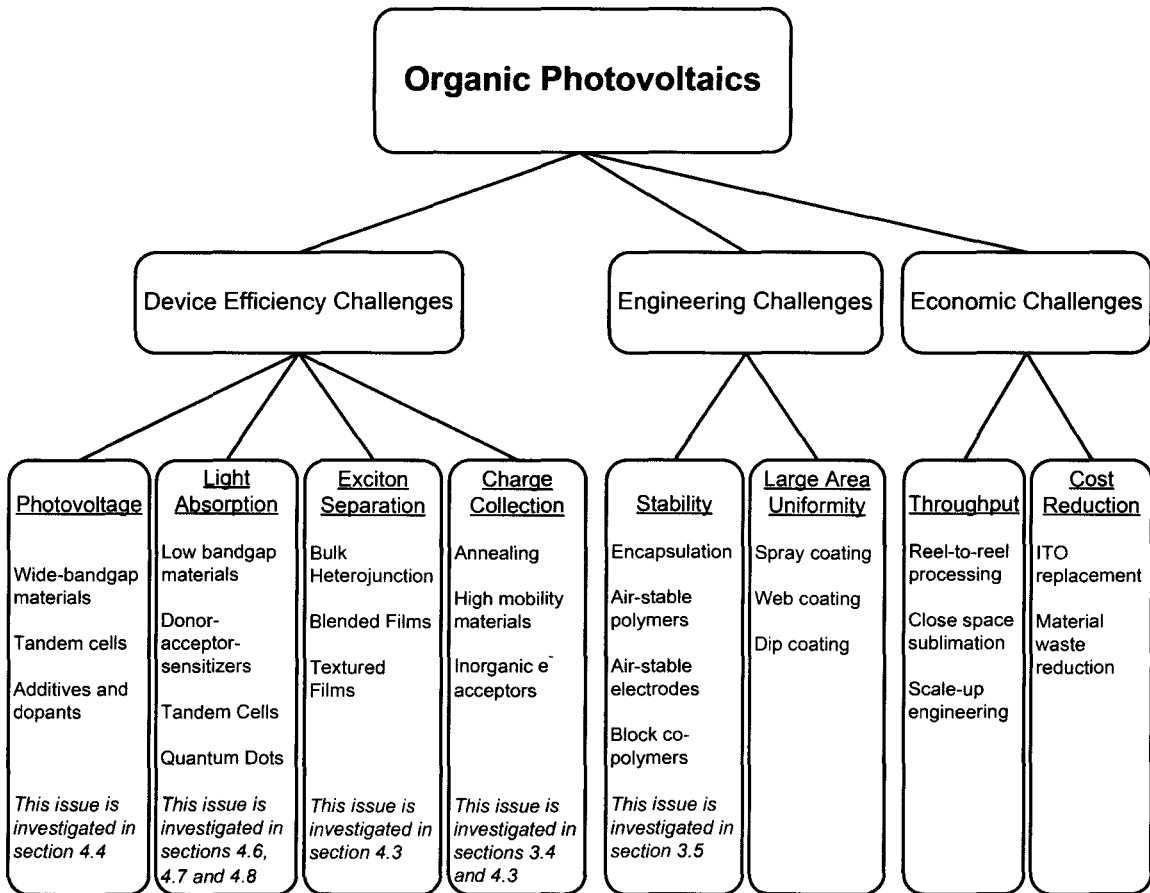


Figure 1.13: Current challenges and methods of addressing them in the field of Organic Photovoltaics

is explored and compared against findings in literature. To improve the absorption of solar cells, two new device structures (the parallel tandem device and the heteromorphic device) and a method of treating materials (solvent conversion) are explored. To improve the separation efficiency, the effects of blending M-Pc and C<sub>60</sub> are explored, and generalized trends regarding the valency of M-Pc are examined. To understand the role of device structure on the charge transport properties of materials, time-of-flight photoconductivity studies are conducted on both solution coated and vacuum coated materials. In order to implement this technique for vacuum coated thin films, the novel *Lateral* Time-of-Flight photoconductivity method is employed. Finally, the improvement of the stability of OPV devices is necessary for the commercialization

of the technology. The role of integrating a relatively new material, PQT-12, into solution processed OPV devices is also examined.

Research in these areas is necessary for the adoption of OPV devices in the market. Despite the seemingly large difference between solution coated and vacuum coated OPV devices, the two classes of devices are actually intrinsically linked by the 4 factors controlling OPV performance. Therefore, knowledge gained from examining one class of materials could be applied to improving the other. This would not only add to the scientific body of knowledge, but could help accelerate their use in industry to generate clean, cheap power for the world.

## Chapter 2

# Equipment & Characterization

The following chapter describes the equipment used in the fabrication and characterization of organic solar cells produced in our laboratory at both the Xerox Research Centre of Canada and the Centre for Emerging Device Technology (CEDT) at McMaster.

### 2.1 Common Materials & Preparation

There are three aspects that are in common for the fabrication of both solution processed and vacuum coated PV cells. These are the substrates used, the method of cleaning the substrates before deposition of organic layers, and the general device structure for testing in a common sample holder.

#### 2.1.1 Substrates

All devices are fabricated on 50 mm x 50 mm Indium Tin Oxide (ITO) coated aluminosilicate glass slides (Delta Technologies, Part # CB-40IN,  $15 \Omega/\square$ ). Each of these is etched in a pattern to produce 10 isolated ITO fingers that act as the anode for 10 different devices on the same substrate. There are two common ground pads also etched on opposite ends of the substrate. The ITO etching pattern can be found in Figure 2.1.

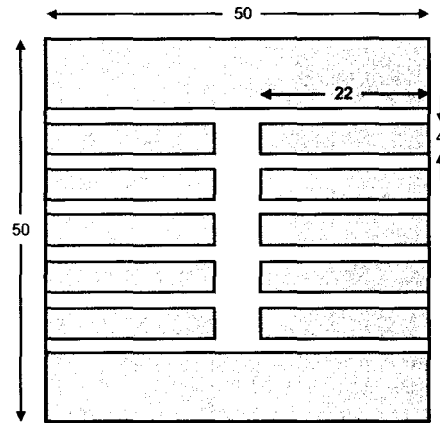


Figure 2.1: Etched ITO pattern for standard substrate (dimensions in mm)

To form the pattern, the ITO slide is spin coated with positive photoresist (AZ 1518) at a speed of 2500 rpm for 60 s. The slide is then soft baked at 90 °C for 30 minutes. After soft baking, the slide is exposed to UV ( $\sim 250 \text{ mJ/cm}^2$ ) using a long wave UV lamp (UVP Blak Ray Model B 100 AP) through a copper mask, then dipped in a beaker of MF-314 developer to remove the photoresist from the areas that were exposed to UV. Since photoresist will tend to build up on the edges of the substrate, this excess edge photoresist is then scratched off in the area between the fingers of photoresist. The substrate is then hard baked at 120 °C for 30 minutes. The slide is then etched using an acid mixture (10:10:1 of de-ionized water:HCl(38%):HNO<sub>3</sub>(70%)) heated to 60 °C, and left in the mixture for 1.5 minutes. The photoresist is then removed using acetone, leaving behind the desired ITO pattern. In this configuration, the 10 ITO fingers acted as anodes for up to 10 independent devices, while the two ground pads acted as a common cathode.

### 2.1.2 Cleaning Procedure

The cleaning of substrates before deposition of organic layers is critical to the performance of the device as well as the consistency of the results. A completed etched substrate is submerged in a detergent solution consisting of 1 part Extran 300

detergent with 50 parts de-ionized water for a period no shorter than 1 hour, with overnight being preferable. This surfactant is used to remove the organics on the surface. The slide is then scrubbed vigorously with a tissue and rinsed off for  $\sim 1$  min in flowing hot water. If the water wets the entire surface without selectively wetting the glass or the ITO fingers, then the slide was soaked in the detergent solution for a sufficient period of time. If it does not evenly wet the surface, the slide is re-submerged in the detergent solution for a longer period of time. The slide is then rinsed with de-ionized water, followed sequentially by methanol and isopropanol. Since solvents in squirt bottles tend to leave a residue based on the impurities in the solvent, the substrate is then suspended in a wire basket in a large beaker with a pool of boiling isopropanol underneath the basket. This method of using isopropanol vapour is highly effective in getting streak-free cleaned substrates, and failure to do this can lead to inconsistent results. The basket is then removed from the beaker and covered in aluminum foil to limit the dust falling on the substrate, and the basket is placed in an oven at  $140\text{ }^{\circ}\text{C}$  for 15 minutes to bake off any adhered solvent or water. The slide is then transferred to a UV-ozone cleaner and cleaned for 10 minutes. In some cases, the slide is also cleaned in an argon plasma cleaner (Harrick PDC-32G) for 5 minutes. Cleaned substrates are then carefully moved to a Petri dish using gloves to handle the edges or by handling only the backside of the substrate (the side without ITO).

### 2.1.3 Device Structure & Sample Holder

In order to test the OPV devices, a common device structure is used, consisting of an ITO anode, organic active layer(s), and a metal cathode. The completed structure is depicted in Figure 2.2. A sample holder was used to connect the contacts on the ITO substrate to the external circuit. Spring-loaded pins were mounted into a Teflon block, with four pins contacting the four corners (one on each corner) to act as the common ground. These pins were grounded to the shielding of a BNC connector, which was used to connect to the external circuit. The center pin of the BNC connector was soldered to a 10-pole rotary switch, which allowed for the selection of any of the 10 ITO fingers as the anode for the device being tested. Therefore, in the forward bias,

the current flow from anode (+) to cathode (-) is horizontally through the ITO finger, vertically through the active layer to the metal stripe, and horizontally again to the common ground pads. In this configuration, the only “active area” (i.e. area capable of photovoltaic power conversion) on the substrate are the ends of the ITO fingers towards the center of the substrate, where there is an active organic layer sandwiched between the ITO underneath and the metal stripe above.

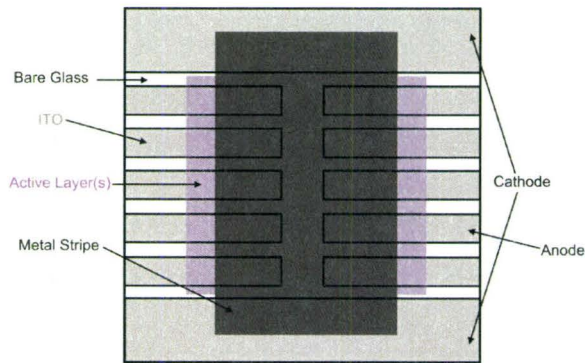


Figure 2.2: Common device structure for organic photovoltaic devices

The sample holder itself consisted of an aluminum project box with the spring loaded pins mounted inside. In order to control the testing environment, a gas feedthrough was used, allowing for a constant flow of any inert (nitrogen or argon) or reactive (oxygen) gas. The metal casing also helped to reduce any latent electrical noise, and was grounded to the shielding of the BNC connector.

## 2.2 Equipment for Solution Processing

To fabricate solution processed solar cells, several pieces of equipment needed to be set up and used. These are unique to solution processed solar cells and are therefore described separately from equipment used in vacuum processing.

### 2.2.1 Glovebox & Spin Coater

Since organic electronic thin films are susceptible to ambient humidity, without a controlled deposition atmosphere the performance of organic electronic devices depends on the season in which it is fabricated. This results in devices fabricated during the winter months (lower humidity) performing better than devices fabricated during the summer months. To counter this, a complete solution processing apparatus was set up inside of an environmentally controlled glovebox (Plas Labs Controlled Atmosphere Chamber). The oxygen and humidity content could be controlled using a constant purging nitrogen and vacuum, getting the oxygen level to below 1000 ppm as measured by an oxygen sensor (MSA Altair O<sub>2</sub> Pro). Humidity was lowered using a desiccant (Anhydrous calcium sulfate) to below 1% relative humidity. Unfortunately, due to available equipment, the oxygen and humidity levels could not be lowered any further.

The glovebox contained a spin coater (Specialty Coating Systems G3-8) connected to feedthroughs for vacuum and nitrogen purge, a weigh scale (Radwag AS100/C/2), and a hotplate (Heidolph MR 3003). This allowed for materials to be measured, dissolved in solvent, heated and filtered without being exposed to ambient air. This also ensured that as the active materials were coming out of solution during the spin coating process, they are not exposed to ambient levels of oxygen and humidity and remain in the relatively inert environment until they are transferred into a thermal evaporator for cathode deposition.

### 2.2.2 Bell Jar Evaporator

To deposit the metal cathode on the organic thin film, a thermal bell jar evaporator (Edwards Coating System E306A) is used. The chamber is connected to a diffusion pump that can bring the pressure down to  $3 \times 10^{-3}$  Pa. A tungsten wire basket is used to heat up a source of the metal (usually aluminum). Since this particular evaporator was not equipped with a quartz crystal monitor for thickness control, the thickness was calibrated by controlling the applied power, duration, and source-substrate distance and measuring the resulting thickness with an alpha-step profilometer.

## 2.3 Equipment for Vacuum Processing

To fabricate vacuum coated OPV, two pieces of equipment were required. The first, a train sublimation furnace, was used to purify materials. The second, a thermal evaporator system, was used to deposit organic and metallic layers.

### 2.3.1 Train Sublimation Purifier

To purify vacuum coated materials, a three-zone train sublimator (Figure 2.3) was used. This consisted of a glass source boat and a cleaned glass collection tube inside a glass carrier tube. The tube was pumped down to 20 Pa, followed by a trickling flow of nitrogen as a carrier gas. The carrier tube was inside of a three-zone furnace (Lindberg 59744A), which allowed for heating of the source material up to 600 °C, while the other two zones were controlled at 380 °C (collection zone) and 200 °C (impurity zone). There was also a liquid nitrogen trap to prevent impurities from getting into the vacuum pump. In this setup, the impure source material sublimates due to the high temperature, and is carried by the nitrogen gas flow towards the cooler zones. Since the impurities tend to have a lower sublimation temperature, they will continue towards the end of the tube until the temperature is low enough to condense on the walls of the glass. In some cases the impurities can travel all the way to the end of the glass tube, which is at room temperature. Meanwhile, the desired pure material will condense in the middle zone, which is set to a temperature that is below the sublimation point of that material. For the materials used in this project, 380 °C was sufficiently high to remove impurities while being sufficiently low to allow for condensation of the pure material. After approximately 24 hours of constant heating, the collection tube can be removed and the pure material is harvested from the walls of the tube.

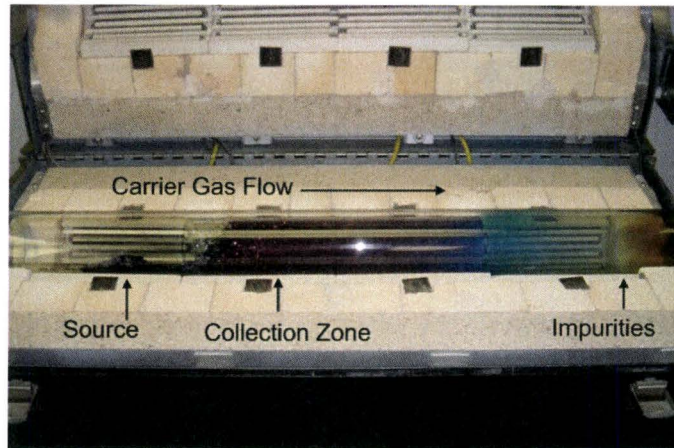


Figure 2.3: Three-zone train sublimator for material purification

### 2.3.2 Thermal Evaporator

A multi-mask, multi-source evaporator (PVT Systems/Intelvac) was used to fabricate all vacuum coated devices. This evaporator system was equipped with a mechanical pump and a cryo pump that could evacuate the chamber down to  $2 \times 10^{-4}$  Pa, and could hold up to 8 boats with the capability of co-evaporating from 2 different sources simultaneously. In addition, multiple masks could be used with a feedthrough in the evaporator without venting the chamber, allowing for all organic layers and the cathode to be deposited before exposure of the sample to air. This is important since the organic layers have a tendency to degrade when exposed to air, and the cathode acts as a partial encapsulation from the diffusion of ambient water and oxygen. In addition, the multiple masks allowed for the fabrication of up to 5 unique structures within a single pump down cycle. The thermal evaporator is depicted in Figure 2.4.

In order to monitor the thickness and deposition rate of the organic or metallic layers, 4 quartz crystal monitors were used. A deposition controller, which varies the power applied to the source boats, allowed for the control of the deposition rate. For discrete, sequential layers, only one crystal monitor is used at a time with one source. However, during a co-evaporation, 2 monitors can be used to measure the deposition rate of 2 sources, therefore allowing for composition control in the co-evaporation.



Figure 2.4: Thermal evaporator used for vacuum processing

## 2.4 Electrical & Material Characterization

The following section describes the equipment required to characterize completed devices, or the materials used.

### 2.4.1 Solar Spectrum Current-Voltage Measurements

To measure the power conversion efficiency of a device, the current-voltage (I-V) response of the device is measured when illuminated by simulated solar light. The sunlight is produced by an Oriel 96000 solar simulator with an accompanying AM1.5G spectral filter (Xe-arc lamp, see spectrum in Figure 2.5). The beam is collimated using the reflectors and lenses in the lamp housing, and the input power is monitored by exposing a calibrated Newport 818-UV/CM photodetector coupled to a Newport 1830-C power meter to the beam of light. The lamp power of the Oriel 96000 was tunable, allowing for the control of the incident light power. It should be noted that the Oriel 96000 is not a class ‘A’ simulator, and hence the spectral mismatch is quite pronounced. Since class A simulators cost several times more than the Oriel 96000, they were not feasible for this project. In addition, the Oriel 96000 is deemed sufficient for the relative measurements of OPV devices, since many world-class research labs

in published literature use the same simulator.

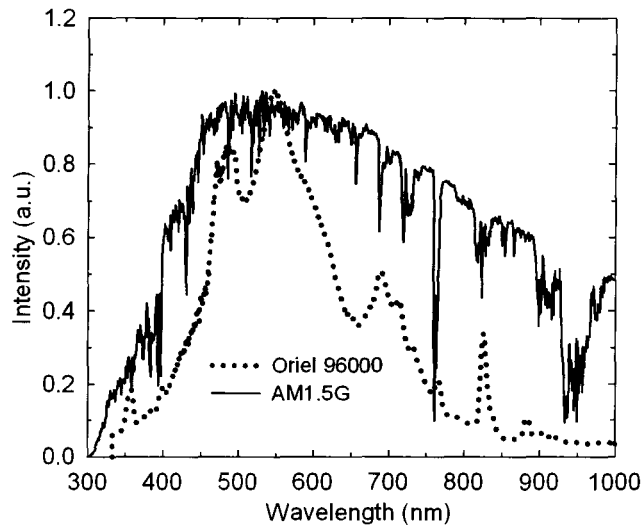


Figure 2.5: Measured spectral output from Oriel 96000 solar simulator

To measure the I-V response, a PC-connected source measure unit (Keithley 238) was used. The block diagram is depicted in Figure 2.6, where the applied voltage is positive. At a positive applied voltage greater than the  $V_{oc}$  of the OPV device, the current is positive in the direction shown. When the applied voltage is less than the  $V_{oc}$  of the OPV (or when  $V_{app} \leq 0$ ), the photogenerated current from the OPV causes a net current to be in the reverse direction, resulting in a negative measured current. The source measure unit was controlled by a PC with a LabVIEW program that was provided by Keithley.

In order to standardize and accurately define the area of the device for efficiency calculations, a shadow mask was used. This shadow mask was pressed up against the backside of the test sample and consisted of ten windows (3 mm diameter holes) drilled into a 200  $\mu\text{m}$  thick, 50 mm x 50 mm thick aluminum sheet. The windows were placed such that they were coincident on the active area of each ITO finger. Due to the thickness of the aluminum sheet, it could be assumed that the incident light in any section of the active area that is not exposed through a window was negligible. Accordingly, the active area for all devices, as defined by the shadow mask, was 0.07

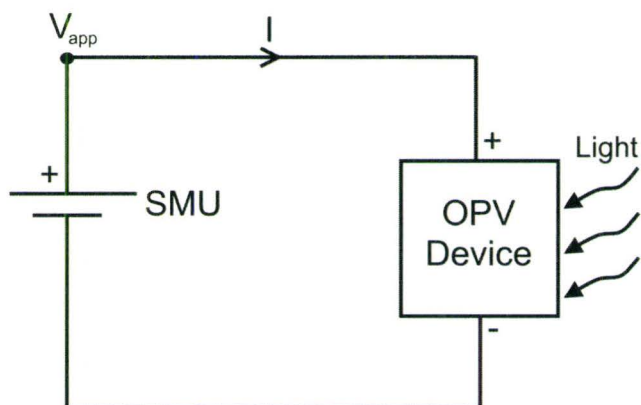


Figure 2.6: Block diagram for measuring of I-V response

$\text{cm}^2$ . A similar shadow mask with a single hole of the same diameter is used to cover the photodetector when measuring the incident power, such that the incident power as measured by the detector is the same as the incident power that falls on the completed OPV device.

The fabrication of OPV devices has a relatively high degree of variability, and is particularly sensitive to ambient conditions at the time of film deposition. To account for this variability, a different technique is employed for solution processed devices and vacuum deposited devices. For solution processed devices, the experiment is repeated several times to ensure that the establishing trend is still accurate. Devices are also made in parallel, sharing the same active layer solution and being spin coated on the same day in the same glovebox with controlled  $\text{O}_2$  and  $\text{H}_2\text{O}$  levels. For vacuum deposited devices, the experiments are always conducted by comparing against a control device, allowing for a comparison of relative performances. Due to the control afforded by the multi-mask evaporator, two comparison devices can also be made on the same substrate, giving them both the same substrate cleaning procedures, vacuum levels, and buffer/cathode deposition conditions.

### 2.4.2 External Quantum Efficiency

To measure the external quantum efficiency, a custom setup needed to be assembled. For wavelength control, a Xe-arc lamp was coupled to a programmable monochromator (Photon Technologies International) with a 500 nm blaze grating (1200 lines/mm). The output light was then coupled to an optical fibre and directed onto the sample holder, where the short circuit current of the device was measured with a Keithley 6485 Picoammeter. A LabVIEW program (see appendix A.2) was written to change the output wavelength, with the short circuit current measured at each wavelength. In order to compensate for 2nd order modes in the monochromator (ex. setting the monochromator to 800 nm and having 400 nm light output as well), optical filters were used. To measure quantum efficiency from 300 - 600 nm, an optical filter that cut off light above 600 nm was used (optical density  $> 4$  at wavelengths above 600 nm). A second scan, from 500 - 900 nm was also performed through an optical filter that cut off light below 500 nm. The reason for the overlap from 500-600 nm is that the attenuation profile of the optical filters is not perfectly square near their limits, causing discontinuities in the measurements. Using the current output from 300nm to 550nm, then from 550nm to 900nm, allows for correction of this discontinuity.

Since the output power of the monochromator is not uniform across all wavelengths, the incident power from the monochromator was measured using a Newport 818-UV/CM photodetector coupled to a Newport 1830-C power meter. The same LabVIEW program could then change the output wavelength, and at each wavelength the photodetector measured the power according to its calibrated responsivity at that wavelength. The same optical filters and ranges that were used for current measurement were used for optical power measurement. This gives a true representation of the incident power, and resulting current, at each wavelength. The number of electrons out and photons in could then be calculated using the current, optical power, and wavelength, yielding the external quantum efficiency according to equation (1.3).

### 2.4.3 Long Term Decay

To measure the photovoltaic performance as a function of time, a LabVIEW program (see appendix A.3) was written to measure the full I-V curve at user-defined intervals of time. In between measurements, the sample was fully irradiated with light, simulating operating conditions. The output files of the LabVIEW program were a list of times and a concatenated list of voltage-current measurements. The large data file was processed using a Matlab code (see appendix A.4) that could extract parameters such as  $J_{sc}$ ,  $V_{oc}$  and FF at each time. While testing long term decay, the sample chamber was filled with trickling nitrogen, argon, or oxygen flow (depending on desired test conditions) from a compressed gas cylinder.

### 2.4.4 Time-of-Flight Photoconductivity

To measure the mobility of charge carriers in a material, time-of-flight photoconductivity (TOF) [88] was used. This involves the time-resolved measurement of current through a sample after a short pulse of light in a spatially confined area. In this project, two methods are used: the conventional vertical TOF and the relatively new lateral TOF (LTOF).

In vertical TOF, a thick film (10's  $\mu\text{m}$ ) is deposited by drop casting a concentrated solution onto a conducting substrate, such as aluminized mylar. A second contact is either evaporated on top of the film, or a second piece of semi-transparent aluminized mylar is pressed against the film, which has shown to be as reliable as vapour-deposited contacts [89]. This sample structure is shown in Figure 2.7a. This contact must be semi-transparent to allow pulsed laser light through. An electric field of  $\pm 10^4$  V/cm is applied to the contacts, with the polarity determining the carrier being probed. The circuit diagram is shown in Figure 2.8. An  $\text{N}_2$  laser (Spectra Physics, 337 nm, 10 ns pulse) is then incident on the semi-transparent contact, exciting a thin sheet of charge carriers at the surface of the film. Since the absorption coefficient of the material is so high, over 90% of the light is generated in a region roughly 100 nm from the surface. Since the total thickness of the film is in the order of 10  $\mu\text{m}$ , this represents a well defined sheet of charge generated in roughly 1% of the

volume near the top electrode. The time-resolved current is then measured by using an oscilloscope to probe the voltage drop across a gain resistor. An ideal transient for TOF is shown in Figure 2.7b. The transit time was determined by the intersection of the asymptotes of the plateau and tail regions in a log-log representation. This TOF technique has been previously performed with other polymer-fullerene systems [90].

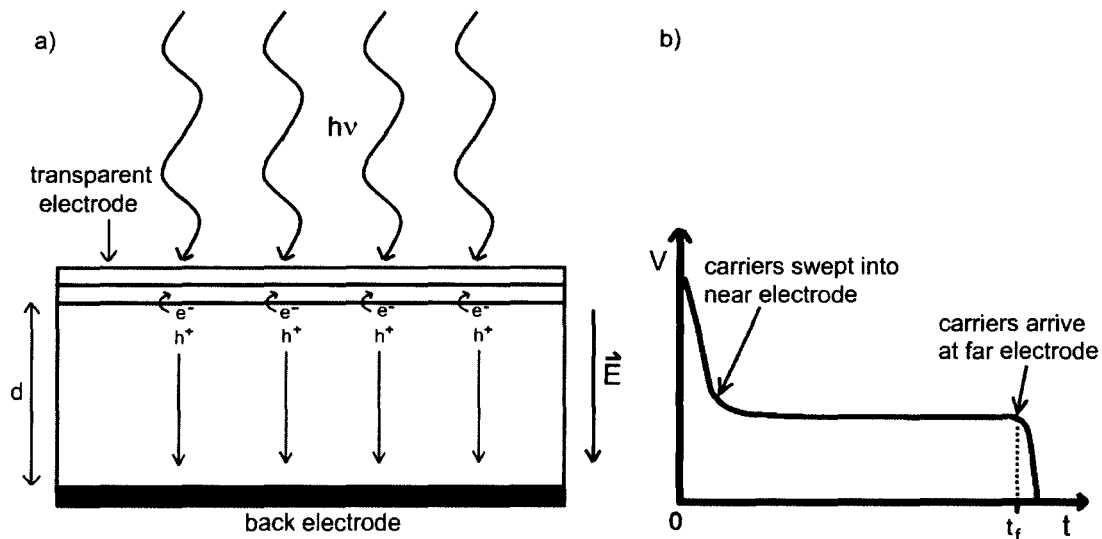


Figure 2.7: a) Vertical TOF sample and b) ideal transient for TOF

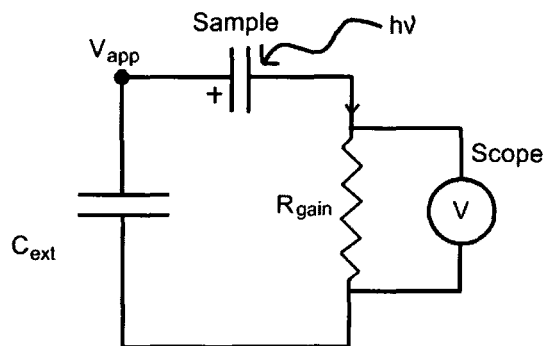


Figure 2.8: Circuit diagram for TOF measurements

The mobility of the charge carrier is defined as:

$$\mu = \frac{d^2}{t_f V_{app}} \quad (2.1)$$

where  $d$  is the effective flight distance,  $t_f$  is the time of flight, and  $V_{app}$  is the applied voltage. In vertical TOF, the effective flight distance is equal to the thickness of the sample.

In lateral time-of-flight (LTOF) [91, 92], sample thicknesses can be dramatically reduced by changing the orientation of the electric field. This allows for the measurement of carrier mobilities through thin (10's nm) vacuum coated layers. To do this, two thin aluminum or silver lines are evaporated 40  $\mu\text{m}$  apart through a shadow mask onto a glass substrate (see Figure 2.9). The organic semiconductor material of interest is then evaporated on top of the gap in between the metal line electrodes. Using a microscope, an N<sub>2</sub> dye laser (using a Coumarin dye centered at 650 nm, 10 ns pulse) is focused through the glass and directed towards one of the electrodes and a DC voltage is applied to achieve the desired electric field and polarity, where the magnitude was usually 10<sup>5</sup> V/cm and the polarity determines the type of charge carrier being probed. For example, if hole mobility is the desired measurement, the laser is focused on the electrode that is biased positively, causing electron-hole pairs to be generated near the positive electrode and holes to transit the 40  $\mu\text{m}$  gap width. Since the effective flight distance is defined by the lateral gap between the electrodes, the deposited thickness of the evaporated organic layer does not affect the transit time. However, the thickness of the organic layer needs to be sufficient to absorb a significant fraction of the light, therefore producing a strong enough signal for the oscilloscope. For many of the materials of interest, the absorption depth is in the order of  $\sim 100$  nm, so 50 nm is sufficiently thick to acquire a strong enough signal. This is a significant advantage of LTOF over conventional vertical TOF, since at a deposition rate of 0.1 nm/s, thicknesses of 10  $\mu\text{m}$  become prohibitively time consuming. The resulting current transient from an LTOF sample is measured using the identical gain resistor and oscilloscope setup described for conventional TOF, and the transit time and mobility is determined using the same method.

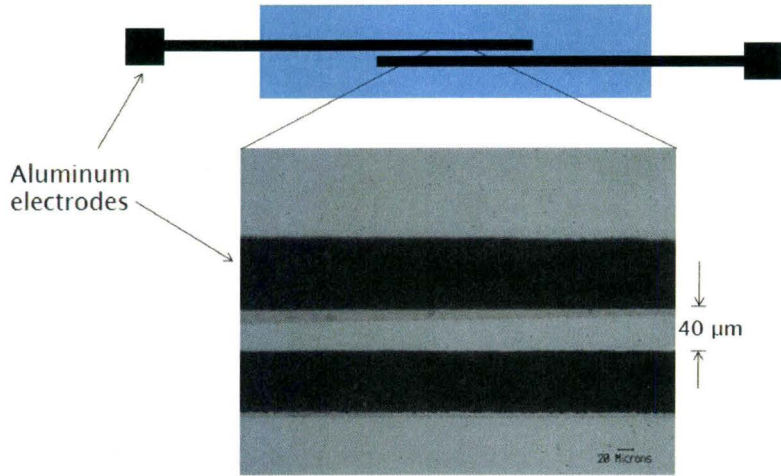


Figure 2.9: Diagram and optical micrograph of LTOF Sample

## 2.4.5 Other Characterization

In addition to electrical measurements of completed devices, characterization of materials was also important in the understanding of the device physics. The equipment described here was already set up at either the Xerox Research Centre of Canada or McMaster University.

To measure the UV-visible absorption of thin films, a Cary Varian 5000 spectrophotometer was used. Films were fabricated by either spin coating or vacuum coating the desired material onto glass or Mylar substrates and measured in the spectrophotometer using a blank glass or Mylar substrate as a baseline. The output of the spectrophotometer was the optical density at each wavelength scanned, which can be converted to an absorption coefficient if the thickness of the film is known. Equation (2.2) shows the relationship between  $\alpha$  and optical density.

$$\alpha = \frac{OD \ln 2}{t} \quad (2.2)$$

where  $\alpha$  is the absorption coefficient,  $t$  is the film thickness, and  $OD$  is the optical density.

To measure the thickness of a film, an alpha step (Dektak 6M Profilometer) is

used. At least two lines are scratched in the organic film to provide a reference for the surface of the substrate. When the alpha step measures the height over the desired range, the two scratches are used to level the measurement (since the whole apparatus often will be tilted slightly) and also provides a reference for the thickness of the organic layer.

To measure the fluorescence, a Jobin Yvon-Spex FluoroMax-2 was used. To measure the thin film fluorescence, the thin film sample was excited using a wavelength of light near the maximum absorption of the material. For polythiophene films, the excitation wavelength was chosen to be 530 nm. The emission spectrum was recorded from 545 - 900 nm, using a 1 nm output slit width and 1 s integration time.

For scanning electron microscopy (SEM), transmission electron microscopy (TEM), and atomic force microscopy (AFM), the facilities at the Canadian Centre for Electron Microscopy were used with the help of the staff. The SEM used was a JEOL-7000F in secondary electron mode. The TEM was a JEOL JEM-2010F in bright field. The AFM was a Digital Instruments Multimode AFM in tapping mode.

# Chapter 3

## Solution Processed Organic Photovoltaic Devices

The following section describes experiments conducted in the lab with regards to solution processed organic photovoltaic devices. This section deals only with work done in the lab, and unless otherwise stated, is my unpublished work done at the Xerox Research Centre of Canada (XRCC). Significant portions of Section 3.4 and 3.5 are taken from published peer-reviewed papers, with some additional work that was removed from publication due to length constraints presented here.

### 3.1 Materials

The materials used in the fabrication of solution processed PV devices can be categorized as: electron donating polymers, electron accepting fullerenes, buffer layers, and solvents. In all cases, aluminum was used as an evaporated metal cathode.

Two electron donating polymers were used in experiments, both of which are polythiophene derivatives: poly(3,3'-didodecylquaterthiophene) (PQT-12) and poly(3-hexylthiophene) (P3HT). As discussed in Section 1.5.3, P3HT is a commonly used material for solution processed PV devices. In order to examine the effects of various solution and film preparation techniques on device performance at the XRCC lab, P3HT was used first as a benchmark to establish the capabilities of the laboratory to

see if it was possible to match the best results reported in literature given the equipment present. PQT-12 is a polymer that was synthesized at XRCC and is similar in structure to P3HT. It has shown similar absorption spectra, hole mobility and performance when used as the semiconductor in OFETs [93]. One particular advantage of PQT-12 is its stability in oxygen, as tested by degradation studies of OTFT's, due to its larger ionization energy [94]. Due to this potential for stability, the primary study of this section pertains to PQT-12 based PV devices (see Section 3.4 and 3.5). The molecular structure of PQT-12 and P3HT is shown in Figure 3.1.

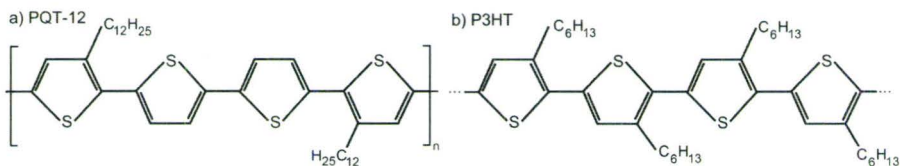


Figure 3.1: Molecular structure of a) PQT-12 and b) P3HT

In terms of solution and film preparation, P3HT and PQT-12 are quite similar, with PQT-12 being differentiated by gelling at room temperature and requiring elevated temperatures to stay in solution. Cast films of PQT-12 will be purple in appearance, whereas a hot solution of PQT-12 will appear red. Figure 3.2 shows the UV-visible absorption spectra for a hot solution, cold solution and cast film (solvent used was chlorobenzene). It is clear that hot dissolved PQT-12 has a Gaussian absorption spectra, characteristic of a statistical distribution of individual polymer molecules separated from each other by the solvent. Upon cooling, the polymers have a tendency to aggregate, redshifting their absorption spectra and resulting in aggregate peaks at 560 nm and 610 nm, the latter of which is related to a charge-transfer (C-T) transition from the HOMO of PQT-12 to the LUMO of chlorobenzene [94]. Upon casting, the solvent is removed and the 610 nm C-T peak disappears, while the main peak redshifts further to 540 nm with shoulders appearing at 500 nm and 580 nm due to further molecular aggregation similar to j-aggregates. The solid film spectrum also broadens with respect to the hot solution spectrum. The redshift and broadening of absorption is characteristic of extended delocalization as a result of

electronic interaction of closely assembled molecules [95]. Since casting a film causes a rapid reduction in temperature (due to the low volume, high surface area) it is likely that the hot solution quickly becomes a cold aggregate dispersion before the solvent is removed entirely. This hypothesis is supported by the fact that spin coated films of PQT-12 are purple within seconds of spinning, despite starting at elevated (100 °C) solution temperatures. This is not the case for P3HT, which remains a red-orange colour for significant periods of time after the film has dried and will crystallize with annealing.

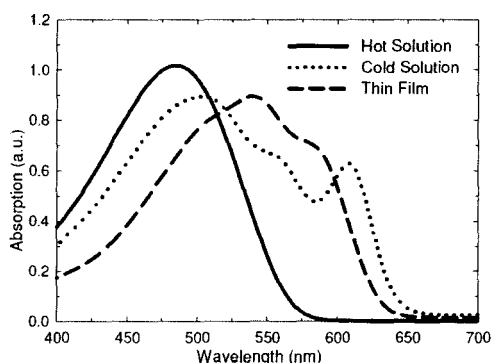


Figure 3.2: UV-vis spectra for hot solution, cold solution, and cast film of PQT-12

The electron accepting fullerene derivative, [6,6]-phenyl- $C_{61}$ -butyric acid methyl ester (PCBM), was described in Section 1.5.3. It was purchased from Nano-C and its molecular structure was shown in Figure 1.7.

A buffer layer that is used for both P3HT and PQT-12 based OPV is the water soluble poly(3,4-ethylenedioxythiophene): poly(styrenesulfonic acid) (PEDOT:PSS). The grade purchased and used was Baytron PH500, from Sigma Aldrich. PEDOT:PSS is a hole conductor with a work function near that of ITO, which aids in the injection of holes from the HOMO of the polymer into the ITO. It also will smooth out the usually rough ITO surface. Further, because of its asymmetric hole conducting nature, it acts as an electron blocker.

The solvent chosen for the casting of these materials is important since it must dissolve the polymer and fullerene, but must not dissolve the buffer layer (PE-

DOT:PSS). Since toluene has been shown to yield comparatively poor performance [53], chlorobenzene and 1,2-dichlorobenzene were chosen as the preferred solvents. These were HPLC grade from Sigma Aldrich.

## 3.2 Fabrication Techniques

To fabricate solution processed organic PV devices, a common procedure was used for all materials with regards to solution and film preparation. These techniques are critical to the performance of the device and are an iteration of previous best-practices used throughout the duration of the project.

After the extensive cleaning procedure described in Section 2.1.2, substrates are coated with a  $\sim 30$  nm PEDOT:PSS layer. This is done by diluting the Baytron PH500 PEDOT:PSS with de-ionized water (3:2), since failure to dilute the solution results in too thick of a layer. The solution is filtered through a  $1\ \mu\text{m}$  glass filter directly onto the substrate, which has the cathode pads and edges of the ITO fingers masked by tape. The spin coater is then turned on, without a ramp-up time, to 1000 rpm for 60 s. The tape is then removed from the substrate, and the substrate is then put in a Petri dish and placed inside the glovebox, where it is annealed on the hotplate for 20 minutes at  $120\ ^\circ\text{C}$ .

Concurrently, the active layer solution is prepared. Since the quantity of polymer and fullerene required is very small for each device, the solutions are prepared by making stock solutions of polymer and fullerene first, then mixing the solutions. This allows for tighter control of composition and concentration. For example, a standard solution of 20 mg/mL, P3HT:PCBM (1:1) is made first by measuring  $\sim 10$  mg of P3HT, and  $\sim 10$  mg of PCBM into separate vials, with the appropriate mass of solvent added. This helps control the composition because measuring the exact mass for both solids is very difficult with such small quantities of material. Both stock solutions are then dissolved using a heat gun and manual shaking. A third vial is then used to mix P3HT and PCBM stock solutions in the desired proportions to control the composition of the solution. If desired, the concentration can also be lowered by adding more solvent at this point. This third vial is then heated and shaken again to

promote mixing of the solutions, and can be sonicated at an elevated temperature. The solution is then filtered through a 1  $\mu\text{m}$  glass filter into a fourth vial that has been cleaned in parallel with the substrates (i.e. isopropanol vapour and heating). This fourth vial is then kept at an elevated temperature on the hotplate inside the glovebox to reduce its exposure to water vapour and oxygen. This active layer solution is then used for casting films. This method is preferable to direct filtration of the solution onto the substrate, since the very-high surface area of the filter results in rapid cooling of the solution and often forms significant bubbles, resulting in uneven films. This effect is especially pronounced for PQT-12 solutions, which forms a gel upon cooling.

Once the PEDOT:PSS coated slide has annealed for 20 minutes, the backside of the substrate is mounted to a glass slide using tape, which also masks the cathode pads and edges of the ITO anodes. The glass slide prevents the formation of a ring pattern in the film. This pattern is a result of faster heat conduction in the area of the substrate that is directly in contact with the metal spin coater chuck. Before spin coating the active layer, the glovebox is purged with a constant flow of nitrogen to reduce oxygen content to  $\sim 1000$  ppm, which was the limitation for the glovebox. The active layer solution is then applied to the substrate, and the spin coating is performed at the desired rpm and time (often 1000 rpm for 60s). Once the backside glass and tape are removed from the substrate, it is placed in a Petri dish inside a vacuum dessicator for the 5 minute trip to the cathode deposition system. This is done because a thin film has a very high surface area to volume ratio, and exposure to ambient air and UV light can cause degradation of the electronic properties of the film. Deposition of the Al cathode is then performed using the equipment described in Section 2.2.2, typically yielding a cathode  $\sim 50$  nm thick.

### 3.3 P3HT/PCBM Solar Cells

The following section describes unpublished work performed on P3HT/PCBM solar cells, and is meant to establish a benchmark for device performances achieved in the lab at XRCC. Further, general trends in fabrication techniques are discussed. The highest power conversion efficiency achieved in this project was 3.5%.

The optimal P3HT/PCBM solar cell was fabricated using a 1:1 P3HT:PCBM, 20 mg/mL solution in 1,2-dichlorobenzene heated to 80 °C, spun at 1000 rpm for 60s. The annealing conditions that yielded optimal results were 140 °C for 10 minutes.

### 3.3.1 Solution Temperature

The temperature of the active layer solution had a significant effect on the PV performance of the device. At elevated temperatures, the P3HT does not crystallize immediately upon dropping onto the substrate (since the temperature is high, both polymer and fullerene remain in solution), resulting in better incorporation of PCBM into the P3HT matrix. This results in better current collection because of higher interfacial area, yet similar  $R_s$  due to good charge transport properties resulting from the crystallization of P3HT during annealing. At lower temperatures, the P3HT tends to crystallize before the 60 s spin is completed, as evidenced by the colour change in the film. This leads to P3HT and PCBM clusters that may be efficient at transporting charge but are not as intimately mixed, resulting in lower exciton separation efficiency and hence lower current generation. At too high of a temperature, the viscosity of the solution is lowered, reducing the thickness of the cast layer and resulting in good  $R_s$ , but low current generation due to low absorption. These results are depicted in Figure 3.3 and Table 3.1, where all slopes at the  $V_{oc}$  are similar but have different  $J_{sc}$ .

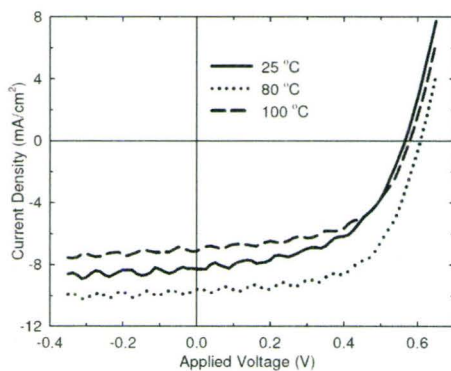


Figure 3.3: Varying solution temperature and the resultant J-V response

Temp. (°C)	$J_{sc}$ (mA/cm <sup>2</sup> )	$V_{oc}$ (mV)	FF (%)	PCE (%)
25	8.3	566	53	2.50
80	9.6	608	61	3.54
100	7.1	579	55	2.26

Table 3.1: J-V parameters for varying P3HT/PCBM solution temperature

### 3.3.2 Solution Concentration

The solution concentration also affected the PV device performance, mostly by varying the thickness of the cast layer. At high concentrations, the cast layer is thicker, resulting in a higher series resistance and also a lower built-in field due to the increased distance between electrodes. These have the effect of simultaneously reducing the charge collection efficiency while increasing the relative amount of recombination, yielding a lower current and fill factor. At low concentrations, although series resistance is lowered and separation efficiency is improved, too low of a concentration results in a film that is not thick enough to absorb a significant portion of light. This results in decreased current generation. Therefore, there is a tradeoff between light absorption and efficient separation and transport. These results are depicted in Figure 3.4 and Table 3.2.

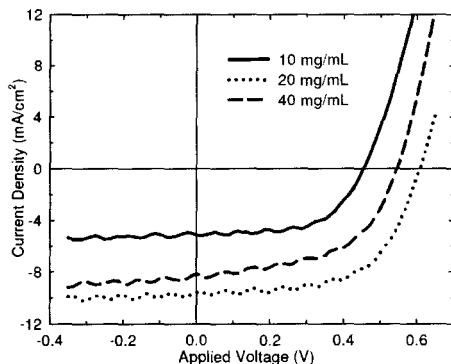


Figure 3.4: Varying solution concentration and the resultant J-V response

Concentration (mg/mL)	$J_{sc}$ (mA/cm <sup>2</sup> )	$V_{oc}$ (mV)	FF (%)	PCE (%)
10	5.1	454	58	1.37
20	9.6	608	61	3.54
40	8.2	546	55	2.45

Table 3.2: J-V parameters for varying P3HT/PCBM solution concentration

### 3.3.3 Spin Speed

The spin speed has a similar effect as the solution concentration, in that the differences in the resulting film thicknesses lead to differences in the PV performance. At low spin speeds, the resulting film is too thick, characterized here by good current generation but poor  $R_s$ . The effect is exacerbated by the fact that a slowly spun film will have more trapped solvent in the film, screening the electric field and further reducing transport efficiency [96]. At high spin speeds, the resulting film is again too thin, decreasing the light absorption and hence the efficiency. These results are depicted in Figure 3.5 and Table 3.3.

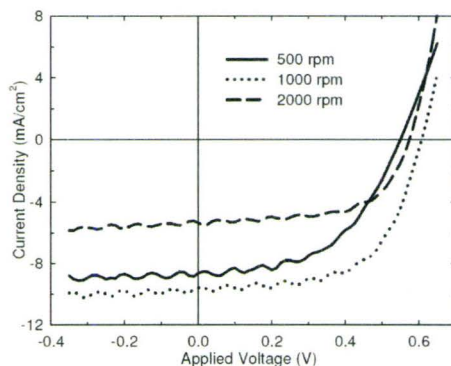


Figure 3.5: Varying spin speed and the resultant J-V response

Spin Speed (rpm)	$J_{sc}$ (mA/cm <sup>2</sup> )	$V_{oc}$ (mV)	FF (%)	PCE (%)
500	8.7	550	52	2.47
1000	9.6	608	61	3.54
2000	5.3	575	61	1.86

Table 3.3: J-V parameters for varying P3HT/PCBM solution spin speed

### 3.3.4 Annealing

The benefit of thermal annealing P3HT:PCBM devices has been well documented in the literature [32,51,66]. Since the mobility is highly dependent on the orientation of the polymer chains, charge conduction is greatly improved with annealing since it provides the energy for those polymer chains to be able to crystallize into clusters. In this study, it was found that devices that were annealed after the cathode was deposited outperformed devices that were annealed before the cathode was deposited. This is likely because annealing the sample with the cathode present allowed for the crystallization of P3HT under an electric field (established by the dissimilar metal contacts). This helps align polymers chains, and also helps form a proper contact with Al [66]. Further, it helps to restrict the polymer from moving vertically due to the presence of the metal. Annealing before cathode deposition also has the benefit of aiding crystallization, albeit in a more random, less confined nature. This results in a rougher surface, which, when the cathode is deposited, results in gaps and voids. This leads to less intimate contact between the film and the Al, increasing the series resistance. This is shown in Figure 3.5 and Table 3.4. Annealing also aids removal of trapped solvent, increasing the internal electric field since a solvent acts as a dielectric screener of the electric field [96].

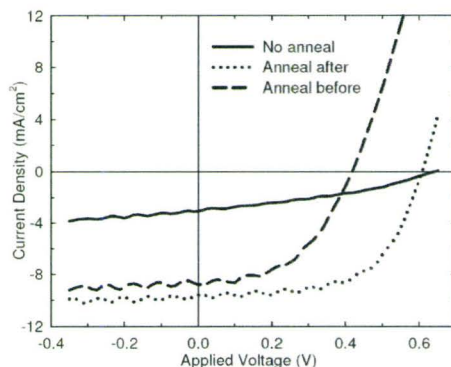


Figure 3.6: Varying annealing conditions and the resultant J-V response

Annealing Condition	$J_{sc}$ (mA/cm <sup>2</sup> )	$V_{oc}$ (mV)	FF (%)	PCE (%)
No anneal	3.1	641	35	0.69
Anneal after	9.6	608	61	3.54
Anneal before	8.8	418	49	1.79

Table 3.4: J-V parameters for varying P3HT/PCBM annealing conditions

### 3.3.5 Lithium Fluoride Buffer Layer

The insertion of an interfacially thin (0.5 nm) LiF layer in between the active layer and the Al cathode served to increase the fill factor, especially in unannealed devices (see Figure 3.7 and Table 3.5). Without a LiF layer, the cathode in an unannealed device forms a poor contact with the film, and results in nearly no diode behaviour, resulting in very low fill factors. The insertion of a LiF layer aids in electron transfer from the LUMO of PCBM to the Al, and also acts as a hole blocker [64]. However, annealing of a device with a thin LiF layer does not dramatically increase the PV performance, with only a slight increase in the current generation. Films with a thin LiF layer showed noticeably less roughening after annealing, with the LiF possibly serving to further restrict the vertical movement of the polymer. Note that the

IV curve for the annealed Al-only cell, with its lower current and voltage, is different from those used in the previous spin condition comparisons. This cell had a deposited Al layer using the same multi-boat thermal evaporator (as opposed to the bell jar evaporator) that was used to deposit a LiF/Al layer. This multi-boat evaporator deposits Al at a lower rate than the bell jar evaporator, which may lead to faster oxidation of the cathode and generally leads to worse ohmic contacts. It is possible to deposit a thin LiF layer in the multi-boat thermal evaporator, break vacuum, and then transfer the sample to the bell jar evaporator for Al deposition. However, this would introduce another variable in the exposure of the film and LiF to air and dust, which is especially important considering the low thickness of the LiF layer. Since the experiment was the comparison of an LiF/Al contact with an Al-only contact, keeping the Al deposition conditions in common was more important than seeing the effect on the best-case scenario.

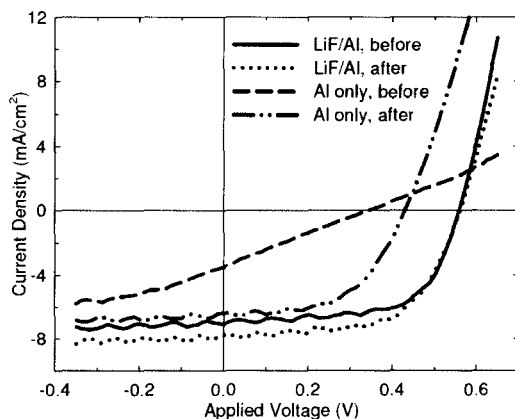


Figure 3.7: Effects of the insertion of a thin (0.5nm) buffer layer of LiF on J-V response

Cathode & Annealing Condition	$J_{sc}$ (mA/cm <sup>2</sup> )	$V_{oc}$ (mV)	FF (%)	PCE (%)
LiF/Al, before	7.1	559	63	2.51
LiF/Al, after	7.8	562	62	2.70
Al only, before	3.5	345	24	0.29
Al only, after	6.4	431	55	1.51

Table 3.5: J-V parameters for varying P3HT/PCBM cells with LiF/Al cathodes, before and after annealing

The insertion of a LiF layer also improves the stability of the device. When unencapsulated devices were manufactured with a 0.5 nm LiF buffer layer in between the film and cathode, the performance of the device remained stable over 88 hours of continuous AM1.5G exposure in a flowing nitrogen environment. Over the same period of time, a film with a bare Al contact decayed significantly. It is possible that in addition to acting as a physical barrier to the diffusion of water and oxygen, its effect on reducing roughening of the annealed film also contributes to reducing the surface area where oxygen and water can diffuse. In addition, the more efficient charge collection would also lead to less space charge in the film, reducing the likelihood of oxidation of excited species.

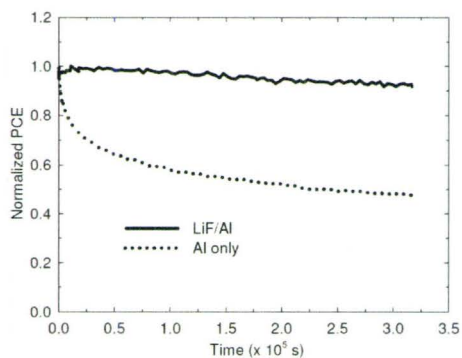


Figure 3.8: Effect of the insertion of a thin (0.5nm) buffer layer of LiF on PV performance stability

## 3.4 Blend Composition Study of PQT-12/PCBM Organic PV Devices

This section is based on a published article (document A in preface), “Blend composition study of poly(3,3′′-didodecylquaterthiophene) / [6,6]-phenyl-C<sub>61</sub>-butyric acid methyl ester solution processed organic solar cells”, A.P. Yuen, A.M. Hor, R.A. Klenkler, J.S. Preston, E.R.Q. Macabebe, E.E. van Dyk, R.O. Loutfy, *Journal of Applied Physics*, v. 105, p. 016105 (2009). It describes the effect of changing the ratio of donor and acceptor concentration on the power conversion efficiency. Of the four factors that affect efficiency, the primary focus of this section is on (4) charge transport. Since PQT-12 is a relatively new polymer, this article was one of the first exploratory papers on PQT-12/PCBM solar cells.

Photovoltaic devices made from blends of poly(3,3′′-didodecylquaterthiophene) (PQT-12) and [6,6]-phenyl-C<sub>61</sub>-butyric acid methyl ester (PCBM) have been fabricated and characterized. By varying the polymer loading in the blend, an optimal power conversion efficiency (PCE) of 0.70% has been achieved for a blend consisting of 15 wt% PQT-12, which is an order of magnitude higher than the PCE for a 50wt% blend. The apparent reason for the large difference is the fact that blends with higher PQT-12 loading are transport limited, with much larger hole-to-electron mobility ratios.

### 3.4.1 Experimental Details

In this study, PQT-12 is blended with [6,6]-phenyl-C<sub>61</sub>-butyric acid methyl ester to produce a solution processed organic solar cell. Specifically, we have investigated the effect of PQT-12/PCBM blend composition on the power conversion efficiency (PCE) by examining full spectrum I-V characterization, external quantum efficiency (EQE), and photoconductive time-of-flight (TOF).

Water-soluble poly(3,4-ethylenedioxythiophene): poly(styrenesulfonic acid) (PEDOT:PSS) was spun onto the substrates to form a ~30 nm layer. PQT-12/PCBM solutions were prepared by dissolving PQT-12 in 1,2-dichlorobenzene, then adding

PCBM to form the desired blend composition at a solid concentration of 24 mg/mL. The solution was then spin coated at 1000 rpm for 60s, forming an active composite layer ( $\sim 100$  nm) that was then capped with a thermally evaporated aluminum electrode at a chamber pressure of  $\leq 2 \times 10^{-3}$  Pa. Five different wt% of PQT-12 were examined: 5, 15, 25, 35 and 50 wt%, with the device structures shown in Figure 3.9. Unless specifically stated otherwise, all usage of wt% refers to the mass percentage of PQT-12 as a fraction of the total mass of solids in the solution, with the remainder of the solid being PCBM. A TEM cross section image is shown in Figure 3.10.

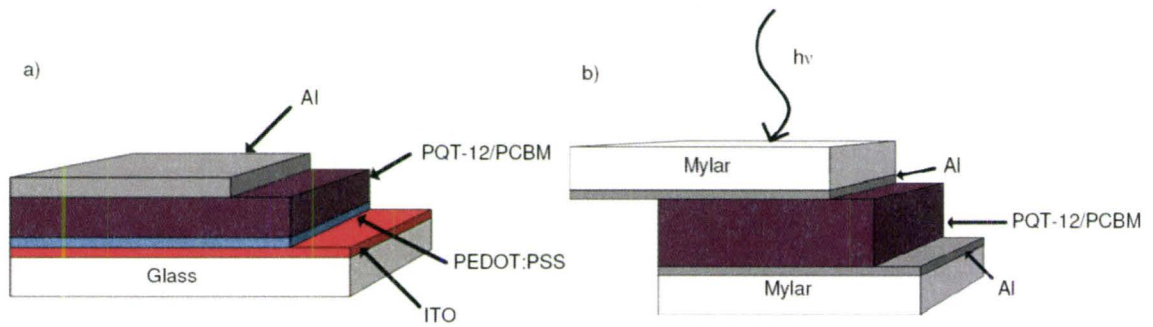


Figure 3.9: Device structure for a) I-V and EQE and b) Time-of-Flight measurements (not to scale)

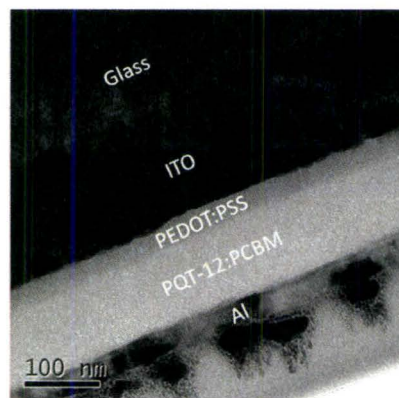


Figure 3.10: TEM cross section of a completed device

### 3.4.2 Current-Voltage

The J-V characteristics for the five blends are shown in Figure 3.11a and Table 3.1, with current densities,  $J$ , calculated by dividing the currents by active area. Despite the obvious advantage of more light-absorbing polymer, devices with 50 wt% PQT-12 show a PCE an order of magnitude lower than cells at 15wt% PQT-12, reaching a maximum at PCE = 0.70%. In comparison, studies have shown that P3HT/PCBM systems benefit from a 50-50 wt% blend [97]. This low optimal PQT-12 wt% is comparable to other studies showing an optimal polymer/PCBM ratio of 1:4, as is the case for MDMO-PPV [98] and pBTTT [99].

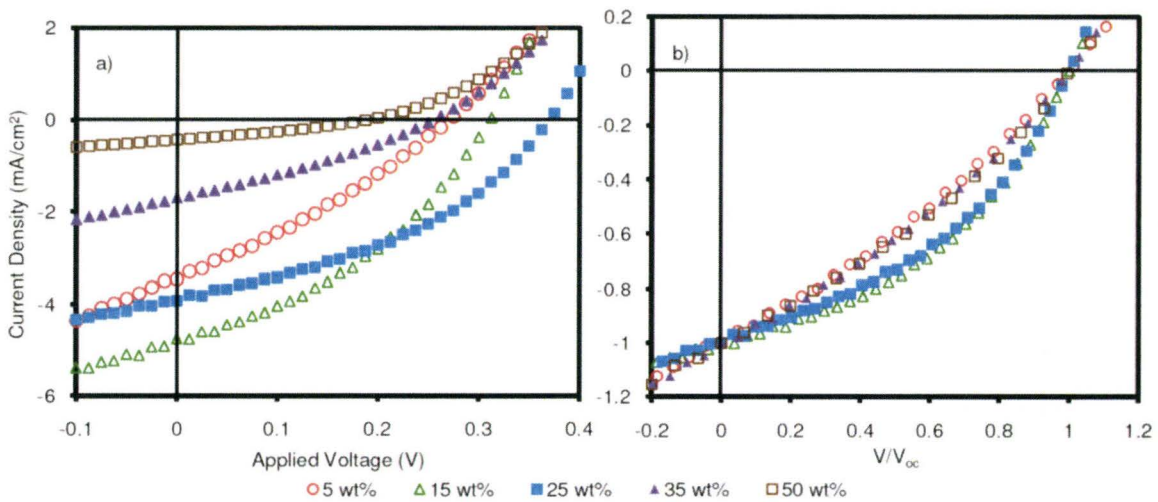


Figure 3.11: a) J-V response for varying PQT-12 wt% devices in simulated AM1.5G sunlight,  $100 \text{ mW/cm}^2$ , b) I-V responses, normalized for each  $I_{sc}$ , demonstrating higher fill factor for 15wt% and 25wt% blends.

By analyzing the normalized I-V data (Figure 3.11b), the shunt and series resistances for each blend composition can be directly compared. Examination of the inverse slope of the I-V responses at the short circuit current and open circuit voltage provides an approximation of the shunt and series resistances [31]. Comparing the  $R_s$  (see Figure 3.12) for each blend composition implies that 15 wt% and 25 wt% blends have the most efficient charge transport, with  $R_s$  increasing noticeably when the polymer composition rose above 25 wt%.

PQT-12 wt%	$J_{sc}$ (mA/cm <sup>2</sup> )	$V_{oc}$ (V)	FF (%)	$R_s$ ( $\Omega$ cm <sup>2</sup> )	PCE (%)
5	3.45	0.27	30	53	0.28
15	5.05	0.34	41	24	0.70
25	3.91	0.37	39	35	0.57
35	1.70	0.26	31	83	0.14
50	0.43	0.19	31	250	0.03

Table 3.6: J-V parameters for different compositions of PQT-12/PCBM

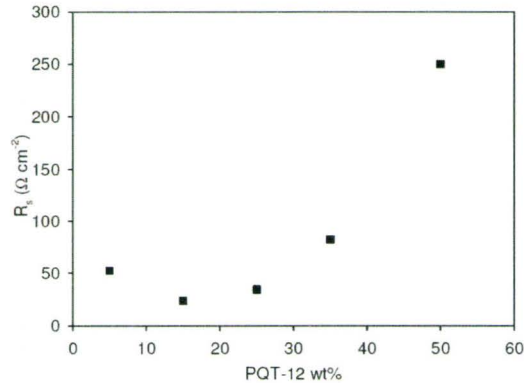


Figure 3.12: Series resistance approximation as a function of the PQT-12 wt% loading

### 3.4.3 UV-visible Absorption & EQE

Based on the UV-visible absorption spectrum of the thin films alone (Figure 3.13a), the 50 wt% blend should have a notable advantage over the lower wt% blends due to its stronger absorption in the visible regime. The absorption spectra are fairly linear with increasing polymer, showing increased absorption around 535 nm and decreased absorption around 335 nm. This is because of the increase in the relative amount of polymer with the simultaneous decrease in the relative amount of fullerene. Another notable feature of Figure 3.13a is the redshift of the PQT-12 absorption peak with increased polymer loading, with a 50wt% film demonstrating a nearly identical profile as a pristine PQT-12 film, as shown in Figure 3.13b. The shoulder peak at 580nm for both the pristine film and 50 wt% blended film demonstrates the formation of red-shifted aggregates of polythiophene chromophores, indicating that even high

PCBM loading (1:1) is not sufficient to disrupt this aggregation. In addition, the spectrum for a cold PQT-12 solution is not only red-shifted with respect to a hot solution, but also exhibits a shoulder at 565 nm, indicating the interplane interaction [100] or segmental aggregation of polythiophene chromophores. These observations all imply that, if the performance of the device was solely determined by the match to AM1.5G, a higher wt% should yield the best power conversion efficiencies.

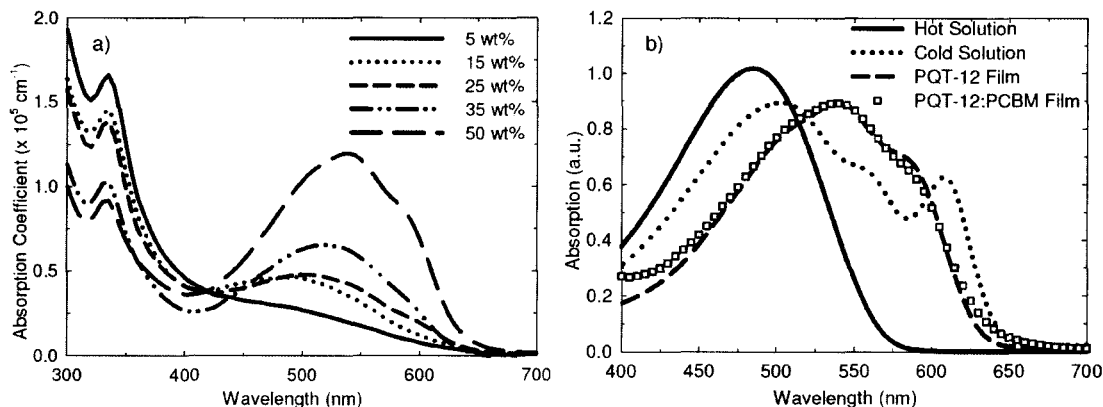


Figure 3.13: a) UV-visible absorption of spin-coated PQT-12/PCBM films of varying PQT-12 wt%, b) UV-visible absorption of PQT-12 solutions, pristine film, and blended PQT-12-PCBM film

An examination of the external quantum efficiency (EQE) for the various blend compositions (Figure 3.14) gives further insight into the carrier transport in the film. It is clear that as the polymer wt% decreases, external quantum efficiency increases until it reaches a maximum at 15 wt%. Further, the shifting of the action spectra peaks from the absorption peak is indicative of unipolar transport. This is due to a weaker absorption coefficient, meaning that the average depth of exciton generation is further from the ITO electrode and therefore represents a shorter distance for electrons to travel to the cathode. In addition, it is clear from Figure 3.14 that the 35 wt% blend is near the limit for efficient transport and 50 wt% is clearly transport limited. This is presumably the reason for poor power conversion efficiency of the higher PQT-12 wt% blends despite much higher optical absorption in the visible spectrum. The implication of this is that at 50 wt% PQT-12, there is an

insufficient amount of PCBM to form a continuous electron transport network, i.e. the percolation threshold for electron transport is  $> 50\text{wt}\%$  PCBM, and is likely around  $65\text{ wt}\%$  PCBM ( $35\text{wt}\%$  PQT-12). It is also interesting to note that among the 5, 15, and  $25\text{wt}\%$  EQE curves, the peak of the EQE in the 400-500 nm regime blueshifts with decreasing polymer loading. From examination of Figure 3.13, this can be interpreted as higher concentrations of PCBM having the effect of isolating PQT-12 molecules, reducing aggregation in much the same way that the absorption spectra of solutions are blueshifted from thin solid films.

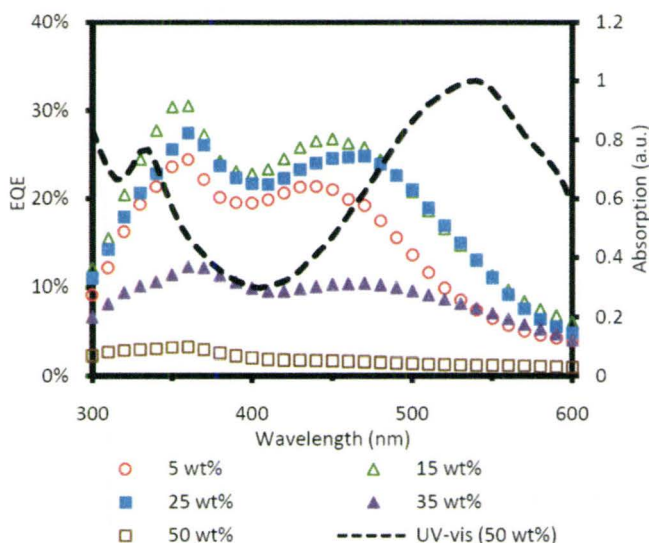


Figure 3.14: External Quantum Efficiency of completed devices for different wt% of PQT-12 with UV-visible absorption of  $50\text{wt}\%$  overlaid.

### 3.4.4 Photoconductive TOF

An examination of the photoconductive TOF properties of the varying blends will yield electron and hole mobilities for the various films (See Figure 3.15 for sample transient, including the determination of the knee of the TOF signal). Similar studies based on field-effect mobilities have shown that a balanced hole-to-electron mobility ratio will yield the highest power conversion efficiency [101]. A TOF study for the  $15\text{wt}\%$  blend shows a hole mobility of  $\mu_h(15\text{wt}\%) \approx 3 \times 10^{-5} \text{ cm}^2\text{V}^{-1}\text{s}^{-1}$  and an electron

mobility of  $\mu_e(15\text{wt}\%) \approx 3 \times 10^{-6} \text{ cm}^2\text{V}^{-1}\text{s}^{-1}$ . Therefore, the ratio of hole-to-electron mobility is  $\mu_h/\mu_e \approx 10$ . However, at 50 wt%, due to the increased polymer concentration, the hole mobility of the blend increases to  $\mu_h(50\text{wt}\%) \approx 9 \times 10^{-4} \text{ cm}^2\text{V}^{-1}\text{s}^{-1}$ . Owing to the difficulty of acquiring reasonably non-dispersive transients for electrons in 50wt%, the electron mobility is not reported here. However, it is reasonable to assume that a decrease in the amount of electron-transporting PCBM can only serve to decrease the electron mobility [8]. Even if the electron mobility did not decrease, the rise in hole mobility immediately indicates an even more imbalanced charge transport with a mobility ratio of  $\mu_h/\mu_e > 300$ . It is possible that further decreasing the PQT-12 loading will further balance the hole and electron mobility. However, due to the difficulty of preparing suitably thick films for TOF measurements from low-viscosity blends (e.g. 5wt%), this hypothesis was not immediately verifiable.

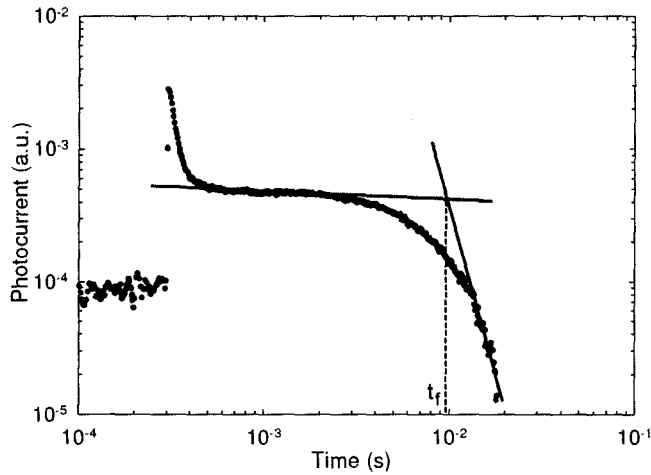


Figure 3.15: Sample transient for TOF measurements (15wt% PQT-12), where the knee ( $t_f$ ) is determined by the intersection of the two linear regions

### 3.4.5 AFM Imaging

In order to examine the surface roughness of the films, AFM images were acquired for 15wt% and 50wt% films (Figure 3.16 and 3.17). Examining the phase images (right side panel of each image) shows the noticeably rougher surface in 50wt% films compared to 15wt% films. A high degree of roughness results in uneven internal

electric fields after the cathode is deposited, as well as less intimate contact between the cathode and the film. This would tend to increase the series resistance, which is consistent with observations from the I-V data. In addition to a rougher film, there are also large aggregations that exceed 25nm in height. Considering the whole active layer film is only  $\sim 50$  nm thick, a 25 nm cluster is a significant deviation. This would result in increased short circuiting, lowering the shunt resistance. This is again consistent with observations from the I-V data. Further, the aggregation of polymer clusters would lead to increased charge trapping and quenching of photoexcitation.

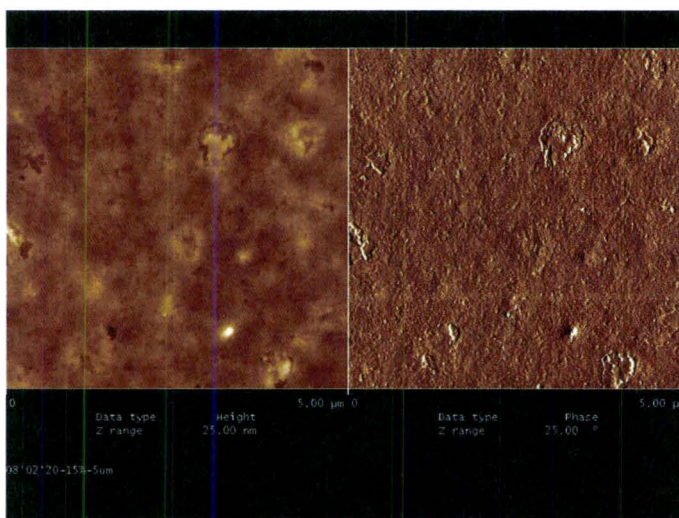


Figure 3.16: AFM image of the surface of a 15wt% PQT-12/PCBM film

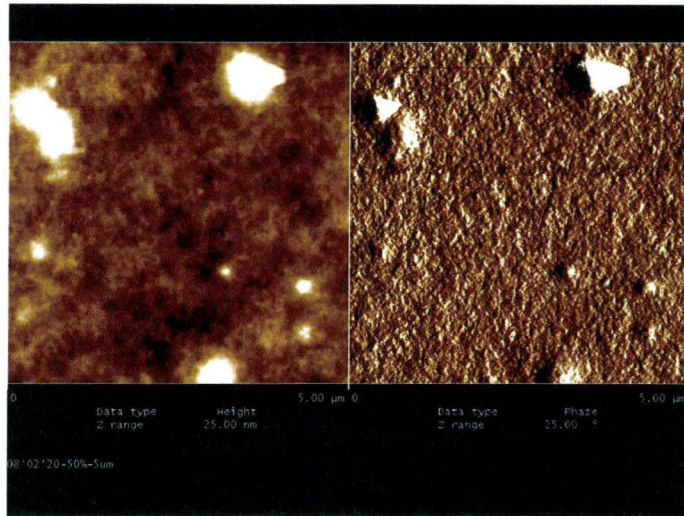


Figure 3.17: AFM image of the surface of a 50wt% PQT-12/PCBM film

### 3.4.6 Summary

In summary, PQT-12/PCBM bulk heterojunction photovoltaic devices of varying blend compositions were fabricated. It was determined that the PQT-12 loading that yielded the highest PCE was 15 wt%. Despite the increased absorption of the 50wt% blend in the visible regime, the PCE was an order of magnitude lower than that of the 15wt% blend. This is likely attributed to the greater imbalance between hole and electron mobility as PQT-12 concentration is increased, as demonstrated by an analysis of both the EQE and hole/electron mobility measured by TOF. In addition, the EQE spectrum indicates that 35wt% PQT-12 is near the percolation threshold for efficient electron transport in PCBM. Finally, TOF measurements confirm that a heavily PCBM loaded blend is likely to yield more balanced carrier transport in a PQT-12/PCBM system.

## 3.5 Decay Study of PQT-12 based solar cells

The following section is based on an article (document B in preface), “Improved stability of solution processed photovoltaic devices using PQT-12”, A.P. Yuen, A.M.

Hor, S.M. Jovanovic, J.S. Preston, R.A. Klenkler, N.M. Bamsey, R.O. Loutfy, *Solar Energy Materials & Solar Cells*, v. 94, p. 2455 (2010). The purpose of this section is to investigate the performance stability of organic solar cells using PQT-12 as opposed to P3HT. This section does not describe one of the four factors affecting power conversion efficiency, but is relevant to the potential usefulness of PQT-12 in organic solar cells. To the best of our knowledge, this is the first paper directly measuring the PQT-12 device stability.

Photovoltaic devices made from blends of electron donating poly(3,3'' - didodecylquaterthiophene) (PQT-12) and electron accepting [6,6]-phenyl-C<sub>61</sub>-butyric acid methyl ester (PCBM) are fabricated, and the device performance is measured over a period of 88 hours to determine device stability. Results are compared against similar devices incorporating P3HT as the electron donor. Devices based on PQT-12 demonstrate a significant improvement in device stability, with a calculated half-life of 190,000 hours when operated in an inert environment. A fluorescence study is also conducted on bare films of PQT-12 and P3HT, and show that the PQT-12 films are significantly more stable to air than P3HT. In addition, given the slower decay of bare films stored in vacuum, the results indicate that the exposure of the active layer to air is a significant contributor to performance decay of completed devices.

One significant challenge for OPV is the photostability of the devices, as many of the materials used in OPV degrade in ambient air and UV light. One particularly important OPV material, poly(3-hexylthiophene) (P3HT), has become one of the most studied materials in the field of organic electronics due to its excellent relative performance in organic thin film transistors (OTFT) [102] and organic light emitting devices (OLED) [103]. P3HT is a conjugated polymer that acts as an electron donor and has demonstrated high hole mobility ( $0.1 \text{ cm}^2\text{V}^{-1}\text{s}^{-1}$ ) [104], strong absorption in the visible regime [105], and has yielded photovoltaic power conversion efficiencies (PCE) as high as  $\sim 5\%$  in a single junction [1, 106, 107]. However, a flaw with P3HT is the rapid degradation of the material in ambient conditions, necessitating effective encapsulation for long term stability [108, 109]. While encapsulation can help to slow the degradation of device performance, it would be desirable to find a material that is inherently more stable and can therefore replace P3HT as the electron donor.

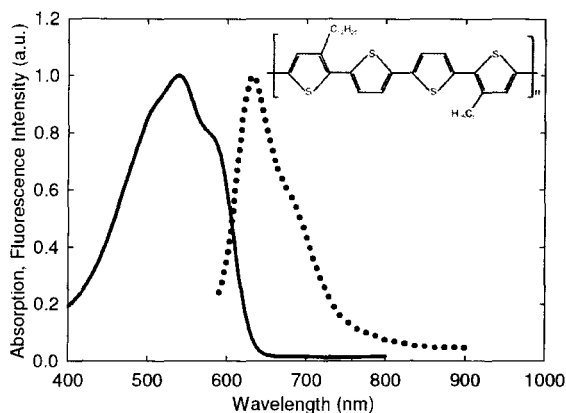


Figure 3.18: Absorption (solid line), fluorescence (dotted line), and molecular structure (inset) of PQT-12. Absorption and fluorescence measured for spin coated thin film.

A relatively new polymer, poly(3,3''-didodecylquaterthiophene) (PQT-12, see Figure 3.18), is structurally similar to P3HT with similar HOMO and LUMO levels, absorption profile, and hole mobility [93]. It has shown both excellent OTFT performance as well as enhanced OTFT stability due to its larger ionization energy [94]. Thus far, some attempts have been made to use PQT-12 as the electron donor in OPV [110–113] though efficiencies are thus far limited to  $\sim 1\%$  due to nano-phase crystallization that excludes PCBM in cast films [113, 114]. However, with its higher hole mobility and large absorption coefficient, there is no immediately evident reason that PQT-12 cannot outperform P3HT given optimized film casting conditions that take into consideration the size and distribution of nano-phase domains for bicontinuous hole and electron transport.

### 3.5.1 Experimental Details

This experiment reports on the use of PQT-12 as an electron donor substitute for P3HT in organic solar cells. PQT-12 is blended in solution with electron accepting [6,6]-phenyl-C<sub>61</sub>-butyric acid methyl ester (PCBM) to form a bulk heterojunction. The unencapsulated cell is then continually exposed to simulated AM1.5G sunlight and its photovoltaic performance is measured over a period of 88 hours. For compar-

ison, a P3HT cell is also fabricated. Our results show a marked improvement of the stability of the PQT-12 based cell as compared to the P3HT based cell. In order to determine the inherent effects of ambient exposure on the polymers themselves, the fluorescence yield of bare spin coated films of PQT-12 and P3HT are measured.

Samples for I-V measurements were prepared on patterned indium tin oxide (ITO) ( $\sim 15 \Omega/\square$ ) coated aluminosilicate glass substrates. Water-soluble poly(3,4-ethylenedioxythiophene): poly(styrenesulfonic acid) (PEDOT:PSS) was spun onto the substrates to form a  $\sim 30$  nm buffer layer and was then annealed at  $120^\circ\text{C}$  for 20 minutes in a low  $\text{O}_2$  ( $<0.3\%$ ), low humidity ( $<1.0\%$ ) glovebox. The PEDOT:PSS coated substrate was not exposed to ambient conditions before the active layer was deposited. Active layer solutions were prepared by dissolving polymer (PQT-12 or P3HT) in chlorobenzene, then adding PCBM to form the desired blend composition at a solid concentration of 20 mg/mL. Composition of P3HT/PCBM devices was 50 wt% P3HT, whereas PQT-12/PCBM devices had a composition of 15 wt% PQT-12. These compositions corresponded to the blends yielding maximum device efficiency [97,110]. The solution was then spin coated at 1000 rpm for 60 s, forming an active layer ( $\sim 50$  nm) that was then capped with a thermally evaporated aluminum electrode ( $\sim 50$  nm, 0.4 nm/s) at a chamber pressure of  $<2 \times 10^{-3}$  Pa. The device was then transferred to a nitrogen-filled sample chamber and illuminated through the ITO electrode with  $100 \text{ mW}/\text{cm}^2$  simulated sunlight using an Oriel 96000 solar simulator with an AM1.5G spectral filter. Input power was monitored with a Newport 818-UV/CM detector and Newport 1830-C optical power meter. Output I-V curves were acquired using a Keithley 238 source-measure unit connected to a personal computer. A LabVIEW program was written to measure the full I-V curve at exponentially increasing time intervals from  $t=0$  to  $t=2$  hours, followed by every hour henceforth up to 88 hours. Each device had an active area of  $7 \text{ mm}^2$  as defined by a shadow mask.

### 3.5.2 Current-Voltage Decay

The results of the photovoltaic performance decay are shown in Figure 3.19. The PCE of each device has been normalized to the initial ( $t=0$ ) value, since the

P3HT/PCBM and PQT-12/PCBM cells yield different initial PCE. The P3HT/PCBM cell yielded a PCE of  $\sim 2.5\%$ , which is a typical value for our lab. The PQT-12/PCBM cell yielded a PCE of  $\sim 0.45\%$ . It is clear that the P3HT based solar cell decays significantly faster than the PQT-12 based solar cell, and in fact has a half life of roughly 65 hours. Our results for the relative decay at 88 hours are roughly equal to those found by other groups [108]. When plotted in a logarithmic scale, the slope of the linear regression of the linear segment of the curve for each device can be used to approximate the half-life for the PQT-12 device. These calculations yield a half-life of  $\sim 190,000$  hours for the PQT-12/PCBM solar cell. It is important to note, however, that this value is obtained in an inert environment, and that our preliminary results indicate that the device stability is significantly reduced when operated in air, with a half-life on the scale of a few hours.

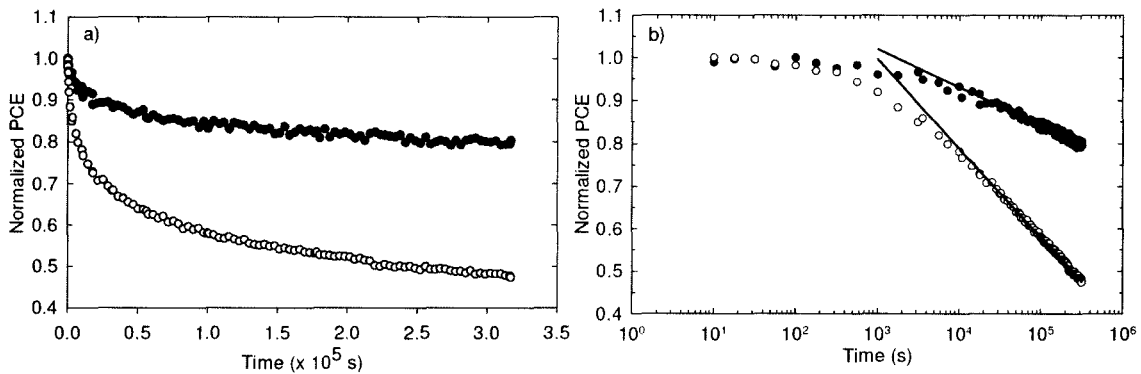


Figure 3.19: Photovoltaic response of PQT-12 (filled circles) and P3HT (hollow circles) as function of time under constant AM1.5G illumination in a) linear scale and b) semi-log scale. Linear fits for both PQT-12 and P3HT data shown in b).

### 3.5.3 Fluorescence Decay

In order to examine the effect of ambient air on the bare polymer films, a fluorescence study was conducted. Thin films ( $\sim 100$ nm) of PQT-12 and P3HT were spin coated on glass substrates, with two samples made for each material. One film from each set was stored in low vacuum when it was not being measured. Similarly, one film from each set was stored in ambient conditions, where it was fully exposed

to air and room lighting. The fluorescence was measured with a Jobin Yvon-Spex FluoroMax-2 using an excitation wavelength of 530 nm, which is near the absorption peak of both P3HT and PQT-12. Figure 3.20 shows the results of the fluorescence study. Fluorescence yields were taken as the fluorescence at peak intensity, as the shape of the fluorescence response did not change over the time frame measured (i.e. no narrowing, broadening, or shifting in peaks over the measured range). The fluorescence yield was taken as a good indicator of stability, since a reduced fluorescence yield indicates the photooxidation of the polymer [115], resulting in decreased conjugation length [116] and disruption to charge transport as a result of the introduction of polar oxidized groups [96]. This lowers hole mobility and device performance. For the P3HT sample stored in ambient conditions, the rapid decay of fluorescence yield is quite evident, with a reduction in fluorescence to 20% of the original in only 1 day. The PQT-12 sample stored in ambient conditions fared much better, with a reduction to only 50% of the original after 1 day and 30% after 4 days. When the samples were stored in vacuum, the fluorescence decay was lessened, indicating that active layer exposure to ambient air is a significant factor in the decay of the device performance. When stored in vacuum, the PQT-12 fluorescence yield remains at roughly 75% of the initial value after 4 days. While the P3HT sample stored in vacuum experiences less fluorescence decay than the P3HT sample stored in air, the vacuum-stored sample still decays to 30% of the initial. In fact, the P3HT sample stored in vacuum has a coincidentally similar fluorescence yield as the PQT-12 sample stored in air, indicating a significant improvement in stability for PQT-12 films. It is also important to note that the fluorescence of the vacuum-stored samples is measured ex-situ, and therefore the films are exposed to air for up to an hour while fluorescence is measured. In addition, low vacuum storage was achieved through a mechanical rotary pump, meaning that there was still likely trace amounts of water and oxygen in the chamber.

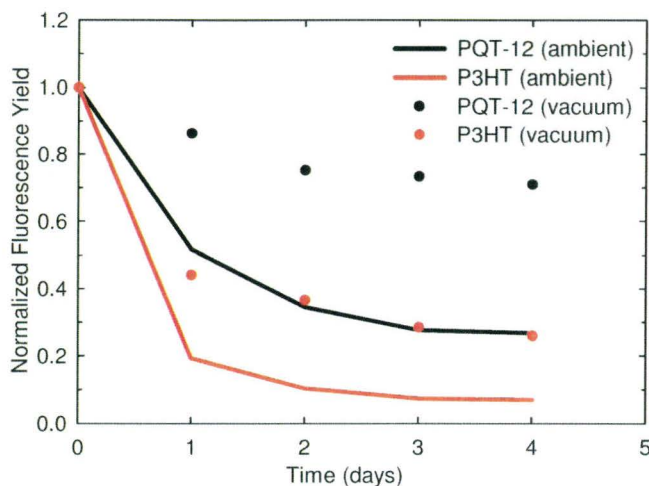


Figure 3.20: Normalized fluorescence yield of bare PQT-12 and P3HT films when stored in vacuum (circles) and in ambient conditions (lines)

It is important to note that the relative fluorescence decay of bare films is much faster than the photovoltaic efficiency decay, especially for P3HT based devices and films. This is likely due to the fact that the deposition of an Al cathode serves as a partial encapsulation, hindering the permeation of oxygen and water vapor into the active layer. Other groups have come to the same conclusion, with air-exposed completed devices being relatively stable while air-exposed bare films with cathodes deposited at a later time exhibited vanishingly small power conversion efficiency [108]. Indeed, our preliminary results demonstrate that, when a PQT-12 film with a 10 nm deposited layer of Al is stored continuously in vacuum for 17 days, there is a negligible ( $\sim 4\%$ ) decrease in fluorescence.

To further examine the difference in photooxidation of P3HT and PQT-12, two bare films of P3HT and PQT-12 were exposed to a UV lamp (365nm peak,  $\sim 20$  mW/cm<sup>2</sup>) in ambient air for 2 minutes (see Figure 3.21). Compared to the initial as-cast results, P3HT films decayed to a fluorescence yield that was 22% of the original. PQT-12 films on the other hand, showed a decay to only 49% of the original, indicating that PQT-12 is more stable to UV-induced photooxidation.

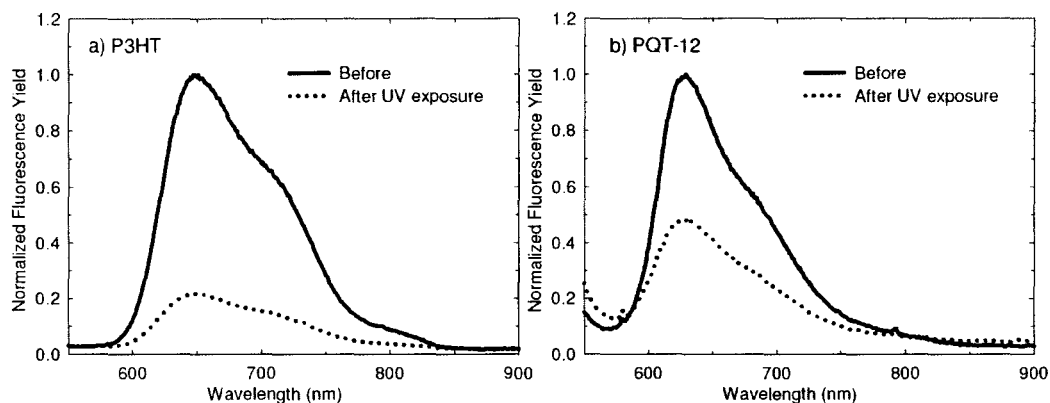


Figure 3.21: Normalized fluorescence decay of a) P3HT and b) PQT-12 after UV exposure

### 3.5.4 Summary

In summary, solar cells with PQT-12 replacing P3HT as the hole conducting polymer demonstrate a significant improvement in the performance stability, with a calculated half life of 190,000 hours when stored in an inert environment. A fluorescence study on bare films of PQT-12 and P3HT was conducted, showing a slower decrease in fluorescence yield for PQT-12 films versus P3HT films when stored in air. The fluorescence decay can be further slowed by storage in vacuum or proper encapsulation. These results indicate that, although the overall PCE of PQT-12 cells is lower than the PCE of P3HT cells, the stability of PQT-12 cells is a significant advantage for the long-term viability of PQT-12 based photovoltaic devices.

## Chapter 4

# Vacuum Coated Organic Photovoltaic Devices

The following section describes experiments conducted in the lab with regards to vacuum coated organic photovoltaic devices. In particular, sections 4.3 and 4.4 have been submitted to peer-reviewed journals, with some additional work that was removed from publication due to length constraints presented here. Sections 4.6, 4.7 and 4.8 were filed as patents to the United States Patent and Trademark Office by Xerox Corp. on Oct. 22, 2010.

### 4.1 Materials & Purification

The materials used in the fabrication of vacuum coated PV devices are: electron donating molecules, electron accepting  $C_{60}$  fullerene, and buffer layers. In all cases, aluminum was also used as an evaporated metal cathode. A group of electron donating molecules was used in experiments, namely M-Phthalocyanines (M-Pc). As discussed in Section 1, M-Pc is an electron donor and is a commonly used group of materials for vacuum coated organic electronic devices, including OPV. The group of M-Pc's all have the same overall molecular structure, with the main difference being the central moiety that can change the molecule's absorption spectra and PV characteristics. In particular, the M-Pc's studied are: monovalent metal free phthalocyanine ( $H_2Pc$ ),

divalent copper, zinc, and magnesium phthalocyanine (CuPc, ZnPc, MgPc), trivalent chloroindium, chloroaluminum, and chlorogallium phthalocyanine (ClInPc, ClAlPc, ClGaPc), and tetravalent vanadyl and titanyl phthalocyanine (VOPc, TiOPc). For a vacuum coated electron acceptor, C<sub>60</sub> fullerene is the only material used in this project. Figure 1.10 showed the molecular structure of both M-Pc and fullerene.

All M-Pc was synthesized by XRCC staff. Fullerene was acquired from MER Corp at 99.5% purity. The buffer layers, MoO<sub>3</sub> (electron blocker) and bathocuproine (hole blocker) were purchased from Sigma Aldrich and were of 99.99% purity. Since the purity of materials can have a large effect on the performance of the device [117], the M-Pc and C<sub>60</sub> were further purified by 3-zone train sublimation as described in Section 2.3.1. The difference between purified and unpurified material was immediately evident, as heating of the unpurified material resulted in degassing of the material, releasing solvent into the chamber and raising the base pressure to as high as  $2 \times 10^{-3}$  Pa. On the other hand, heating of purified material resulted in no significant degassing at  $2 \times 10^{-4}$  Pa.

## 4.2 Fabrication Techniques

Vacuum coated devices were fabricated using the thermal evaporator described in Section 2.3.2. After the extensive cleaning procedure described in Section 2.1.2, substrates were loaded into the thermal evaporator system and the chamber was evacuated for  $\sim 4$  hours (or overnight) to achieve a base pressure of roughly  $2.5 \times 10^{-6}$  Torr. Source materials were heated at below the sublimation point for roughly 5 minutes to ensure that any trapped solvent or moisture was removed before deposition onto the substrate. The desired deposition rate was then input into the deposition controller, which automatically applied the power to achieve and stabilize the deposition rate as seen by the crystal monitor. A geometric correction factor unique to the positioning of each boat relative to the monitor and the substrate is then used to calculate the actual deposition rate as seen by the substrate. When the deposition rate stabilized, the sample shutter was opened to begin deposition. For co-evaporated layers, it was important for both sources to stabilize to the desired rate in order to properly control

composition. Often, different device structures or layer thicknesses for pairs of ITO fingers were desired, and this was achieved by changing the mask positioning. For depositing Al, the cathode mask (which is long enough to connect ground pads on opposite ends) was always used.

### 4.3 Photovoltaic Properties of M-Pc:C<sub>60</sub>

This section describes an article (document C in preface), “Photovoltaic Properties of M-Phthalocyanine / Fullerene Organic Solar Cells”, A.P. Yuen, A.M. Hor, S.M. Jovanovic, R.A. Klenkler, J.S. Preston, G.A. Devenyi, R.O. Loutfy, submitted to Journal of Applied Physics. Of the four factors affecting power conversion efficiency, this section examines factors (1) photovoltage, (3) exciton separation and (4) charge collection. This study is important because much of the work on organic solar cells in the literature has been devoted to solution processed materials despite the excellent stability of metallophthalocyanines (M-Pc) [56, 118] compared to most conjugated polymers. Another advantage of M-Pc is their broad absorption profile in the 650-850 nm range, which is beyond the absorption edge for the most studied conjugated polymers (P3HT [119] and MDMO-PPV [53]).

Photovoltaic devices made from M-Phthalocyanine and Fullerene have been fabricated and characterized by current-voltage response, lateral time-of-flight photoconductivity, UV-visible absorption and scanning electron microscopy. The effect of varying the central moiety on the photovoltaic performance is examined, and demonstrates that the monovalent and divalent phthalocyanines tend to yield higher efficiencies in blended structures, whereas the trivalent and tetravalent phthalocyanines tend to yield higher efficiencies in a bilayer structure. The apparent reason for the disparity is the measured decrease in the hole transport efficiency in trivalent and tetravalent phthalocyanine upon blending with C<sub>60</sub>. Furthermore, the open circuit voltages of M-Phthalocyanine/Fullerene solar cells are grouped together according to the valency of the central moiety.

### 4.3.1 Experimental Details

In this study, the effect of varying the central moiety in M-Phthalocyanine/fullerene (M-Pc/C<sub>60</sub>) solar cells was examined. All M-Pc molecules had the basic structure shown in Figure 1.10. We examined here the case of monovalent (metal-free H<sub>2</sub>), divalent (Cu, Mg, Zn), trivalent (In-Cl, Al-Cl, Ga-Cl), and tetravalent (Ti=O, V=O) phthalocyanine as the donor, with C<sub>60</sub> as the acceptor. Specifically, we investigated the effect on the power conversion efficiency (PCE) of blending C<sub>60</sub> with each M-Pc by examining full spectrum current density-voltage (J-V) characterization, UV-visible absorption, photoconductive time-of-flight, and scanning electron microscopy.

All M-Pc were purified by 3-zone train sublimation, whereas the C<sub>60</sub> was acquired by MER Corp (99.5%+ purity) and used without further modification. Buffer layer materials (bathocuproine (BCP), MoO<sub>3</sub>) were purchased from Sigma Aldrich and used without further purification. All devices were fabricated on patterned indium tin oxide (ITO) ( $\sim 15 \Omega/\square$ ) coated aluminosilicate glass, 50 mm x 50 mm substrates. The substrates were then cleaned sequentially in soap solution, DI water, methanol, isopropanol, and UV-ozone. After cleaning, substrates were loaded into a multi-boat, multi-mask thermal evaporator. A cryo-pump was then used to draw a vacuum of  $< 4 \times 10^{-4}$  Pa before any layer was deposited, and the pressure was monitored to ensure that it did not rise beyond  $5 \times 10^{-4}$  Pa during evaporation. Thicknesses were controlled using quartz crystal monitors. For each M-Pc, two device structures were examined: Bilayer and Blend. These structures are shown in Figure 4.1. Blended devices were co-evaporated in a 1:1 ratio and sources were independently monitored to ensure an accurate ratio. For each M-Pc examined, the blend and bilayer devices were fabricated in parallel on the same substrate, ensuring that they had common MoO<sub>3</sub>, BCP, and Al deposition conditions. Devices were sequentially layered at high vacuum and no layer was exposed to air until after the device was completed.

Completed devices were connected to external measurement circuitry using pressure contacts and illuminated through the ITO electrode with 100 mW/cm<sup>2</sup> simulated sunlight using an Oriel 96000 simulator with AM1.5G spectral filter. Simulated solar power was monitored using a Newport 818-UV detector coupled to a Newport

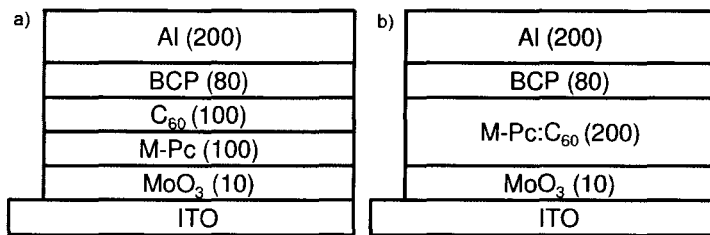


Figure 4.1: a) Bilayer and b) Blend device structures, with thicknesses in  $\text{\AA}$

1830-C optical power meter, and output current-voltage curves were acquired with a Keithley 238 source-measure unit and PC. The active area was  $7 \text{ mm}^2$ , as defined by shadow mask. It should be noted that each M-Pc-C<sub>60</sub> solar cell was not optimized for maximum efficiency since each would likely require different thicknesses, deposition rates, and deposition temperatures. By standardizing the structure and thickness, the photon absorption can be controlled and the bilayer and blend structures can be compared against each other in 2 critical areas: exciton separation efficiency and charge transport efficiency.

### 4.3.2 Absorption Spectra

The absorption spectra for one M-Pc of each valency (H<sub>2</sub>Pc, ZnPc, ClInPc, VOPc) is shown in Figure 4.2. These spectra were measured for M-Pc/C<sub>60</sub> bilayer films with equal thicknesses of M-Pc and C<sub>60</sub>, and do not change when the films were blended (1:1) M-Pc:C<sub>60</sub>. As expected, below 550nm, all four M-Pc films have the same absorption spectra due to absorption from the C<sub>60</sub>. For the monovalent H<sub>2</sub>Pc and divalent ZnPc, a peak at 630 nm with a shoulder at 700 nm is present. These are consistent with the absorption spectra of amorphous films of M-Pc. For the trivalent ClInPc and tetravalent VOPc, the absorption spectra reveals a more redshifted profile, with a peak near 750 nm. This is consistent with M-Pc that deposits in a more crystalline nature. The relative amorphous vs. crystalline nature of the M-Pc's is further investigated by analyzing the effects of blending C<sub>60</sub> with M-Pc on the J-V response (Section 4.3.3), as well as direct measurement via time-of-flight photoconductivity

(Section 4.3.4).

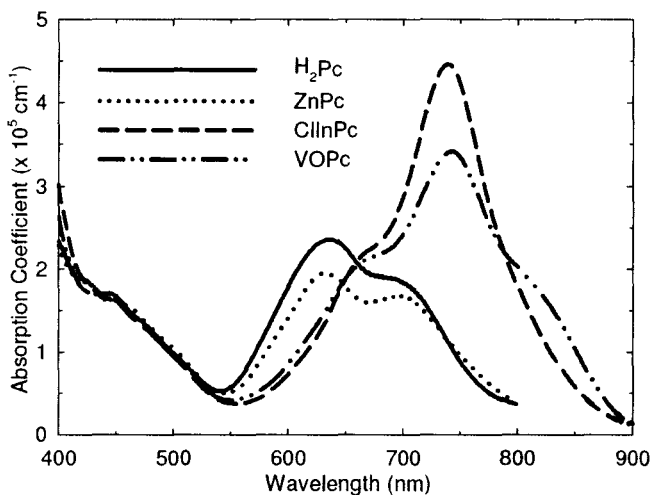


Figure 4.2: Absorption spectra for bilayer M-Pc/C<sub>60</sub> films

### 4.3.3 Current-Voltage

The J-V characteristics in Figure 4.3 show a fairly clear trend in terms of open circuit voltage, with monovalent H<sub>2</sub>Pc/C<sub>60</sub>  $V_{oc} \approx$  divalent (Cu, Mg, Zn) M-Pc/C<sub>60</sub>  $V_{oc} <$  tetravalent (Ti=O, V=O) M-Pc/C<sub>60</sub>  $V_{oc} <$  trivalent (In-Cl, Al-Cl, Ga-Cl) Pc/C<sub>60</sub>  $V_{oc}$ . Further, in both the bilayer and blend structures, there is little variation in the  $V_{oc}$  within each valency group, indicating that the  $V_{oc}$  is more strongly correlated to the valency of the central atom and the attached axial atom rather than the size of the metal atom itself. This is related to the lowering of the HOMO level of M-Pc by more strongly electron accepting moiety, resulting in a bigger difference in HOMO(Pc)-LUMO(C<sub>60</sub>) energy levels, and hence a higher  $V_{oc}$  [47]. Other groups have reported similarly high  $V_{oc}$  for a trivalent [120] and a tetravalent [121] Pc.

In the case of the bilayer structure, there is a low donor-acceptor interfacial area, and hence the exciton separation efficiency can be limited. Therefore, in order to achieve a reasonable efficiency, the bilayer devices must have good charge transport properties. This is often a function of the molecular order of the film, since mobility

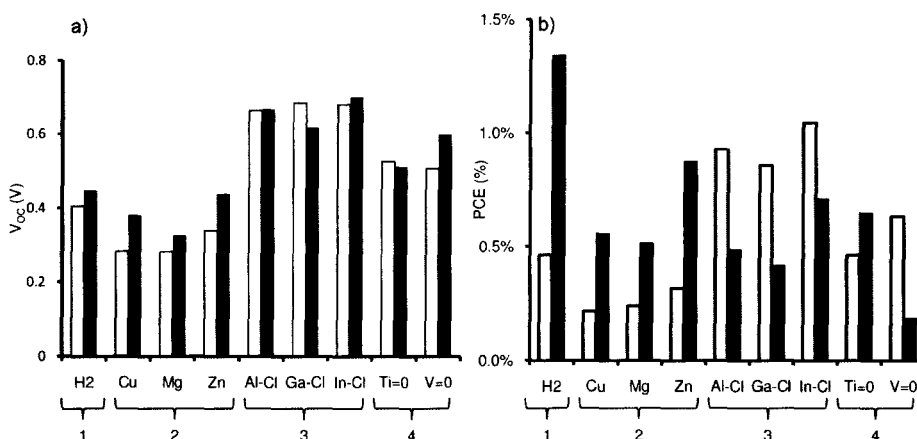


Figure 4.3: a) Open circuit voltage ( $V_{oc}$ ) and b) power conversion efficiency (PCE) for M-Pc/ $C_{60}$  bilayer (open) and blended M-Pc: $C_{60}$  (filled) solar cells.

in organic semiconductors is tied to molecular crystallinity [37]. Here, trivalent and tetravalent Pc's exhibit the highest short circuit currents, as well as dark currents that are  $\sim 2$  orders of magnitude lower than divalent and monovalent Pc's. These factors are most emphasized when comparing trivalent and divalent Pc's, whereby trivalent Pc's exhibit power conversion efficiencies that are roughly 3x higher than divalent Pc's ( $\sim 1\%$  vs.  $\sim 0.3\%$ ) in the bilayer structure.

In the case of the blend structure, the average distance that a photogenerated exciton must travel is much shorter than in the bilayer case due to the greater interfacial area, resulting in more efficient exciton dissociation. This often results in higher short circuit current density, but can also have the negative effect of lowering the fill factor. In this case, divalent Pc generates a higher short circuit current than trivalent Pc but is still surpassed by monovalent  $H_2Pc$ . This is a surprising result, as  $H_2Pc$  is no longer preferred in xerographic applications due to the higher photosensitivity of other metal-phthalocyanines [122].

Figure 4.3 demonstrates a fairly clear trend for the metal free and divalent phthalocyanines. By blending the M-Pc with  $C_{60}$ , a notable increase in power conversion efficiency occurs. Conversely, with the exception of TiOPc, trivalent and tetravalent Pc decrease in power conversion efficiency when blended. Currently, we are unaware as to why TiOPc does not follow the trend, though it is possible that as-deposited

TiOPc forms in the amorphous Phase I and does not crystallize without exposure to solvent treatment [123].

It is important to note that monovalent and divalent Pc's are mostly planar molecules. On the other hand, trivalent and tetravalent Pc have a Cl or O atom normal to the phthalocyanine plane, allowing for a greater number of stacking configurations. It seems from the J-V results (Figure 4.4) that the monovalent and divalent Pc have similar transport properties regardless of being in a configuration that favors crystallinity (bilayer) or in a configuration whereby the order is highly disrupted by equal parts of C<sub>60</sub> being co-evaporated (blend). This implies that blending with C<sub>60</sub> should not affect the charge collection efficiency, but should increase the charge separation efficiency due to much higher interfacial donor-acceptor area. Indeed, Figure 4.4a and 4.4b show that blending of C<sub>60</sub> with H<sub>2</sub>Pc or ZnPc results in a downward shift in the J-V response without loss of  $V_{oc}$  or FF. This implies that H<sub>2</sub>Pc and ZnPc can act like a small molecule point-conductor, where charge transport can be described by the classical Bässler formalism [8]. Other studies on divalent metal phthalocyanine solar cells have similarly shown a strong correlation between transport properties and solar cell performance [14]. Conversely, transport properties for the trivalent and tetravalent Pc seem to be adversely affected by blending with C<sub>60</sub>. In this case, while blending with C<sub>60</sub> would increase the exciton separation efficiency through higher donor-acceptor interfacial area, the charge collection efficiency could be concomitantly decreased through a disruption of the molecular crystal that would otherwise be formed by evaporating a pristine layer of trivalent or tetravalent M-Pc. Figure 4.4c and 4.4d show that upon blending with C<sub>60</sub>, ClInPc and VOPc demonstrate a lowering of power conversion efficiency mostly through a reduction in fill factor, which is an indication that the transport properties have been the most affected. Since the blending of C<sub>60</sub> with M-Pc should increase the exciton separation efficiency, and the light absorption is held constant by controlling the amount of M-Pc deposited, it is reasonable to conclude that the blending of C<sub>60</sub> with ClInPc and VOPc have an adverse affect on the carrier transport properties.

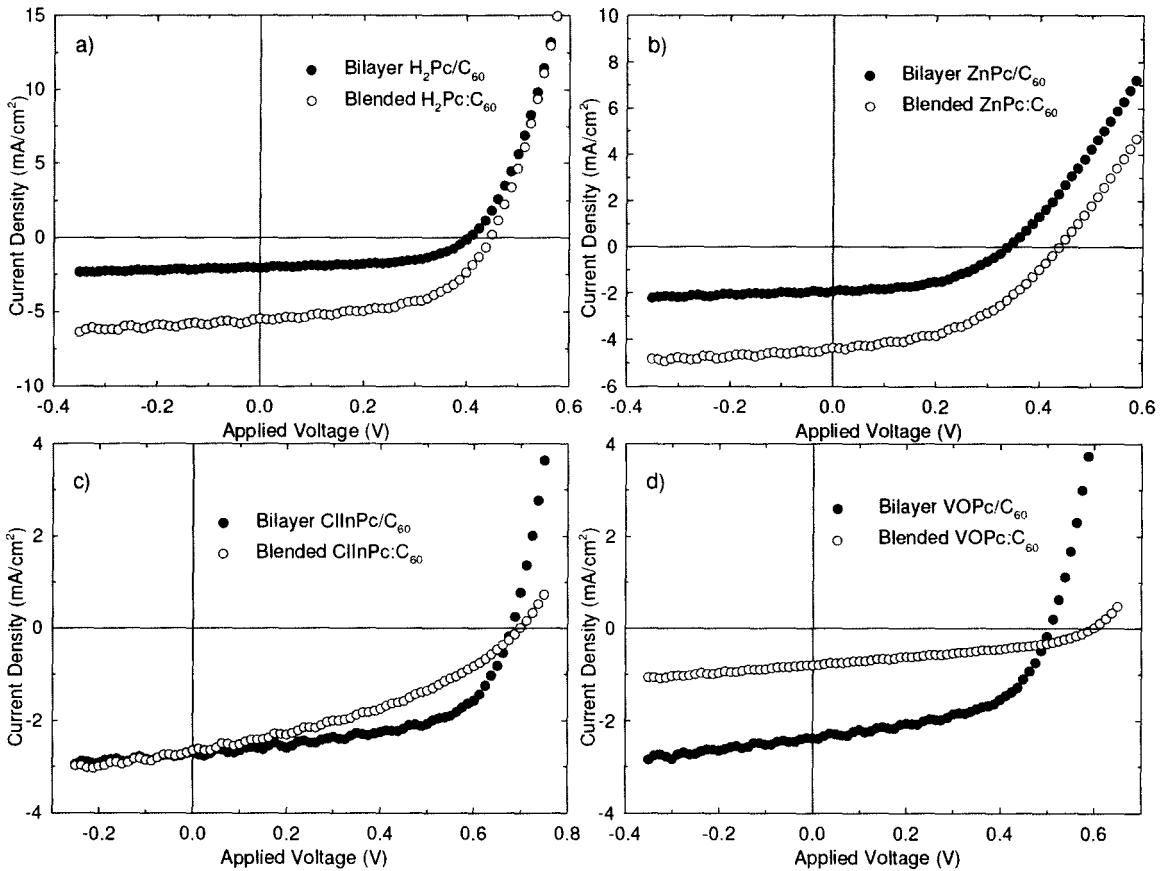


Figure 4.4: J-V response for bilayer and blended devices of a) H<sub>2</sub>Pc, b) ZnPc, c) ClInPc and d) VOPc

#### 4.3.4 Lateral Time-of-Flight

In order to directly examine the effects of blending M-Pc with C<sub>60</sub> on the charge transport properties, the hole mobility of the films were studied by measuring Lateral Time-of-Flight photoconductivity (LTOF) [91, 92]. LTOF measurements were performed by the method described in Section 2.4.4. LTOF was chosen over the more traditional (vertical) TOF since hole mobility ranges and equipment resolution requirements necessitated film thicknesses in the order of 10's of  $\mu\text{m}$ . At a deposition rate of 0.1 nm/s, fabrication of these devices would be prohibitively time consuming. Therefore, for this LTOF study, parallel aluminum contacts were deposited 40  $\mu\text{m}$  apart to act as the flight distance, and the pulse of light was provided by a N<sub>2</sub> dye

laser (Spectra Physics, 650nm peak, 10ns pulse) focused through an optical microscope next to one of the electrodes. The applied electric field was set to  $\sim 10^5$  V/cm. Deposited pristine M-Pc or M-Pc:C<sub>60</sub> blended films had a thickness of 50 nm in order to capture enough light to increase the signal to noise ratio. It is important to note that the thickness in this case does not affect the transit time, since the flight distance is defined by the separation of the two aluminum electrodes. LTOF samples were prepared and measured for both the bilayer and blend structure of 4 different M-Pc's: H<sub>2</sub>Pc, ZnPc, ClInPc, and VOPc.

Results of the LTOF study seem to agree well with an interpretation of the J-V results. In the case of H<sub>2</sub>Pc and ZnPc, there is no notable decrease in the hole mobility upon blending with C<sub>60</sub>. In fact, H<sub>2</sub>Pc shows an increase in hole mobility, from  $8 \times 10^{-4}$  cm<sup>2</sup>V<sup>-1</sup>s<sup>-1</sup> to  $7 \times 10^{-3}$  cm<sup>2</sup>V<sup>-1</sup>s<sup>-1</sup>. This agrees with the downward shift in J-V response from Figure 4.4a, whereby the blend structure produces a higher short circuit current without a notable decrease in fill factor. For ClInPc and VOPc LTOF, results show a 4x and 2x decrease in hole mobility, respectively. For ClInPc, hole mobility drops from  $4 \times 10^{-3}$  cm<sup>2</sup>V<sup>-1</sup>s<sup>-1</sup> to  $1 \times 10^{-3}$  cm<sup>2</sup>V<sup>-1</sup>s<sup>-1</sup> upon blending with C<sub>60</sub>. For VOPc, hole mobility drops from  $1 \times 10^{-3}$  cm<sup>2</sup>V<sup>-1</sup>s<sup>-1</sup> to  $5 \times 10^{-4}$  cm<sup>2</sup>V<sup>-1</sup>s<sup>-1</sup> upon blending with C<sub>60</sub>. These LTOF results again agree with the J-V results, whereby the fill factor for blended devices is notably lower for trivalent and tetravalent Pc. Of particular note is the lowering of the slope of the J-V curve (Figure 4.4c) at the open circuit voltage upon blending with C<sub>60</sub>, implying a higher series resistance and lower carrier mobility.

### 4.3.5 SEM Imaging

Figure 4.5 and 4.6 show the effect of blending C<sub>60</sub> with ClInPc. SEM images were acquired using a JEOL-7000F in secondary electron mode. The SEM image of a pristine ClInPc film in Figure 4.5 shows nanoclusters in the order of  $\sim 10$ 's of nm, which is also the thickness of the film in the active device. Examining Figure 4.6, it is clear that blending ClInPc with C<sub>60</sub> results in a more amorphous film, with the small nanoclusters no longer appearing. SEM images of pristine ZnPc also demonstrate

a similarly amorphous nature (image not shown). The amorphous nature of ZnPc implies that the hole mobility should not decrease when blended with  $C_{60}$  since there is no molecular crystal to disrupt. Indeed, LTOF results for ZnPc shows a negligible change in transport properties, with a hole mobility of  $6 \times 10^{-3} \text{ cm}^2 \text{V}^{-1} \text{s}^{-1}$  in pristine ZnPc and a hole mobility of  $5 \times 10^{-3} \text{ cm}^2 \text{V}^{-1} \text{s}^{-1}$  in blended ZnPc: $C_{60}$  films.

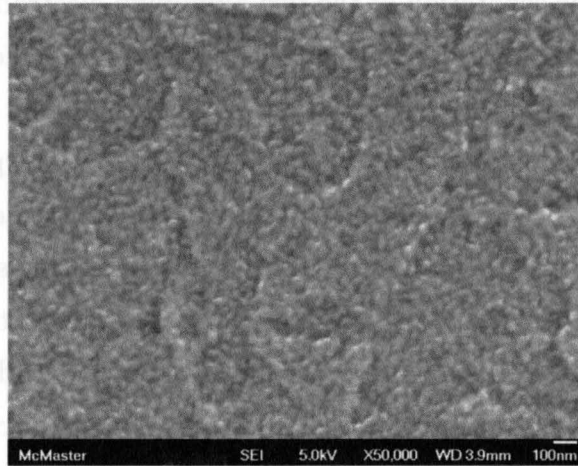


Figure 4.5: SEM image of a pristine ClInPc thin film

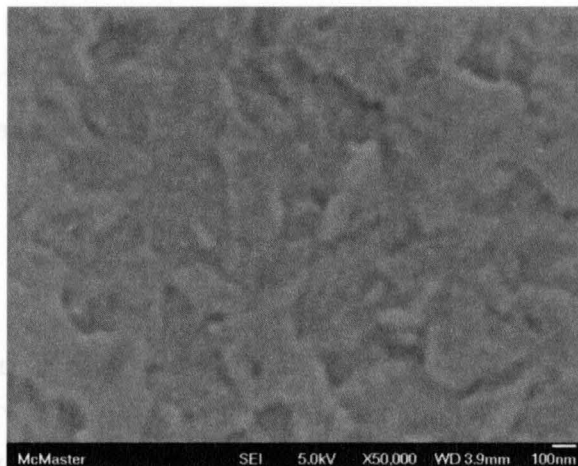


Figure 4.6: SEM image of a 1:1 blended ClInPc: $C_{60}$  thin film

### 4.3.6 Summary

In summary, M-Pc/C<sub>60</sub> photovoltaic devices were fabricated in bilayer and blended structures. It was determined that the open circuit voltage for M-Pc/C<sub>60</sub> solar cells can be grouped according to the valency of the central moiety, with trivalent chlorinated metals yielding the highest voltage. It was also determined that upon co-evaporating C<sub>60</sub> with planar monovalent (H<sub>2</sub>) or divalent metal (Cu, Zn, Mg) phthalocyanine, photovoltaic performance greatly increases due to an increase in donor-acceptor interfacial area resulting in an increased exciton separation efficiency, without a significant decrease in hole mobility. Conversely, trivalent metal (ClInPc, ClAlPc, ClGaPc) and one tetravalent metal (VOPc) show a decrease in efficiency upon co-evaporation with C<sub>60</sub> due primarily to the lowering of hole mobility.

## 4.4 Rubrene as an additive in M-Pc:C<sub>60</sub> Cells

This section describes an article (document D in preface), “Rubrene as an additive in M-Phthalocyanine/Fullerene Organic Solar Cells”, A.P. Yuen, N.M. Bamsey, A.M. Hor, J.S. Preston, R.A. Klenkler, S.M. Jovanovic, R.O. Loutfy, submitted to Solar Energy Materials & Solar Cells. The primary focus of this section is to examine factor (1) photovoltage to improve the overall power conversion efficiency of M-Pc/C<sub>60</sub> cells. Since photovoltage is primarily a function of material properties, this section describes how the integration of a new material can modify the  $V_{oc}$  of an organic solar cell.

Photovoltaic devices made from Metallo-Phthalocyanine/Fullerene (M-Pc/C<sub>60</sub>) with 5,6,11,12-Tetraphenylnaphthacene (rubrene) as an additive are fabricated and characterized. The effect of rubrene is examined for four different M-Phthalocyanines - H<sub>2</sub>Pc, ZnPc, ClInPc, and VOPc - to represent four different valencies of the central moiety of M-Pc. In each case, rubrene shows a notable increase in the open circuit voltage and in the case of the ClInPc and VOPc results in an increase in the overall power conversion efficiency. Through measurement of external quantum efficiency, it is shown that the increased efficiency is due to increased  $V_{oc}$  and *not* due to the photocurrent contribution from the complementary absorption profile of

rubrene. Finally, the photostability of rubrene-based cells is studied, showing that unencapsulated devices decay rapidly in air as a result of the formation of rubrene peroxide, as evidenced by significant decay of the UV-visible absorption and direct measurement of the cell performance over a time period as short as several minutes.

For vacuum coated devices, although there has been work on additional dopants to increase the spectral coverage of M-Pc/C<sub>60</sub> [124], there has been less focus on increasing the open circuit voltage ( $V_{oc}$ ) and fill factor (FF) [125]. Although these materials have yielded excellent  $J_{sc}$  values, the  $V_{oc}$  has still been limited to  $\sim 0.6V$  for the most commonly studied material systems. It is clear that in order to increase the PCE of devices, further efforts must be made to increase the  $V_{oc}$  as well. Some groups have shown an increase in open circuit voltage with the use of 5,6,11,12-tetraphenylanthracene (rubrene, Figure 4.7) as a dopant in divalent metal phthalocyanine (ZnPc, CuPc) [124,126] or in a system without M-Pc, where rubrene replaces the M-Pc as the electron donor [127,128]. Under ideal growth conditions, rubrene can exhibit excellent hole mobility in the order of  $1 \text{ cm}^2\text{V}^{-1}\text{s}^{-1}$  [129]. Rubrene has also been shown to improve the photogeneration efficiency in metal free H<sub>2</sub>Pc Schottky barrier cells [130].

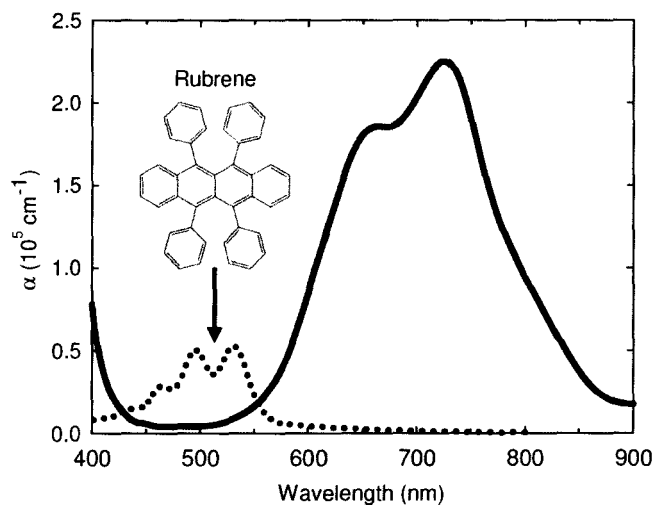


Figure 4.7: Molecular structure (inset) and absorption coefficient of rubrene (dotted line) and ClInPc (solid line)

The reported advantage of rubrene is its complementary absorption profile [124], which is highest in the region where many M-Pc's have no absorption (Figure 4.7). When these two materials are measured independently and normalized to their respective maxima, the incorporation of both materials may appear to be an effective way to increase spectral coverage. However, when thickness is taken into account and the absorption coefficients of the two materials are compared, it is clear that for equivalent thicknesses, the rubrene absorbs significantly less strongly than M-Pc. This implies that for a film of rubrene and a film of M-Pc of the same thickness, the total number of absorbed photons will be much higher in the M-Pc. Therefore, contrary to reported literature, the main advantage of rubrene cannot be an increase in light absorption. We assert that the main advantage of rubrene as an additive in an M-Pc/C<sub>60</sub> system is actually the voltage increase, and this is demonstrated in our experiments.

#### 4.4.1 Experimental Details

This experiment reports on the role of rubrene in monovalent (H<sub>2</sub>Pc), divalent (ZnPc), trivalent (ClInPc) and tetravalent (VOPc) phthalocyanine based solar cells and compare them with already reported rubrene/divalent M-Pc solar cells. Characterization includes full spectrum current density-voltage (J-V) characterization, external quantum efficiency (EQE), and UV-visible absorption spectroscopy. We also study the suitability of rubrene as a photovoltaic material by examining its stability in the presence of UV light and oxygen.

Photovoltaic cells were prepared as 4 different device structures, shown in Figure 4.8. Devices were fabricated on patterned indium tin oxide (ITO) ( $\sim 15 \Omega/\square$ ) coated aluminosilicate glass, 50 mm x 50 mm substrates. The substrates were then cleaned sequentially in detergent solution, DI water, methanol, isopropanol, and UV-ozone. After cleaning, substrates were loaded into a multi-boat, multi-mask thermal evaporator. A cryo-pump was then used to draw a vacuum of  $< 4 \times 10^{-4}$  Pa before any layer was deposited, and the pressure was monitored to ensure that it did not rise beyond  $5 \times 10^{-4}$  Pa during evaporation. All devices had an electron donor layer consisting of

10 nm of M-Pc, an electron acceptor layer consisting of 30 nm of  $C_{60}$ , and a cathode consisting of a 5 nm bathocuproine (BCP) buffer layer and 50 nm aluminum cathode. This basic structure is henceforth labeled structure a (Figure 4.8a). For the layered rubrene device (structure b, Figure 4.8b), a 10nm rubrene layer is inserted in between the M-Pc and  $C_{60}$  layer. For the blended device (structure c, Figure 4.8c), a 10 nm layer of 1:1 co-evaporated M-Pc: $C_{60}$  was inserted. Finally, for the rubrene blended structure (structure d, Figure 4.8d), a 10 nm layer of 1:1 co-evaporated M-Pc:rubrene and a 10nm layer of 1:1 co-evaporated rubrene:  $C_{60}$  were inserted. Thicknesses were controlled using quartz crystal monitors. All layers were deposited at  $\sim 0.08$  nm/s, and were sequentially layered at high vacuum and no layer was exposed to air until after the device was completed. All M-Pc and  $C_{60}$  were purified by 3-zone train sublimation. Sublimed grade BCP and rubrene were purchased from Sigma Aldrich and used without further purification.

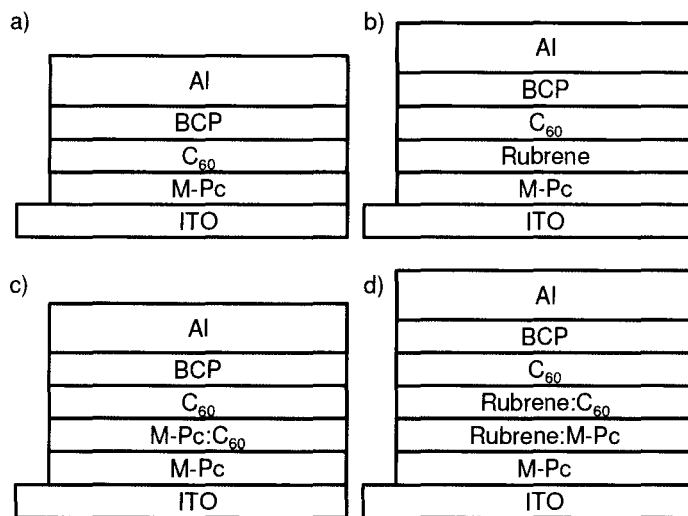


Figure 4.8: Device diagrams for structure: a) M-Pc/ $C_{60}$  b) M-Pc/ $CC_{60}$  with added discrete rubrene layer, c) M-Pc/ $C_{60}$  blend, and d) M-Pc/ $C_{60}$ /rubrene blend

Completed devices were connected to external measurement circuitry using pressure contacts and illuminated through the ITO electrode with  $100 \text{ mW/cm}^2$  simulated sunlight using an Oriel 96000 simulator with AM1.5G spectral filter. Samples were placed in a flowing Argon environment inside a sample chamber while tested. Sim-

ulated solar power was monitored using a Newport 818-UV detector coupled to a Newport 1830-C optical power meter, and output current-voltage curves were acquired with a Keithley 238 source-measure unit and PC. The active area was 7 mm<sup>2</sup>, as defined by shadow mask.

To acquire external quantum efficiency measurements, a calibrated monochromator (Photon Technology International) and a Picoammeter (Keithley 6485) were used to measure the short circuit current as a function of incident light wavelength. In order to calculate the external quantum efficiency, these values were then normalized to the incident power at each wavelength. UV/visible absorption was measured using a Cary Varian 5000 spectrophotometer.

#### 4.4.2 Current-Voltage

Table 4.1 lists the key measured parameters for each device. Of particular interest is the increase in the PCE of ClInPc and VOPc based devices when rubrene is blended with the M-Pc (structure d vs. structure c). In addition to the increase in the  $V_{oc}$  for these M-Pc's, the fill factor rises significantly, mostly due to a higher shunt resistance. It is possible that the quality of the diode is improved due to the wider HOMO-LUMO gap of rubrene as compared to the C<sub>60</sub>. Further, in our previous work (Section 4.3), we have shown that ClInPc and VOPc have reduced hole mobilities when blended with C<sub>60</sub>, as evidenced by a drop in the fill factor of the devices and direct TOF measurements. It is possible that when blending these M-Pc's with rubrene, the morphology of the film changes to be more favorable towards efficient charge transport. However, this has not been immediately verified. Some groups have also postulated that the blending of rubrene with M-Pc increases FF due to the high performance hole conducting nature of rubrene [126]. This is of particular benefit to ClInPc and VOPc, since the blending of C<sub>60</sub> with ClInPc or VOPc causes a reduction in FF (structure a vs. structure c). Blending these M-Pc's with rubrene (structure d) is therefore an effective way to recover the FF while concomitantly increasing the  $V_{oc}$ .

Some devices with the insertion of rubrene show a decrease in overall PCE due

		M-Pc, C <sub>60</sub> only (struct. a,c)				M-Pc, C <sub>60</sub> , rubrene (struct. b,d)					
	M-Pc		J <sub>sc</sub> mA/cm <sup>2</sup>	V <sub>oc</sub> V	FF %	PCE %		J <sub>sc</sub> mA/cm <sup>2</sup>	V <sub>oc</sub> V	FF %	PCE %
Layered	H <sub>2</sub> Pc	a	3.91	0.38	55	0.83	b	2.38	0.64	43	0.66
	ZnPc		4.23	0.35	51	0.77		2.43	0.66	43	0.68
	ClInPc		3.69	0.74	58	1.59		2.83	0.89	65	1.64
	VOPc		3.54	0.53	59	1.11		2.65	0.87	57	1.30
Blended	H <sub>2</sub> Pc	c	6.31	0.46	54	1.58	d	3.17	0.59	47	0.88
	ZnPc		6.64	0.40	55	1.46		3.66	0.67	42	1.02
	ClInPc		3.34	0.80	39	1.05		3.08	0.88	57	1.56
	VOPc		2.08	0.56	47	0.55		2.98	0.75	57	1.28

Table 4.1: J-V parameters for device structures a, b, c, and d (Figure 4.8).

to a significant reduction in short circuit current. However, every device with an inserted rubrene layer demonstrated a consistent increase in the open circuit voltage. This is likely due to the HOMO of rubrene lying lower than the HOMO of M-Pc, which results in a larger HOMO(donor)-LUMO(acceptor) difference and therefore a higher  $V_{oc}$  [47] (see Figure 4.9 for the energy level diagram of a ClInPc/rubrene/C<sub>60</sub> device). For ClInPc, which has the highest  $V_{oc}$  of the group, with the inclusion of rubrene the voltage is increased to a very high value of 0.89 V. It is also interesting to note that across all four M-Pc's, the same  $V_{oc}$  trend appears in both the pristine and rubrene-added cases, i.e.  $V_{oc}(\text{H}_2\text{Pc}/\text{C}_{60}) \approx V_{oc}(\text{ZnPc}/\text{C}_{60}) < V_{oc}(\text{VOPc}/\text{C}_{60}) < V_{oc}(\text{ClInPc}/\text{C}_{60})$ . This implies that rubrene is a simple additive for increasing the  $V_{oc}$  of any M-Pc. However, for M-Pc's that rely on high-current and low-voltage (H<sub>2</sub>Pc, ZnPc), the resultant increase in  $V_{oc}$  is not sufficient to offset the loss in current. For M-Pc's that rely on high  $V_{oc}$ , with relatively lower currents (ClInPc, VOPc), the increase in  $V_{oc}$  and FF is sufficient to increase PCE.

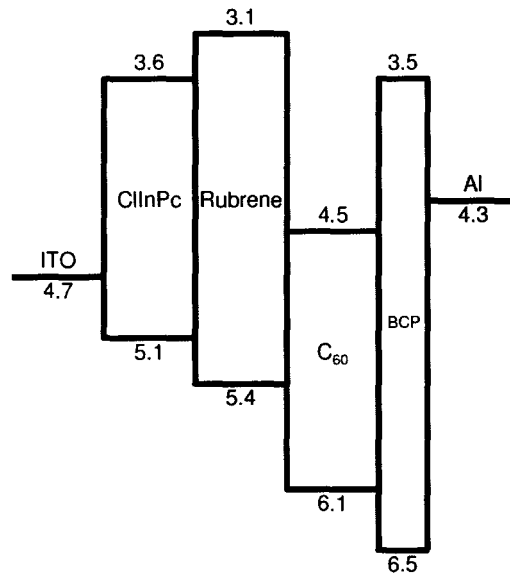


Figure 4.9: Energy level diagram for a layered ClInPc/rubrene/C<sub>60</sub> device

In order to determine the effect of a pristine layer of rubrene on a layered device, standard bilayer M-Pc/C<sub>60</sub> cells were fabricated with a 10 nm rubrene layer inserted in between (structure b). Results are shown in Table 4.1. For each M-Pc, the short circuit current density decreases. Given the complementary absorption profile of rubrene as compared to M-Pc, this is a surprising result since it would seem reasonable to assume that given the proper optimization of thickness, insertion of a rubrene layer could increase the short circuit current density due to increased absorption in the visible region of the solar spectrum. However, it is important to note that since the carrier mobility in disordered rubrene [131] is three orders of magnitude lower than for M-Pc, the layer of rubrene would have to be correspondingly thinner due to transport considerations. In addition to the much lower absorption coefficient of rubrene as compared to M-Pc, it would seem that relying on rubrene to act as a significant contributor to photocurrent is not a realistic assertion.

In order to demonstrate that the rubrene does not contribute a significant portion of the current, the EQE of three devices were measured (Figure 4.10a). In the standard bilayer ClInPc/C<sub>60</sub> device (structure a), the broad photocurrent contribution

between 600 and 800 nm can be seen. When the ClInPc is replaced by a 10 nm rubrene layer, making a rubrene/C<sub>60</sub> bilayer device, it is clear that there is very little additional current in the 450-550 nm region, where the rubrene absorbs the strongest. Therefore, we assert that the primary benefit of rubrene in this system is the voltage increase, not the current contribution as others have reported [124].

Interestingly, when a rubrene layer is inserted in between the ClInPc and C<sub>60</sub> layers, the EQE shows little to no contribution from the ClInPc and in fact matches the rubrene/C<sub>60</sub> device almost exactly. Indeed, due to the minimal current contribution from rubrene, the shape of the EQE curve is almost entirely aligned with the absorption profile of C<sub>60</sub> only and scales nearly linearly with the thickness of C<sub>60</sub> (Figure 4.10b), making C<sub>60</sub> the primary photon absorber. The proposed reasoning for this effect can be explained by an examination of the energy level diagram for the device, shown in Figure 4.9. In this particular system, the rubrene acts as a partial blocking layer since photogenerated electrons in the LUMO of ClInPc have a significant energy barrier to overcome to fall to the LUMO of C<sub>60</sub>, which would explain the lack of current contribution from light absorbed in the ClInPc. On the other hand, holes generated on the C<sub>60</sub> are not energetically restricted with the addition of rubrene, and hence the light absorbed by C<sub>60</sub> can contribute to the photocurrent. When the rubrene and ClInPc layers are reversed, the resulting efficiency decreases to  $\sim 0.50\%$ , since the wide band gap rubrene acts as a blocking layer for both holes and electrons. It is also important to note that in this system, the BCP buffer layer improves the electron transport from the C<sub>60</sub> to the Al [132]. This is because transport in the BCP layer occurs through states below the LUMO induced during deposition of the Al [133], and the BCP is sufficiently thin (5 nm) compared to the distance where current density has been shown to drop off [134].

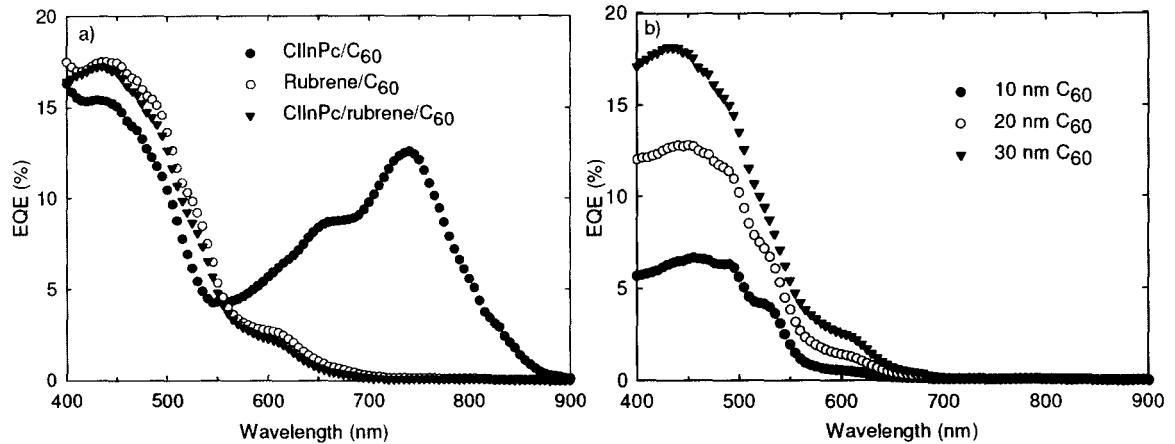


Figure 4.10: External Quantum Efficiency (EQE) of a) varying ClInPc/C<sub>60</sub>, Rubrene/C<sub>60</sub>, and ClInPc/Rubrene/C<sub>60</sub> structures and b) ClInPc/rubrene/C<sub>60</sub> layered devices with variable C<sub>60</sub> thickness

#### 4.4.3 Decay Study

Thus far, rubrene has shown to be an advantageous material for increasing the  $V_{oc}$  of M-Pc/C<sub>60</sub> solar cells. However, rubrene is highly susceptible to photo-oxidation, as shown in Figure 4.11b. When exposed to UV light (365 nm peak,  $\sim 15 \text{ mW/cm}^2$ ) while under a vacuum pressure of  $< 4 \times 10^{-4} \text{ Pa}$ , there is only a slight decrease in the absorptivity of the film. The slight decrease in absorption may be attributed to the brief time that the film is exposed to air and light after it is removed from high vacuum, as it is measured ex-situ. However, when a rubrene film is placed under high vacuum ( $\sim 4 \times 10^{-4} \text{ Pa}$ ) and the chamber is partially purged with dry O<sub>2</sub> and the sample exposed to the same UV source, the absorption drops significantly (Figure 4.11a).

In order to correlate the effect of the degradation of rubrene with the decrease in photovoltaic performance, devices were constantly illuminated by simulated AM1.5G solar spectrum light at  $100 \text{ mW/cm}^2$  and measured in 30 second intervals for  $\sim 1$  hour. Figure 4.11b shows the rapid decay of photocurrent when exposed to air. It has been shown that, in the presence of oxygen and light, rubrene peroxide will form [135]. This peroxide has a deeper HOMO level compared to rubrene as well as a shorter

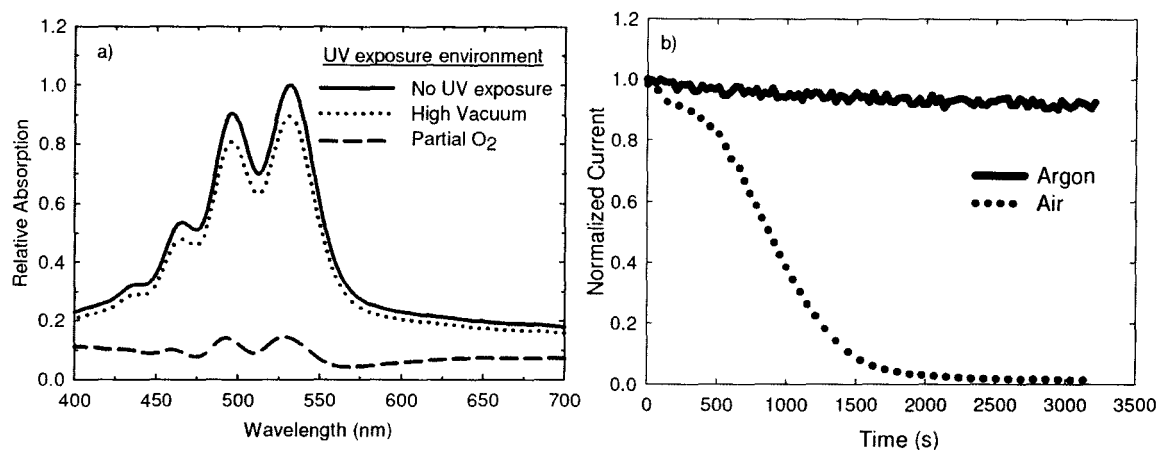


Figure 4.11: a) Relative absorption of rubrene when exposed to UV light in high vacuum and in O<sub>2</sub> environment and b) decay of photocurrent under exposure to air and Argon

conjugation length [136]. This has the effect of reducing hole transfer from the C<sub>60</sub>, decreasing photocurrent. Rubrene peroxide will also form intricate crystallites that cause severe local strain [137], possibly short circuiting the device. These results highlight the importance of removing oxygen while storing and testing devices incorporating rubrene. Preliminary results have shown that the power conversion efficiency of our devices will decay less than 5% if stored under Argon over the course of 24 hours in ambient light. Proper encapsulation to limit the diffusion of oxygen into the cell would therefore be a reasonable method of limiting the short-term decay of devices with rubrene.

#### 4.4.4 Summary

In summary, despite the complementary absorption profile of rubrene, the absolute quantity of absorbed photons is not sufficient to explain the increased power conversion efficiency. Rather, the primary benefit of rubrene in an M-Pc/C<sub>60</sub> system is the increase in open circuit voltage, across every M-Pc tested. For M-Pc's that rely on high-current, low voltage operation (H<sub>2</sub>Pc, ZnPc), the increase in open circuit voltage is not sufficient to offset the decrease in short circuit current. However, for M-

Pc's that rely on relatively lower current, higher voltage operation (ClInPc, VOPc), increased  $V_{oc}$  and FF result in an overall higher PCE. Furthermore, encapsulation of devices is shown to be of critical importance, as evidenced by the decay of UV/visible absorption and direct measurement of the decay of device performance when exposed to air.

## 4.5 Organic Parallel Tandem Cells

As previously discussed in Section 1.6.3, tandem structures are particularly useful because they can help overcome the relatively narrow absorption profiles of organic semiconductors. This is one method of improving factor (2) light absorption to increase the overall power conversion efficiency. The typical method of integrating multiple absorbing materials into a solar cell has been to stack them in a traditional series tandem configuration, whereby the voltages of the bottom and top junctions are added together. In this section, the general concept of the *parallel* tandem cell [75, 138, 139] is discussed. Sections 4.6 - 4.8 describe specific experiments utilizing the parallel tandem structure, with different materials or processing conditions differentiating them. The parallel tandem cell can be described as any combination of 3 (or more) active absorbing materials that increase the photocurrent without decreasing the photovoltage. Further, there is no requirement for a recombination layer or current matching. This makes the parallel tandem structure significantly easier to design and fabricate. Figure 4.12a shows a generic diagram of a parallel tandem organic solar cell used in this work. The first donor layer is deposited onto the ITO anode, and is then followed by either layered or blended donor/acceptor materials. The device can then be finished with an electron transport layer, buffer layer, or the cathode.

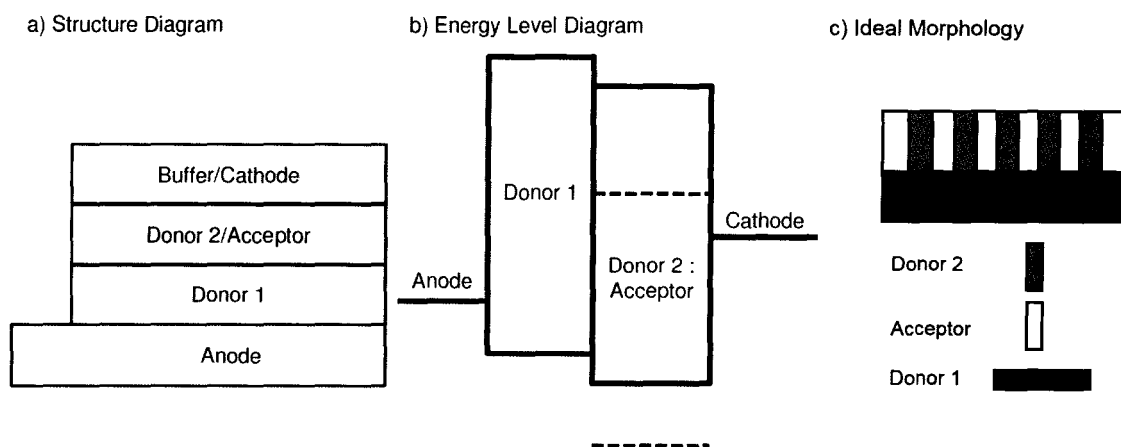


Figure 4.12: a) Generic structure of a parallel tandem cell, b) Energy level diagram for a parallel tandem cell, c) Ideal morphology of Donor and Acceptor layers

There are several design considerations for parallel tandem cells. First, the energy levels of the three materials must still be aligned to promote the proper direction for electron and hole transfer. That is, the general ‘staircase’ structure must still be employed, with the HOMO of the first layer (on the anode) lying the closest to vacuum and the LUMO of the top layer (by the cathode) being the furthest from vacuum (see Figure 4.12b). Second, in order to get any benefit from the introduction of multiple donor materials, the absorption profiles of donor 1, donor 2, and the acceptor must have minimal overlap. This results in complementary absorption profiles from each material that, when combined, effectively broadens the overall device absorption profile. Third, bicontinuous electron and hole transport must be possible. In the generic structure in Figure 4.12, electrons generated in the donor 1 layer can be transferred to the acceptor molecules in the donor 2/acceptor blend layer, while holes generated in the donor 2/acceptor blend layer can be transferred to the donor 1 layer. Finally, the mobility of the 3 materials must be similar to avoid highly unbalanced electron/hole transport, which would limit the photocurrent. Ideally, the morphology of the donor/acceptor layers should look like Figure 4.12c, where there is both high interfacial donor/acceptor area as well as bicontinuous hole and electron transport pathways.

## 4.6 Parallel Tandem Cells using M-Pc

The following section presents work that has been filed as a patent with the United States Patent and Trademark Office by Xerox Corp. (document E in preface, ‘Photovoltaic Device’, U.S. Ser. No. 12/910,056, filed Oct. 22, 2010), “A simple parallel tandem organic solar cell based on M-Phthalocyanines”, N.M. Bamsey, R.A. Klenkler, A.P. Yuen. In this work, I was the lead researcher. This section describes a method that improves efficiency by increasing factor (2) light absorption. This is important, because the relatively narrow absorption profile of organic materials compared to the AM1.5G solar spectrum significantly limits the power conversion efficiency.

A simple parallel tandem solar cell based on a combination of ZnPc and ClInPc has been fabricated and characterized. Compared to a traditional series tandem cell, parallel tandem cells eliminate the need for a semitransparent recombination layer, reducing the complexity of device fabrication while still providing an excellent increase in device performance. Results show a realized broadening of the spectral response and enhancement of the external quantum efficiency as a result of the complementary absorption profiles of ZnPc and ClInPc in the NIR region. Introduction of a blended ClInPc:C<sub>60</sub> layer is shown to more than double the power conversion efficiency (PCE) of a standard ZnPc/C<sub>60</sub> bilayer device (PCE=0.86%). The enhanced performance of the parallel tandem (PCE=1.81%) arises from an increase in both the open circuit voltage and the short circuit current. The experiment described here uses ZnPc and ClInPc as the two M-Pc electron donors, but there is the possibility for other combinations of divalent/trivalent M-Pc’s to be used as well.

### 4.6.1 Experimental Details

This experiment reports on the use of two different metallo-phthalocyanines with complementary absorption profiles in a parallel tandem cell, resulting in the broadening of the spectral response and a significant increase in power conversion efficiency (PCE). The first layer, ZnPc, absorbs photons in the 600-700 nm region [140]. The

second absorbing material, ClInPc, has a measured peak absorption extending from 600-800 nm. By combining these two M-Pc's, we can achieve a significant broadening of the absorption profile for this solar cell. This in turn leads to an increase in the short circuit current due to an improved overlap with the solar spectrum. Further, it has been shown that organic solar cells utilizing ZnPc or ClInPc as the electron donor, with fullerene as the electron acceptor, yield very different open circuits voltages ( $\sim 0.4V$  vs.  $\sim 0.7V$ ) [120]. This is a result of a lower HOMO of the ClInPc compared to ZnPc, resulting in a larger difference in the LUMO ( $C_{60}$ ) - HOMO (M-Pc) energy levels and therefore a higher  $V_{oc}$  [47]. Another advantage of using two M-Pc's is that they have similar hole mobilities, which helps alleviate carrier mobility balance concerns.

Photovoltaic devices were fabricated on patterned indium tin oxide (ITO) ( $\sim 15 \Omega/\square$ ) coated aluminosilicate glass, 50 mm x 50 mm substrates. The substrates were then cleaned sequentially in detergent solution, DI water, methanol, isopropanol, and UV-ozone. After cleaning, substrates were loaded into a multi-boat, multi-mask thermal evaporator. A cryo-pump was then used to draw a vacuum of  $< 4 \times 10^{-4}$  Pa before any layer was deposited, and the pressure was monitored to ensure that it did not rise beyond  $5 \times 10^{-4}$  Pa during evaporation. Three device structures were fabricated (thickness, in nm, in parenthesis):

- (1) ZnPc(10) /  $C_{60}$ (30)
- (2) ClInPc: $C_{60}$ (10) /  $C_{60}$ (30)
- (3) ZnPc(10) / ClInPc: $C_{60}$ (10) /  $C_{60}$ (30)

All devices were finished with a 5 nm bathocuproine (BCP) buffer layer (to improve electron transport from  $C_{60}$  to Al [132]) and a 50 nm aluminum cathode. Device (1) is a standard ZnPc/ $C_{60}$  bilayer device. Device (2) is a blended (1:1 ratio) ClInPc: $C_{60}$  device with a  $C_{60}$  n-transport layer. Device (3) is the simple parallel tandem device with a ClInPc: $C_{60}$  photon harvesting layer inserted into the bilayer. Thicknesses were controlled using quartz crystal monitors. All layers were deposited at  $\sim 0.08$  nm/s, and were sequentially layered at high vacuum and no layer was exposed to air until after the device was completed. All M-Pc and  $C_{60}$  were purified by

3-zone train sublimation. Sublimed grade BCP was purchased from Sigma Aldrich and used without further purification. Figure 4.13 is a structure diagram for the parallel tandem cell (structure (3)).

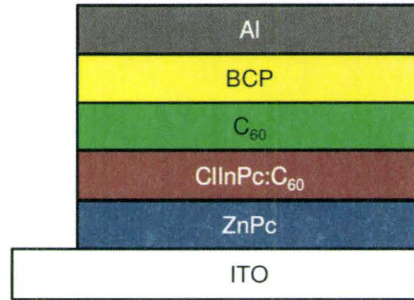


Figure 4.13: Structure diagram of a ZnPc/ClInPc:C<sub>60</sub> parallel tandem cell

Completed devices were connected to external measurement circuitry using pressure contacts and illuminated through the ITO electrode with  $100 \text{ mW/cm}^2$  simulated sunlight using an Oriel 96000 simulator with AM1.5G spectral filter. Samples were placed inside a chamber in a flowing Argon environment while tested. Simulated solar power was monitored using a Newport 818-UV detector coupled to a Newport 1830-C optical power meter, and output current-voltage curves were acquired with a Keithley 238 source-measure unit and PC. The active area was  $7 \text{ mm}^2$ , as defined by shadow mask.

To acquire external quantum efficiency (EQE) measurements, a calibrated monochromator (Photon Technology International) and a Picoammeter (Keithley 6485) were used to measure the short circuit current as a function of incident light wavelength. In order to calculate the external quantum efficiency, these values were then normalized to the incident power at each wavelength.

The energy level diagram for the simple parallel tandem (device 3) is shown in Figure 4.14. In this simple tandem, the current is produced in parallel by both M-Pc layers and therefore does not require the current matching conditions that series-tandems require. Holes generated in ZnPc can freely flow to the ITO contact, and electrons generated in ZnPc can be transferred to the C<sub>60</sub> network that exists in the

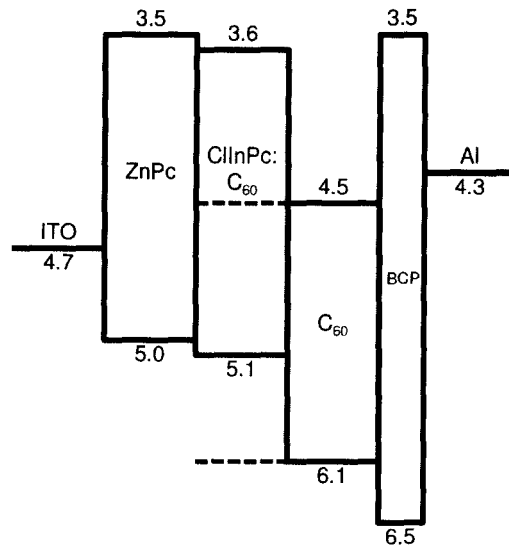


Figure 4.14: Energy level diagram for simple parallel tandem cell

blend. Similarly, holes generated in the ClInPc in the blend can be transferred to the ZnPc since its HOMO lies closer to vacuum than the ClInPc HOMO, and electrons in the ClInPc can be transferred to the C<sub>60</sub> network in the blend. The blended ClInPc:C<sub>60</sub> layer is preferable to discrete layers of ClInPc and C<sub>60</sub>, since the exciton separation efficiency is higher due to higher interfacial area.

#### 4.6.2 Current-Voltage

The current density-voltage (J-V) characteristics for the three devices are shown in Table 4.2 and Figure 4.15, with current densities J calculated by dividing the measured current by the active area. When comparing the ZnPc/C<sub>60</sub> bilayer (device 1) with the ClInPc:C<sub>60</sub> blend (device 2), the most prevalent difference is the open circuit voltage. Cells based on ClInPc exhibit very high open circuit voltages since they belong to the trivalent metallo-phthalocyanine group [120]. In contrast, divalent ZnPc has a slightly larger short circuit current density but a much lower open circuit voltage. This results in device (1) having a relatively low PCE of 0.86%. The blended ClInPc:C<sub>60</sub> (device 2) has a PCE of 1.34%, mostly due to the much higher photovoltage. It

is clear from Figure 4.15 that the insertion of a ClInPc:C<sub>60</sub> layer into the standard ZnPc/C<sub>60</sub> bilayer results in a significant increase of the short circuit current density, while increasing the photovoltage over the ZnPc/C<sub>60</sub> device. The  $V_{oc}$  of this tandem (device 3) lies between the  $V_{oc}$  of device 1 and device 2, possibly owing to the lowering of the HOMO of ZnPc due to the presence of ClInPc. In addition, while no attempts at optimization are reported here, the current from each layer adds to a sum that is close to the measured  $J_{sc}$  of device 3. In other words, device 3 suffers from little loss in current due to recombination arising from the introduction of the additional M-Pc layer. As a result of the favorable increase in current and the increase in voltage, with little change to the fill factor, the overall PCE of device 3 is 1.81%, more than double the efficiency of a ZnPc/C<sub>60</sub> layer without a blended ClInPc:C<sub>60</sub> layer. This PCE is only slightly lower than the combined PCE of device 1 and 2. This performance increase is similar to what could be achieved in a series-tandem structure, however is a much simpler design and is not hindered by current matching considerations.

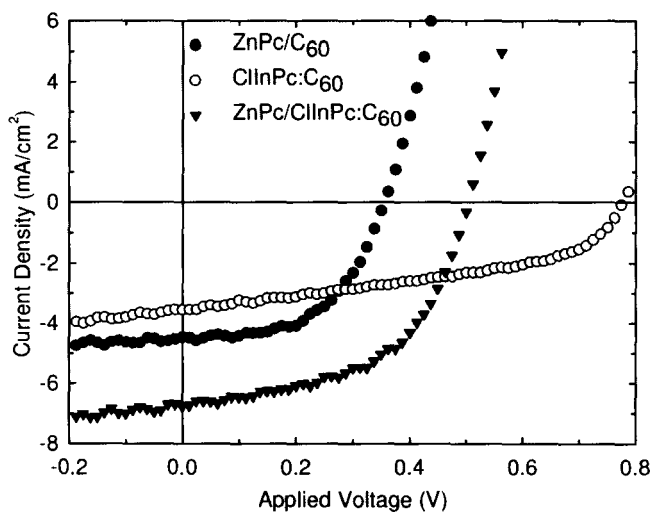


Figure 4.15: J-V Response for (1) ZnPc/C<sub>60</sub>, (2) ClInPc:C<sub>60</sub>/C<sub>60</sub>, and (3) ZnPc/ClInPc:C<sub>60</sub>/C<sub>60</sub> devices

Device	$J_{sc}$ (mA/cm <sup>2</sup> )	$V_{oc}$ (mV)	FF (%)	PCE (%)
(1)	4.47	360	54	0.86
(2)	3.95	790	43	1.34
(3)	6.75	500	53	1.81

Table 4.2: J-V parameters for (1) ZnPc/C<sub>60</sub>, (2) ClInPc:C<sub>60</sub>/C<sub>60</sub>, and (3) ZnPc/ClInPc:C<sub>60</sub>/C<sub>60</sub> devices

### 4.6.3 EQE & UV-vis

In order to investigate the relative current contribution from each layer, the external quantum efficiency of device 1 and 3 are shown in Figure 4.16. It is clear that the quantum efficiency of the ZnPc/C<sub>60</sub> cell follows very closely the shape of the ZnPc absorption profile, implying that the current contribution in this area of the solar spectrum arises from exciton generation in the ZnPc layer. Consequently, this ZnPc/C<sub>60</sub> cell has a decreasing current contribution starting at 700nm, as this coincides with the drop in photon absorption in ZnPc. Examining the EQE profile of the simple tandem shows not only the current contribution in the 600-700 nm region from the ZnPc, but also a very clear current contribution increase near 700nm. In fact, the addition of the ClInPc:C<sub>60</sub> layer results in a relative five-fold increase in EQE at 740 nm. This EQE peak follows the absorption profile of ClInPc, clearly showing that exciton generation in the ClInPc:C<sub>60</sub> layer is primarily responsible for the photocurrent at wavelengths above 700nm. Therefore, device 3 demonstrates a significant broadening of the spectral response and enhancement of external quantum efficiency as a result of exciton generation in both ZnPc and ClInPc.

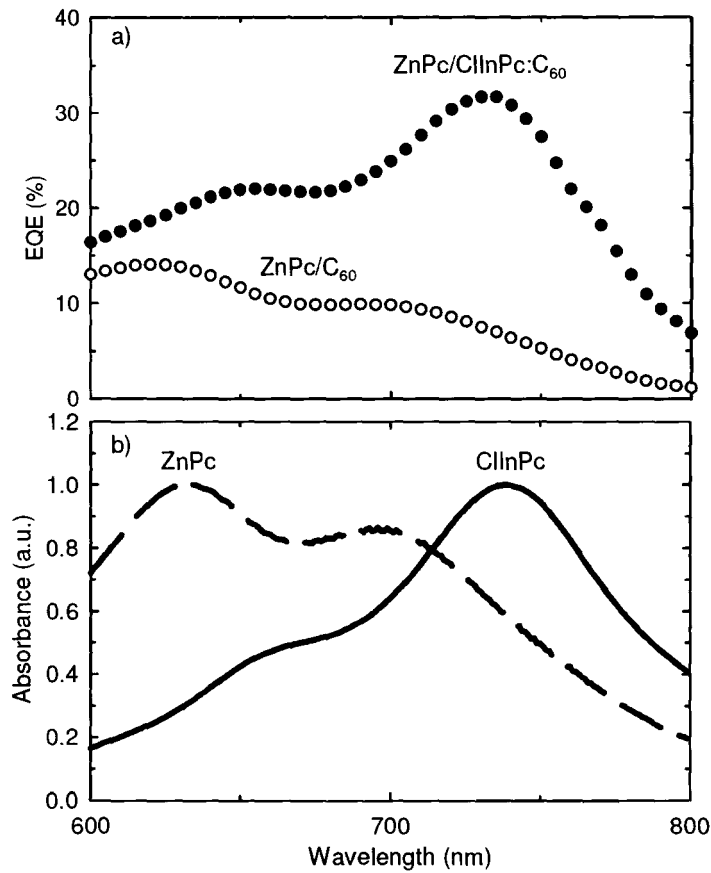


Figure 4.16: a) external quantum efficiency of ZnPc/C<sub>60</sub>(open circles) and ZnPc/ClInPc:C<sub>60</sub> (filled circles) devices and b) absorption spectra of ZnPc (dashed line) and ClInPc (solid line)

#### 4.6.4 Summary

In summary, a simple parallel tandem cell consisting of a combination of ZnPc and ClInPc as electron donors has been achieved. Results show an increase in the short circuit current as a result of the complementary absorption profiles of the two M-Pc's, and an open circuit voltage that resides between the voltages of a bilayer ZnPc/C<sub>60</sub> cell and a blended ClInPc/C<sub>60</sub> cell. The overall result is a more than doubling of the efficiency of a standard ZnPc/C<sub>60</sub> bilayer cell. This result is significant, and there is no inherent reason that this general structure cannot be applied to multiple classes of materials.

## 4.7 Solvent Treatment & Heteromorphic Tandems

The following section presents work that has been filed as a patent with the United States Patent and Trademark Office by Xerox Corp. (document F in preface, ‘Photovoltaic Device’, U.S. Ser. No. 12/910,005, filed Oct. 22, 2010), “Heteromorphic Chloroindium Phthalocyanine Films for Improved Photovoltaic Performance”, N.M. Bamsey, R.A. Klenkler, A.P. Yuen. In this work, I was the second researcher (behind N. Bamsey), and actively participated in the design and execution of the experiment, as well as the data analysis and interpretation. This section aims to increase efficiency by improving factor (2) light absorption.

It has been shown that the molecular packing of M-Pc can have a significant effect on the photoconductivity of M-Pc thin films [56, 57]. These different M-Pc packing arrangements are referred to as polymorphs, and it has been shown that a number of M-Pc’s can be converted from one polymorph to another by exposing deposited M-Pc thin films to solvent vapour [20, 141, 142]. Polymorphism is common in M-Pc’s because intermolecular forces between molecules are relatively weak, allowing for a variety of stacking orientations [56]. Depending on the solvent and central moiety, the swelling and relaxation of the film can result in more ordered and photosensitive films [141, 142]. This is of particular interest for the trivalent M-Pc’s, which when solvent treated can extend their absorption spectra beyond 850 nm. Solvent vapour treatment is therefore an excellent method of increasing current generation by absorbing a broader portion of the spectrum. In addition, as shown in Section 4.3, trivalent M-Pc/C<sub>60</sub> solar cells have the highest  $V_{oc}$  among the M-Pc’s. If the photocurrent could be increased without too much sacrifice in photovoltage, the overall photovoltaic performance could be significantly increased. Indeed, for tetravalent TiOPc thin films, solvent treatment has been shown to increase the photovoltaic performance [123, 143]. Previously, Tetrahydrofuran (THF) has been shown to be a very effective solvent for phase transformation of trivalent M-Pc’s [142].

### 4.7.1 Experimental Details

In this experiment, the effects of solvent exposure on the photovoltaic performance of trivalent ClInPc-based devices are examined. Using this knowledge, a novel structure is designed and demonstrates an increase in the overall power conversion efficiency by over 50 % compared to the untreated sample.

Samples were prepared on ITO coated aluminosilicate glass, 50 mm x 50 mm substrates. The cleaning procedure for these substrates is described in section 2.1.2, and the deposition of thermally evaporated thin films was performed using the equipment described in Section 2.3.2. Each device contained a total of 16 nm of evaporated ClInPc, followed by 30 nm of C<sub>60</sub>, 10 nm of BCP, and then capped with 50 nm of Al. Thicknesses were measured using quartz crystal monitors. Three device structures with varying ClInPc treatment conditions were examined:

- (1) as-deposited ClInPc without exposure to solvent
- (2) ClInPc film that was exposed to THF
- (3) ‘heteromorphic’ layer: 10 nm of solvent treated ClInPc + 6 nm of untreated ClInPc

Structure 2 and 3 were fabricated by first depositing a thin film of ClInPc, then removing from the vacuum chamber and exposing to THF vapour for several hours. The films were then loaded back into the vacuum chamber, and the rest of the device was completed under high vacuum. For structure 3, the 10 nm thickness was chosen to avoid the formation of isolated crystallites during THF exposure, as has been shown in very thin M-Pc layers [123]. The device structures are shown in Figure 4.17. The purpose of structure 3 is to determine if the EQE spectra of ClInPc/C<sub>60</sub> solar cells could be broadened by additional current contribution resulting from the integration of the two fairly complementary absorption profiles of THF-treated ClInPc and untreated ClInPc.

### 4.7.2 Current-Voltage

The J-V response for the three device structures are shown in Figure 4.18 and Table 4.3. The efficiencies of structure 1, 2 and 3 are 1.50%, 2.14%, and 2.35%,

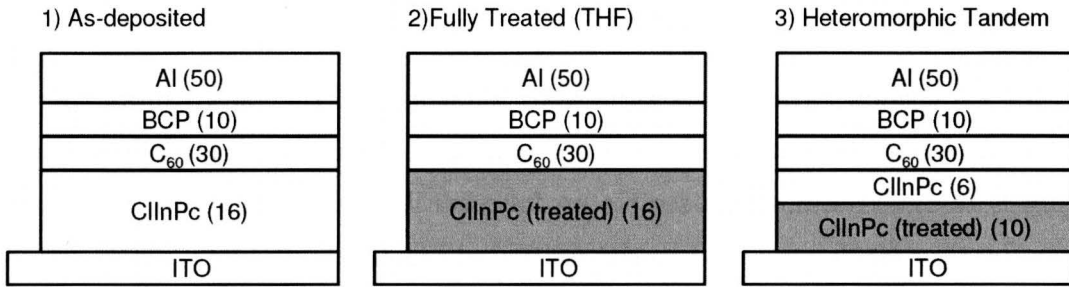


Figure 4.17: Three device structures of the evaporated ClInPc/C<sub>60</sub> solar cells

respectively. When comparing structure 1 and 2, it is very evident that the primary benefit of THF treatment is the increase in the short circuit current density (4.1 mA/cm<sup>2</sup> for structure 1, 6.2 mA/cm<sup>2</sup> for structure 2). We attribute the increase in the  $J_{sc}$  to two factors: a) the increase in the surface roughness of the film and b) the broadening of the absorption profile and redshift of the absorption edge. In studies involving the solvent treatment of TiOPc for use in solar cells, the effect of surface roughness was shown to increase the  $J_{sc}$  as a result of increased interfacial area (increasing exciton separation efficiency) [123]. With regards to the absorption profile broadening, this is directly measured on THF treated ClInPc films, and is shown in Figure 4.19. The redshift of the absorption edge also leads to a slight decrease in the  $V_{oc}$ , as expected. Structure 3 retains the surface roughness advantage of structure 1, since it also contains a solvent exposed layer, but also benefits from increased absorption in the 720 nm region due to the addition of the untreated ClInPc. Further, the  $V_{oc}$  of structure 3 is at an intermediary point between the  $V_{oc}$  of structure 1 and the  $V_{oc}$  of structure 2, as is expected in a parallel tandem cell. It is likely that, due to the very thin (6 nm) layer of untreated ClInPc, and the roughened film of THF treated ClInPc, that there are parallel junctions between the untreated ClInPc/C<sub>60</sub> and THF treated ClInPc/C<sub>60</sub>. This would result in the parallel tandem JV response measured.

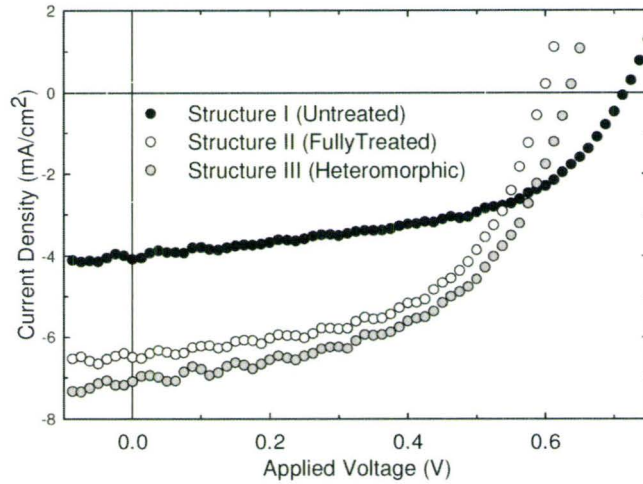


Figure 4.18: J-V response of different device structures incorporating ClInPc

Device	$J_{sc}$ (mA/cm <sup>2</sup> )	$V_{oc}$ (mV)	FF (%)	PCE (%)
(1)	4.1	715	51	1.50
(2)	6.5	597	56	2.14
(3)	7.1	634	52	2.35

Table 4.3: J-V parameters for solar cell based on a ClInPc layer that was (1) as-deposited (16 nm), (2) THF vapor treated (16 nm), and (3) heteromorphic THF vapor treated (10 nm)/as-deposited (6 nm)

### 4.7.3 EQE & Absorption

To verify that the photons absorbed by the THF treated films contribute to the photocurrent, the EQE spectra of all 3 structures was measured, and is shown in Figure 4.19. The results definitively show that there is a significant current contribution from absorbed photons in both untreated and THF treated ClInPc films. Structure 2 in particular shows a notably higher current generation in the 750-850 nm region, where the EQE is higher throughout. The dip in the absorption profile of THF treated ClInPc at 730 nm also manifests in the EQE spectra of structure 2,

showing that the action spectrum closely follows the absorption spectrum, i.e. the internal quantum efficiency is fairly uniform. Since the absorption spectrum of untreated ClInPc actually has a peak near 730 nm, the EQE of structure 3 contains 3 peaks: 2 peaks associated with THF treated ClInPc and 1 peak associated with untreated ClInPc. This additional current contribution in the 730 nm region, associated with the untreated ClInPc, is the reason for the slightly higher  $J_{sc}$  of structure 3. Since the current contribution from structure 3 follows the composite absorption spectrum of THF treated and untreated ClInPc, it is concluded that this structure allows both layers to contribute to the overall photocurrent without a notable loss from either layer. This is significant for several reasons. First, integrating a bilayer of polymorphs (rather than a bilayer of two different M-Pc's, such as those found in Section 4.6) reduces the number of raw materials required to fabricate the device. Secondly, because the two materials are chemically identical, there are no concerns regarding chemical reactions between layers. Finally, two different polymorphs of the same M-Pc will have quite similar energy levels and charge carrier mobilities, allowing for efficient charge transfer between layers. The charge transfer and charge transport in structure 3 are not significantly different from that of structure 2, as evidenced by their similar fill factors.

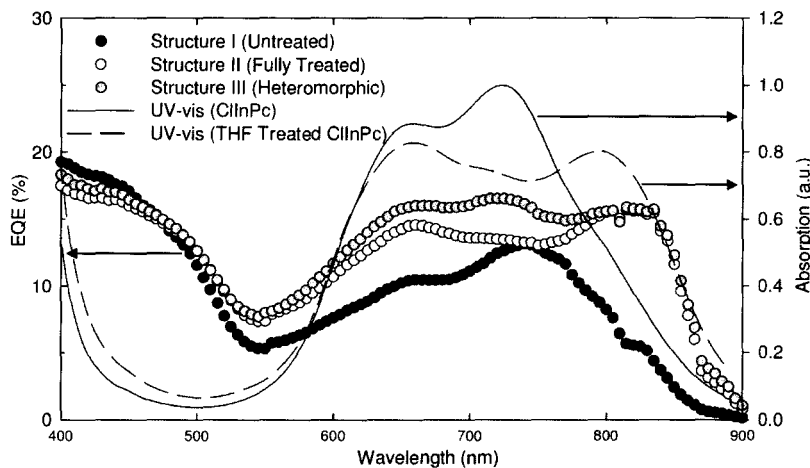


Figure 4.19: EQE of ClInPc/ $C_{60}$  device structures, with UV-vis indicating absorption profile of as-desposited ClInPc and THF treated films

#### 4.7.4 Summary

In summary, the results of this novel device structure are significant. Since many other M-Pc's are capable of solvent-induced polymorph transformations, this device structure could in principle be applied to a wide range of M-Pc's. This would allow for an extension of the absorption spectra of M-Pc's by using two polymorphs of the same material, without sacrificing significantly the photovoltage or charge transport properties. The experiment described here demonstrated a proof of concept for this so-called heteromorphic tandem cell, using ClInPc as the M-Pc and THF as the solvent. The PCE for this heteromorphic tandem cell was 10% greater than an all-THF-treated ClInPc layer, and was 55% greater than an untreated ClInPc layer. It is likely that thickness optimization, higher material purity, and higher vacuum could lead to increased power conversion efficiencies.

### 4.8 Combined Polymer & Small Molecule Tandems

The following section presents work that has been filed as a patent with the United States Patent and Trademark Office by Xerox Corp. (document G in preface, 'Photovoltaic Device', U.S. Ser. No. 12/910,028, filed Oct. 22, 2010), "Improved Spectral Coverage with the Integration of M-Phthalocyanines into PQT-12/PCBM Photovoltaic Cells", N.M. Bamsey, R.A. Klenkler, A.P. Yuen. In this work, I was the second researcher (behind N. Bamsey), and actively participated in the design and execution of the experiment, as well as the data analysis and interpretation. This section aims to increase efficiency by improving factor (2) light absorption. Further, it takes advantage of the polymorph conversion studied in Section 4.7 as well as the optimal casting conditions of PQT-12 from Section 3.4 to broaden the absorption profile of the cell.

Thus far, the photovoltaic device design improvements have been examined through one of two classes of devices, namely solution processed and vacuum coated OPV. This has been done with limited success in other labs in the world [139, 144–146]. In this section, the integration of both solution processed polymers and vacuum coated

small molecule materials is examined by leveraging knowledge gained in both Section 3.4 and 4.7. The implications of these results are important, since the polythiophene materials absorb in the green-red region of the spectrum, whereas the M-Pc's absorb in the near-IR. The ability to attain current contribution from both materials would be very beneficial towards increasing the  $J_{sc}$  of OPV devices.

### 4.8.1 Experimental Details

In this study, devices were fabricated by depositing a PQT-12/PCBM blended film on top of an evaporated M-Pc layer, forming a parallel tandem structure. Many different M-Pc's were tested, with some of them ( $H_2Pc$ ,  $CuPc$ ,  $ClInPc$ ,  $TiOPc$ ) demonstrating an overall increase in both current contribution and in overall power conversion efficiency. For cells with an underlayer of  $TiOPc$ , the increase in PCE is over 100% compared to the control sample.

The device structure for this experiment is shown in Figure 4.20. Samples were prepared on ITO coated aluminosilicate glass, 50 mm x 50 mm substrates. The cleaning procedure for these substrates is described in Section 2.1.2 and the techniques for solution processing and thermal evaporation are discussed in sections 2.2.1 and 2.3.2, respectively. A PEDOT:PSS layer was first deposited onto the cleaned substrate, and annealed at 120 °C for 20 minutes in a low oxygen (<0.2%), low humidity(<1%) glovebox. The sample was then loaded into the thermal evaporator, and a 16 nm layer of M-Pc (one of  $H_2Pc$ ,  $CuPc$ ,  $ClAlPc$ ,  $ClGaPc$ ,  $ClInPc$ ,  $VOPc$ ,  $TiOPc$ ) was deposited under high vacuum ( $5 \times 10^{-4}$  Pa). Quartz crystal monitors were used to determine thickness. The sample was then transferred back to the glove box, where a 20 mg/mL, 15 wt% PQT-12, 85 wt% PCBM solution dissolved in 1,2-dichlorobenzene was spun at 1000 rpm for 60 s, forming a layer approximately 50 nm thick. The Al cathode was then deposited at a pressure of  $2 \times 10^{-3}$  Pa by thermal evaporation. Including the control device, where no M-Pc is deposited, there was a total of 8 devices fabricated since there were 7 different M-Pc's tested.

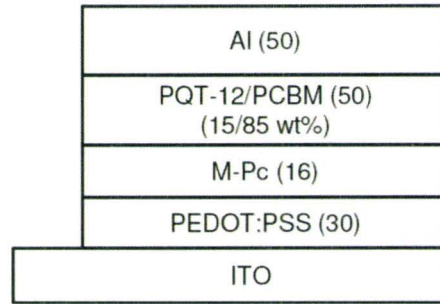


Figure 4.20: Device structure for PQT-12/M-Pc tandem cell, with thicknesses in nm

### 4.8.2 Current-Voltage

The J-V response for all 8 devices are shown in Figure 4.21 and summarized in Table 4.3. The first noticeable trend is the systematic increase in the  $V_{oc}$  for all devices with a M-Pc underlayer. This can be attributed to the lower HOMO level of M-Pc ( $\geq 5.1$  eV) compared to PEDOT ( $\sim 5.1$  eV), which increases the difference between the HOMO (donor) and LUMO (acceptor), thus increasing the  $V_{oc}$ . In addition, consistent with the results from Section 4.3, the highest  $V_{oc}$  is attained in the trivalent and tetravalent M-Pc's. When examining the  $J_{sc}$ , only CuPc, ClInPc, H<sub>2</sub>Pc and TiOPc show an increase in the current density compared to the control sample, with minimal decrease in the fill factor. However, for the three M-Pc's with reduced current and PCE (ClAlPc, ClGaPc, VOPc), the slope at the  $V_{oc}$  was lowered, indicating a higher  $R_s$ . Further, the reduced current for these M-Pc's is likely due to the layer thickness being greater than the carrier diffusion length. Since the charge transport properties depend on the central moiety of M-Pc and the M-Pc layer thickness was held constant in this study, devices are not necessarily optimized for each M-Pc.

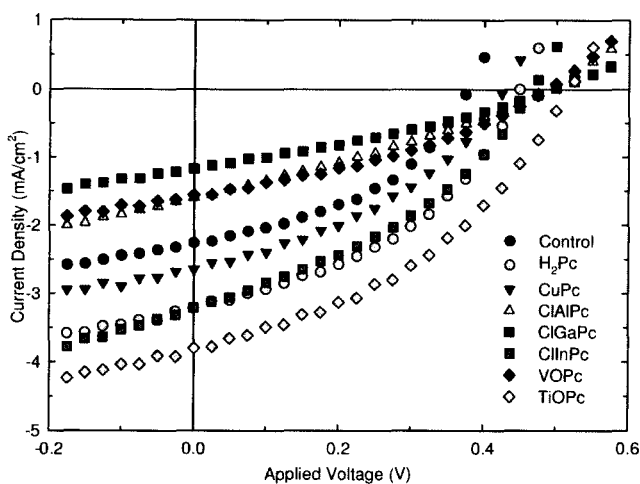


Figure 4.21: JV response for M-Pc/PQT-12 tandem devices

M-Pc	$V_{oc}$ (mV)	$J_{sc}$ (mA/cm <sup>2</sup> )	FF (%)	PCE (%)
none (control)	0.38	2.26	43	0.37%
H <sub>2</sub> Pc	0.45	3.22	42	0.61%
CuPc	0.43	2.65	39	0.44%
ClAlPc	0.49	1.60	30	0.24%
ClGaPc	0.50	1.17	31	0.30%
ClInPc	0.47	3.21	37	0.56%
VOPc	0.49	1.79	36	0.31%
TiOPc	0.52	3.80	40	0.79%

Table 4.4: J-V parameters for PQT-12/PCBM solar cells with M-Pc underlayers

### 4.8.3 TiOPc/PQT-12:PCBM tandems

The remainder of this study is focused on the examination of TiOPc as a material to integrate with PQT-12/PCBM to form a parallel tandem device structure. TiOPc

has been shown to have multiple polymorphs [147–149] and in particular, can be converted via solvent treatment [123, 150–153]. As shown in the absorption spectra in Figure 4.22, upon exposure to the 1,2-dichlorobenzene solvent upon spin coating, the TiOPc absorption peak redshifts from 730 nm to 750 nm and a noticeable broadening into the NIR wavelengths near 850 nm occurs. Since the PQT-12 and PCBM absorption is relatively low beyond 650 nm, the absorption in the 850 nm region is clearly not attributable to either PQT-12 or PCBM. To verify that the solvent was indeed causing this polymorphic shift, 1,2-dichlorobenzene (without any PQT-12 or PCBM) was spun on the TiOPc film. This yielded the same absorption spectra in the NIR region as that of the TiOPc/PQT-12:PCBM tandem. This is consistent with other groups' findings that showed that direct contact with solvent liquid induces polymorphic shifts in M-Pc [151, 152, 154]. It is actually quite fortuitous that the same solvent that dissolves the PQT-12 and PCBM also causes a favorable broadening of the absorption spectrum of the underlying TiOPc layer.

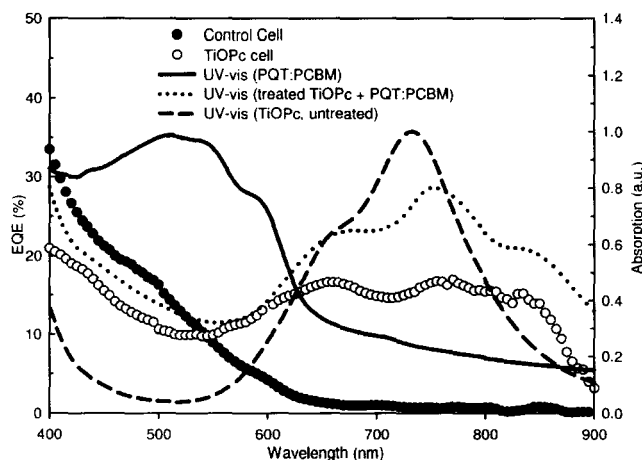


Figure 4.22: EQE & UV-vis for PQT-12/PCBM and TiOPc treated and untreated

In order to confirm that there is a current contribution from the TiOPc, the EQE of the completed device was measured, and is also shown in Figure 4.22. The EQE curves closely match the absorption profile for both the control device (no M-Pc) and for the TiOPc/PQT-12:PCBM parallel tandem device. For the control device, the

EQE drops off significantly to a negligible value beyond 650 nm, consistent with the absorption spectra of the PQT-12:PCBM blended film. When the TiOPc underlayer is present, the EQE spectra in the NIR region begins to follow the absorption profile of the converted TiOPc layer, leading to broad current contribution in the NIR (up to 900 nm) as well as the visible region. This additional current contribution explains the increase in the  $J_{sc}$  compared to the control. Further, this broad current contribution in the NIR region is sufficient to overcome the slight lowering of the current contribution from the PQT-12:PCBM region in the visible region that is likely the result of increased  $R_s$  due to the addition of the TiOPc layer. Overall, this results in an increase in power conversion efficiency from 0.37% to 0.79%, due in large part to the increase in  $J_{sc}$  from 2.26 mA/cm<sup>2</sup> to 3.80 mA/cm<sup>2</sup>.

#### 4.8.4 Summary

In summary, the integration of both solution processed and vacuum coated materials into a single device structure has been demonstrated. The addition of a TiOPc layer under the PQT-12/PCBM spun-on film results in a significant broadening of the EQE spectra as a result of current contribution from NIR wavelengths, thus increasing the overall  $J_{sc}$ . This results in the TiOPc/PQT-12:PCBM tandem having a PCE that is more than double the PCE of the cell with PQT-12:PCBM only. The increase in performance is greatly aided by the fact that the solvent that dissolves the PQT-12 and PCBM also causes a broadening of the absorption spectra of the TiOPc upon contact during spin coating.

# Chapter 5

## Conclusions & Future Work

### 5.1 Thesis Summary

Through a series of experiments aimed at improving one of the four factors (photovoltage, photon absorption, exciton separation, charge collection), materials were integrated into new device designs and their effects on improving power conversion efficiency were investigated. The four factors were primarily addressed as such:

1. Photovoltage: The integration of a third sensitizing material, rubrene, to the standard M-Pc/C<sub>60</sub> solar cells was shown to systematically increase the  $V_{oc}$  for every M-Pc tested. In the case of the trivalent (ClInPc) and tetravalent (VOPc) M-Pc's, the overall power conversion efficiency increased significantly as a result of increased voltage and fill factor. The high voltage of trivalent ClInPc was also demonstrated in section 4.3 establishing the general trend for the effect of the central moiety on the  $V_{oc}$ ,  $J_{sc}$ , and FF.
2. Light Absorption: Two new device structures were developed, namely the parallel tandem structure and the heteromorphic structure. The parallel tandem structure was demonstrated for both all-vacuum coated and for combined solution processed/vacuum coated structures. For the all-vacuum coated device, the insertion of a blended ClInPc:C<sub>60</sub> in between discrete layers of ZnPc and C<sub>60</sub> showed more than a two-fold increase in the power conversion efficiency due

primarily to extended absorption in the NIR wavelengths, leading to a higher  $J_{sc}$ . For the combined solution processed/vacuum coated structure, exposure of a TiOPc underlayer to 1,2-dichlorobenzene upon spin coating resulted in a polymorphic shift and increased absorption in the NIR wavelengths as well. The overall effect of this was a significant increase in  $J_{sc}$ . For the heteromorph structure, a solvent treated ClInPc layer was incorporated with an as-deposited ClInPc layer to take advantage of their relatively complementary absorption profiles, which lead to a broadening of the EQE in the NIR wavelengths and a concomitant increase in the  $J_{sc}$  and PCE.

3. Exciton Separation: The effect of blending of  $C_{60}$  with various M-Pc's is studied, and demonstrates the effect of increased interfacial area contributing to exciton separation. For some M-Pc's where the charge transport is not significantly affected by blending, there is a significant increase in the current generation, leading to a higher PCE.
4. Charge Collection: Two time-of-flight photoconductivity studies were performed. The first is on changing compositions of PQT-12 and PCBM to gain insight into the percolation threshold composition for this particular material system, and provided direct measurement of carrier mobility that corresponded well to the J-V responses measured. The second is on the four different valencies of M-Pc in pristine layers and in  $C_{60}$ -blended films. The results showed that for trivalent and tetravalent M-Pc, blending with  $C_{60}$  had a detrimental effect on the hole mobility, which corresponded to a measured decrease in the fill factor.

Finally, to help determine the suitability for commercialization of PQT-12 based devices, the stability of the PQT-12/PCBM solar cells was studied and found to be notably better than the standard P3HT solar cells.

In general, various design decisions have a notable effect on the power conversion efficiency, with individual design aspects affecting one or more of the four factors listed above. This work has shown that by addressing any of these four factors, the overall power conversion efficiency of an organic solar cell can be improved. This is

achieved through either an integration of a new material, or the employment of a different design structure. Consequently, complementary research groups around the world can contribute to the overall improvement of OPV devices by focusing either on the materials themselves (i.e. chemical structure, purity) or device design (device structure, fabrication techniques). This is particularly important since the skill set required for these two areas is often quite different, with new material synthesis performed by applied chemists and device design performed by engineers. The knowledge gained through this work is primarily beneficial to the latter, but also aids the former by helping establish desirable characteristics for new materials. Further collaboration between applied chemists and engineers therefore has a synergistic effect, whereby each group contributes their specialty towards furthering the performance of OPV devices. Ultimately, the knowledge contributed by this thesis through an examination of the four design factors will help to advance the state-of-the-art, primarily by contributing to the device design aspect. Further, it will hopefully aid in the development of this technology towards wide-spread commercialization for a plethora of applications.

## 5.2 Suggestions for Future Work

While the purpose of this thesis was to investigate the integration of new materials and new device designs to improve photovoltaic performance, more work is undoubtedly necessary before widespread commercialization of OPV technology is possible. Further, there are several suggestions for improvement of the future work done within our lab.

One particular element that we feel is necessary for achieving higher performance from fabricated devices in our lab is an increase in control of laboratory oxygen, humidity, and dust. Many of the best labs in the world utilize glove boxes that can reduce environmental oxygen and water vapour down to several ppm - 3 orders of magnitude lower than is possible in our lab. Further, fabrication of devices in a clean room would greatly reduce the dust content on devices, thus aiding in fabrication consistency. In addition, for vacuum coating of organic materials and cathodes, a

better vacuum would greatly improve the quality of evaporated layers.

Another aspect that we feel deserves further investigation is the ability to control the crystallization of PQT-12 when in the presence of PCBM. Given the increased stability and high hole mobility of PQT-12, if phase crystallization of PQT-12 can be controlled to include PCBM into the matrix, there is no particular reason why PQT-12 could not produce similar efficiencies as P3HT. It is possible that a combination of spin coating conditions and chemical surfactants or other additives could help bring about a more favorable PQT-12:PCBM morphology.

Finally, while the parallel tandem and heteromorphic structures demonstrated a proof-of-concept, further optimization could significantly increase the overall PCE. One particular suggested experiment is a combination of the knowledge gained from the heteromorphic tandem and the simple parallel tandem cells. Since solvent treatment redshifts the absorption edge of ClInPc, it may be possible to get an even wider photon absorption profile from the use of a ZnPc/ClInPc:C<sub>60</sub>(treated)/ClInPc:C<sub>60</sub>/C<sub>60</sub>/BCP/Al structure. This would result in 3 distinct absorption profiles from M-Pc (ZnPc, ClInPc, and treated ClInPc) in addition to the C<sub>60</sub> absorption. The device could be fabricated by first depositing the initial layers of the simple tandem device (ZnPc/ClInPc:C<sub>60</sub>), then removing from vacuum and solvent treating it with THF. The sample could then be placed back in the evaporator and finished with ClInPc:C<sub>60</sub>/C<sub>60</sub>/BCP/Al. It is possible that the ZnPc underlayer may also be polymorph converted by THF, so UV-vis absorption experiments may also be desirable to determine if this conversion has taken place.

We feel that the flexibility of the new structures described in this work allows for a considerable degree of refinements in terms of the materials used and the thicknesses and compositions of individual layers. Combined with higher purity materials, much higher PCE is very much a possibility.

# Bibliography

- [1] G. Li, V. Shrotriya, J. Huang, Y. Yao, T. Moriarty, K. Emery, and Y. Yang. High efficiency solution processable polymer photovoltaic cells by self-organization of polymer blends. *Nature Materials*, 4:864–868, 2005.
- [2] J. Xue, S. Uchida, B.P. Rand, and S.R. Forrest. Asymmetric tandem organic photovoltaic cells with hybrid planar-mixed molecular heterojunctions. *Applied Physics Letters*, 85:5757–5759, 2004.
- [3] W. Ma, C. Yang, X. Gong, K. Lee, and A.J. Heeger. Thermally stable, efficient polymer solar cells with nanoscale control of the interpenetrating network morphology. *Advanced Functional Materials*, 15:1617–1622, 2005.
- [4] J.Y. Kim, K. Lee, N.E. Coates, D. Moses, T.Q. Nguyen, M. Dante, and A.J. Heeger. Efficient tandem polymer solar cells fabricated by all-solution processing. *Science*, 317(5835):222–225, 2007.
- [5] T. Cheyney. Solarmer breaks organic solar PV cell conversion efficiency record, hits NREL-certified 7.9%, [http://www.pv-tech.org/news/\\_a/solarmer\\_breaks\\_organic\\_solar\\_pv\\_cell\\_conversion\\_efficiency\\_record\\_hits\\_nre/](http://www.pv-tech.org/news/_a/solarmer_breaks_organic_solar_pv_cell_conversion_efficiency_record_hits_nre/), December 2009.
- [6] Heliatek and IAPP achieve record efficiency levels for organic solar cells, <http://www.heliatek.com/news-13>, April 2010.
- [7] H-Y. Chen, J. Hou, S. Zhang, Y. Liang, G. Yang, Y. Yang, L. Yu, Y. Wu, and

- G. Li. Polymer solar cells with enhanced open-circuit voltage and efficiency. *Nature Photonics*, 3:649–653, 2009.
- [8] H. Bässler. Charge transport in disordered organic photoconductors: a monte carlo simulation study. *Physica Status Solidi B*, 175:15–56, 1993.
- [9] M. Esteghamatian, Z. D. Popovic, and G. Xu. Carrier generation process in poly(p-phenylene vinylene) by fluorescent quenching and delayed-collection-field techniques. *Journal of Physical Chemistry*, 100:13716–13719, 1996.
- [10] E. Frankevich, H. Ishii, Y. Hamanaka, T. Yokoyama, A. Fuji, S. Li, K. Yoshino, A. Nakamura, and K. Seki. Formation of polaron pairs and time-resolved photogeneration of free charge carriers in  $\pi$ -conjugated polymers. *Physical Review B*, 62(4):2505–2515, 2000.
- [11] E. Hendry, J.M. Schins, L.P. Candeias, L.D.A. Siebbeles, and M. Bonn. Efficiency of exciton and charge carrier photogeneration in a semiconducting polymer. *Physical Review Letters*, 92:196601, 2004.
- [12] V.I. Arkhipov and H. Bässler. Exciton dissociation and charge photogeneration in pristine and doped conjugated polymers. *Physica Status Solidi (a)*, 201(6):1152–1187, 2004.
- [13] V.D. Mihailetschi, H.X. Xie, B. de Boer, L.J.A Koster, and P.W.M. Blom. Charge transport and photocurrent generation in poly(3-hexylthiophene): Methanofullerene bulk-heterojunction solar cells. *Advanced functional Materials*, 16:699–708, 2006.
- [14] Y. Terao, H. Sasabe, and C. Adachi. Correlation of hole mobility, exciton diffusion length, and solar cell characteristics in phthalocyanine/fullerene organic solar cells. *Applied Physics Letters*, 90:103515, 2007.
- [15] M.C. Scharber, D. Mühlbacher, M. Koppe, P. Denk, C. Waldauf, A.J. Heeger, and C.J. Brabec. Design rules for donors in bulk-heterojunction solar cells -

- towards 10 % energy-conversion efficiency. *Advanced Materials*, 18:789–794, 2006.
- [16] A. Moliton and J.-M. Nunzi. How to model the behaviour of organic photovoltaic cells. *Polymer International*, 55:583–600, 2006.
- [17] C.W. Tang and A.C. Albrecht. Photovoltaic effects of metal-chlorophyll-a-metal sandwich cells. *The Journal of Chemical Physics*, 62:2139–2150, 1975.
- [18] A.K. Ghosh, D.L. Morel, T. Feng, R.F. Shaw, and Jr. C.A. Rowe. Photovoltaic and rectification properties of Al/Mg phthalocyanine/Ag Schottky-barrier cells. *Journal of Applied Physics*, 45(1):230–236, 1974.
- [19] F.-R Fan and L.R. Faulkner. Photovoltaic effects of metalfree and zinc phthalocyanines. II. Properties of illuminated thin-film cells. *The Journal of Chemical Physics*, 69(7):3341–3349, 1978.
- [20] A.M. Hor, R.O. Loutfy, and C.K. Hsiao. Photovoltaic properties of cadmium sulfide/trivalent metal phthalocyanine heterojunction devices. *Applied Physics Letters*, 42:165–168, 1983.
- [21] C.K. Chiang, M.A. Druy, S.C. Gau, A.J. Heeger, E.J. Louis, A.G. MacDiarmid, Y.W. Park, and H. Shirakawa. Synthesis of highly conducting films of derivatives of polyacetylene,  $(\text{CH})_x$ . *Journal of the American Chemical Society*, 100:1013–1015, 1978.
- [22] C.W. Tang. Two-layer organic photovoltaic cell. *Applied Physics Letters*, 48:183–185, 1986.
- [23] G. Yu, J. Gao, J.C. Hummelen, F. Wudl, and A.J. Heeger. Polymer photovoltaic cells: Enhanced efficiencies via a network of internal donor-acceptor heterojunctions. *Science*, 270:1789–1791, 1995.
- [24] J.J.M. Halls, C.A. Walsh, N.C. Greenham, E.A. Marseglia, R.H. Friend, S.C. Moratti, and A.B. Holmes. Efficient photodiodes from interpenetrating polymer networks. *Nature*, 376:498–500, 1995.

- [25] G. Dennler, M.C. Scharber, and C.J. Brabec. Polymer-fullerene bulk-heterojunction solar cells. *Advanced Materials*, 21:1323–1338, 2009.
- [26] W. Shockley and H.J. Queisser. Detailed balance limit of efficiency of p-n junction solar cells. *Journal of Applied Physics*, 32:510–519, 1961.
- [27] H. Yang, J. Burnett, and J. Ji. Simple approach to cooling load component calculation through pv walls. *Energy and Buildings*, 31:285–290, 2000.
- [28] Power Plastic Applications, [www.konarka.com/index.php/power-plastic/power-plastic-applications](http://www.konarka.com/index.php/power-plastic/power-plastic-applications).
- [29] F.C. Krebs, M. Biancardo, B. Winther-Jensen, H. Spanggaard, and J. Alstrup. Strategies for incorporation of polymer photovoltaics into garments and textiles. *Solar Energy Materials & Solar Cells*, 90:1058–1067, 2006.
- [30] B.G. Streetman and S. Banerjee. *Solid State Electronic Devices*. Prentice Hall, 2000.
- [31] J. Nelson. *The Physics of Solar Cells*. Imperial College Press, 2003.
- [32] F. Padinger, R.S. Rittberger, and N.S. Sariciftci. Effects of postproduction treatment on plastic solar cells. *Advanced Functional Materials*, 13:85–88, 2003.
- [33] P. Schilinsky, C. Waldauf, and C.J. Brabec. Recombination and loss analysis in polythiophene based bulk heterojunction photodetectors. *Applied Physics Letters*, 81:3885–3887, 2002.
- [34] H. Ishii, K. Sugiyama, E. Ito, and K. Seki. Energy level alignment and interfacial electronic structures at organic/metal and organic/organic interfaces. *Advanced Materials*, 11:605–625, 1999.
- [35] C.J. Brabec, V. Dyakonov, J. Parisi, and N.S. Sariciftci. *Organic Photovoltaics: Concepts and Realization*. Springer, 2003.
- [36] Adapted from H. Aziz, ECE730 lecture notes, University of Waterloo, 2007.

- [37] W. Brütting. *Physics of Organic Semiconductors*. Wiley-VCH, 2005.
- [38] Power Plastic 20 series, [www.konarka.com/media/pdf/konarka\\_20series.pdf](http://www.konarka.com/media/pdf/konarka_20series.pdf).
- [39] C. Dimitrakopoulos and D.J. Mascaro. Organic thin-film transistors: A review of recent advances. *IBM Journal of Research & Development*, 45:11–28, 2001.
- [40] E. Noether. Invariante variationsprobleme. *Nachrichten der Königlichen Gesellschaft der Wissenschaften zu Göttingen, Math-phys. Klasse*, pages 235–257, 1918.
- [41] B.A. Gregg and M.C. Hanna. Comparing organic to inorganic photovoltaic cells: Theory, experiment, and simulation. *Journal of Applied Physics*, 93:3605, 2003.
- [42] Z. Popovic and T. Bender. NIP20 tutorial T16, 2004.
- [43] C.J. Brabec, N.S. Sariciftci, and J.C. Hummelen. Plastic solar cells. *Advanced Functional Materials*, 11:15–26, 2001.
- [44] L. Smilowitz, N.S. Sariciftci, R. Wu, C. Gettinger, A.J. Heeger, and F. Wudl. Photoexcitation spectroscopy of conducting-polymer-C<sub>60</sub> composites: Photoinduced electron transfer. *Physical Review B*, 47:13835–13842, 1993.
- [45] N.S. Sariciftci, L. Smilowitz, A.J. Heeger, and F. Wudl. Photoinduced electron transfer from a conducting polymer to buckminsterfullerene. *Science*, 258:1474–1476, 1992.
- [46] S. Morita, A.A Zakhidov, and K. Yoshino. Doping effect of buckminsterfullerene in conducting polymer: Change of absorption spectrum and quenching of luminescence. *Solid State Communications*, 82:249–252, 1992.
- [47] C.J. Brabec, A. Cravino, D. Meissner, N.S. Sariciftci, T. Fromherz, M.T. Rispen, L. Sanchez, and J.C. Hummelen. Origin of the open circuit voltage in plastic solar cells. *Advanced Functional Materials*, 11:374–380, 2001.

- [48] C.R. McNeill, A. Abrusci, J. Zaumseil, R. Wilson, M.J. McKiernan, J.H. Burroughes, J.J.M. Halls, N.C. Greenham, and R.H. Friend. Dual electron donor/electron acceptor character of a conjugated polymer in efficient photovoltaic diodes. *Applied Physics Letters*, 90(19):193506, 2007.
- [49] I. McCulloch, M. Heeney, C. Bailey, K. Genevicius, I. MacDonald, M. Shkunov, D. Sparrowe, S. Tierney, R. Wagner, W. Zhang, M.L. Chabinyc, R.J. Kline, M.D. McGehee, and M.F. Toney. Liquid-crystalline semiconducting polymers with high charge-carrier mobility. *Nature Materials*, 5:328–333, 2006.
- [50] Y. Wu, P. Liu, B.S. Ong, T. Srikumar, N. Zhao, G. Botton, and S. Zhu. Controlled orientation of liquid-crystalline polythiophene semiconductors for high-performance organic thin-film transistors. *Applied Physics Letters*, 86:142102, 2005.
- [51] Y. Kim, S.A. Choulis, J. Nelson, D.D.C. Bradley, S. Cook, and J.R. Durrant. Device annealing effect in organic solar cells with blends of regioregular poly(3-hexylthiophene) and soluble fullerene. *Applied Physics Letters*, 86:063502, 2005.
- [52] C.J Brabec, S.E. Shaheen, T. Fromherz, F. Padinger, J.C. Hummelen, A. Dhannabalan, R.A.J Janssen, and N.S. Sariciftci. Organic photovoltaic devices produced from conjugated polymer/methanofullerene bulk heterojunctions. *Synthetic Metals*, 121:1517–1520, 2001.
- [53] S.E. Shaheen, C.J. Brabec, N.S. Sariciftci, F. Padinger, T. Fromherz, and J.C. Hummelen. 2.5% efficient organic plastic solar cells. *Applied Physics Letters*, 78:841–843, 2001.
- [54] H. Sirringhaus, T. Kawase, R.H. Friend, T. Shimoda, M. Inbasekaran, W. Wu, and E.P. Woo. High-resolution inkjet printing of all-polymer transistor circuits. *Science*, 290:2123–2126, 2000.
- [55] V.G. Shah and D.B. Wallace. Low-cost solar cell fabrication by drop-on-demand ink-jet printing. *Proceedings of IMAPS 37th Annual International Symposium on Microelectronics*, November 2004.

- [56] K.Y. Law. Organic photoconductive materials: recent trends and developments. *Chemical Reviews*, 93:449–486, 1993.
- [57] D.R. Tackley, G. Dent, and W.E. Smith. Phthalocyanines: structure and vibrations. *Physical Chemistry Chemical Physics*, 3:1419–1426, 2001.
- [58] S. Uchida, J. Xue, B.P. Rand, and S.R. Forrest. Organic small molecule solar cells with a homogeneously mixed copper phthalocyanine: C<sub>60</sub> active layer. *Applied Physics Letters*, 84:4218–4220, 2004.
- [59] J.S. Kim, R.H. Friend, and F. Cacialli. Surface energy and polarity of treated indium-tin-oxide anodes for polymer light-emitting diodes studied by contact-angle measurements. *Journal Of Applied Physics*, 86:2774–2778, 1999.
- [60] Z. Zhong, Y. Zhong, C. Liu, S. Yin, W. Zhang, and D. Shi. Study on the surface wetting properties of treated indium-tin-oxide anodes for polymer electroluminescent devices. *Physica Status Solidi*, 198:197–203, 2003.
- [61] L.S. Roman, W. Mammo, L.A.A Petersson, M.R. Anderson, and O. Inganäs. High quantum efficiency polythiophene/C<sub>60</sub> photodiodes. *Advanced Materials*, 10:774–777, 1998.
- [62] M.P. de Jong, L.J. van Ijzendoorn, and M.J.A. de Voigt. Stability of the interface between indium-tin-oxide and poly(3,4-ethylenedioxythiophene)/poly(styrenesulfonate) in polymer light-emitting diodes. *Applied Physics Letters*, 77:2255, 2000.
- [63] V. Shrotriya, G. Li, Y. Yao, C. Chu, and Y. Yang. Transition metal oxides as the buffer layer for polymer photovoltaic cells. *Applied Physics Letters*, 88:073508, 2006.
- [64] C.J. Brabec, S.E. Shaheen, C. Winder, and N.S. Sariciftci. Effect of LiF/metal electrodes on the performance of plastic solar cells. *Applied Physics Letters*, 80(7):1288–1290, 2002.

- [65] G.E. Jabbour, Y. Kawabe, S.E. Shaheen, J.F. Wang, M.M. Morrell, B. Kippelen, and N. Peyghambarian. Highly efficient and bright organic electroluminescent devices with an aluminum cathode. *Applied Physics Letters*, 88:1762–1764, 1997.
- [66] G. Li, V. Shrotriya, Y. Yao, and Y. Yang. Investigation of annealing effects and film thickness dependence of polymer solar cells based on poly(3-hexylthiophene). *Journal of Applied Physics*, 98:043704, 2005.
- [67] Mark Osborne. SunPower pushes c-si solar cell efficiency record to 24.2%, [http://www.pv-tech.org/news/\\_a/sunpower\\_pushes\\_c-si\\_solar\\_cell\\_efficiency\\_record\\_to\\_24.2/](http://www.pv-tech.org/news/_a/sunpower_pushes_c-si_solar_cell_efficiency_record_to_24.2/), June 2010.
- [68] J. Zhao, A. Wang, and M.A. Green. High-efficiency PERL and PERT silicon solar cells on FZ and MCZ substrates. *Solar Energy Materials & Solar Cells*, 65:429–435, 2001.
- [69] M.A. Green. The path to 25% silicon solar cell efficiency: History of silicon cell evolution. *Progress in Photovoltaics: Research and Applications*, 17:183–189, 2009.
- [70] S.E. Shaheen, D. Vangeneugden, R. Kiebooms, D. Vanderzande, T. Fromherz, F. Padinger, C.J. Brabec, and N.S. Sariciftci. Low band-gap polymeric photovoltaic devices. *Synthetic Metals*, 121:1583–1584, 2001.
- [71] M. Svensson, F. Zhang, S.C. Veenstra, W.J.H Verhees, J.C. Hummelen, J.M. Kroon, O. Inganäs, and M.R. Andersson. High-performance polymer solar cells of an alternating polyfluorene copolymer and a fullerene derivative. *Advanced Materials*, 15:988–991, 2003.
- [72] N. Blouin, A. Michaud, D. Gendron, S. Wakim, E. Blair, R. Neagu-Plesu, M. Belletête, G. Durocher, Y. Tao, and M. Leclerc. Toward a rational design of poly(2,7-carbazole) derivatives for solar cells. *Journal of the American Chemical Society*, 130:732–742, 2008.

- [73] Y. Liang, Y. Wu, D. Feng, S.T. Tsai, H.J. Son, G. Li, and L. Yu. Development of new semiconducting polymers for high performance solar cells. *Journal of the American Chemical Society*, 131:56–57, 2008.
- [74] J.K.J van Duren, A Dhanabalan, P.A. van Hal, and R.A.J. Janssen. Low-bandgap polymer photovoltaic cells. *Synthetic Metals*, 121:1587–1588, 2001.
- [75] C. Zhang, S.W. Tong, C. Jiang, E.T. Kang, D.S.H Chan, and C. Zhu. Simple tandem organic photovoltaic cells for improved energy conversion efficiency. *Applied Physics Letters*, 92:083310, 2008.
- [76] M.M. Wienk, J.M. Kroon, W.J.H Verhees, J. Knol, J.C. Hummelen, P.A. van Hal, and R.A.J. Janssen. Efficient methano[70]fullerene/MDMO-PPV bulk heterojunction photovoltaic cells. *Angewandte Chemie International Edition*, 42:3371–3375, 2003.
- [77] H. Neugebauer, M.A. Loi, C. Winder, N.S. Sariciftci, G. Cerullo, A. Gouloumis, P. Vázquez, and T. Torres. Photophysics and photovoltaic device properties of phthalocyanine/fullerene dyad:conjugated polymer mixtures. *Solar Energy Materials & Solar Cells*, 83:201–209, 2004.
- [78] I. Gur, N.A. Fromer, C.-P. Chen, A.G. Kanaras, and A.P. Alivisatos. Hybrid solar cells with prescribed nanoscale morphologies based on hyperbranched semiconductor nanocrystals. *Nano Letters*, 7(2):409–414, 2007.
- [79] W.U. Huynh, J.J. Dittmer, and A.P. Alivisatos. Hybrid Nanorod-Polymer Solar Cells. *Science*, 295(5564):2425–2427, 2002.
- [80] D.J. Milliron, I. Gur, and A.P. Alivisatos. Hybrid organic-nanocrystal solar cells. *MRS Bulletin*, 30:41–44, 2005.
- [81] S.A. McDonald, G. Konstantatos, S. Zhang, P.W. Cyr, E.J.D. Klem, L. Levina, and E.H. Sargent. Solution-processed PbS quantum dot infrared photodetectors and photovoltaics. *Nature Materials*, 4:138–142, 2005.

- [82] G. Dennler, H.J Prall, R. Koeppe, M. Egginger, R. Autengruber, and N.S. Sariciftci. Enhanced spectral coverage in tandem organic solar cells. *Applied Physics Letters*, 89:073502, 2006.
- [83] P. Peumans, A. Yakimov, and S.R. Forrest. Small molecular weight organic thin-film photodetectors and solar cells. *Journal of Applied Physics*, 93:3693–3723, 2003.
- [84] A.G.F Janssen, T. Reidl, S. Hamwi, H.-H. Johannes, and W. Kowalsky. Highly efficient organic tandem solar cells using an improved connecting architecture. *Applied Physics Letters*, 91:073519, 2007.
- [85] H. Kumar, P. Kumar, R. Bhardwaj, G.D. Sharma, S. Chand, S.C. Jain, and V. Kumar. Broad spectral sensitivity and improved efficiency in CuPc/Sub-Pc organic photovoltaic devices. *Journal of Physics D: Applied Physics*, 42:015103, 2009.
- [86] K. Sivula, Z.T. Ball, N. Watanabe, and J.M.J. Fréchet. Amphiphilic diblock copolymer compatibilizers and their effect on the morphology and performance of polythiophene:fullerene solar cells. *Advanced Materials*, 18:206–210, 2006.
- [87] C.M. Aguirre, S. Auvray, S. Pigeon, R. Izquierdo, P. Desjardins, and R. Martel. Carbon nanotube sheets as electrodes in organic light-emitting diodes. *Applied Physics Letters*, 88:183104, 2006.
- [88] A.R. Melnyk and D.M. Pai. *Physical Methods of Chemistry: Determination of Electronic and Optical Properties, Vol. 8, 2nd edition*. Wiley, New York, 1993.
- [89] R.A. Klenkler, G. Xu, J.F. Graham, and Z.D. Popovic. Charge transport across pressure-laminated thin films of molecularly doped polymers. *Applied Physics Letters*, 88:102101, 2006.
- [90] R. Pacios, J. Nelson, D.D.C. Bradley, and C.J. Brabec. Composition dependence of electron and hole transport in polyfluorene:(6,6)-phenyl C<sub>61</sub>-butyric acid methyl ester blend films. *Applied Physics Letters*, 83:4764, 2003.

- [91] M. Kitamura, T. Imada, S. Kako, and Y. Arakawa. Time-of-flight measurement of lateral carrier mobility in organic thin films. *Japanese Journal of Applied Physics*, 43:2326–2329, 2004.
- [92] A. Kuwahara, S. Naka, H. Okada, and H. Onnagawa. Carrier mobility of organic thin films using lateral electrode structure with optical slits. *Applied Physics Letters*, 89:132106, 2006.
- [93] B.S. Ong, Y. Wu, P. Liu, and S. Gardner. High-performance semiconducting polythiophenes for organic thin-film transistors. *Journal Of The American Chemical Society*, 126:3378–3379, 2004.
- [94] B.S. Ong, Y. Wu, P. Liu, and S. Gardner. Structurally ordered polythiophene nanoparticles for high-performance organic thin-film transistors. *Advanced Materials*, 17:1141–1144, 2005.
- [95] R.M. Hochstrasser and M. Kasha. Application of the exciton model to monomolecular lamellar systems. *Photochemistry and Photobiology*, 3:317–331, 1964.
- [96] P.M. Borsenberger and H. Bässler. The role of polar additives on charge transport in molecularly doped polymers. *Physica Status Solidi (b)*, 170:291–302, 1992.
- [97] D. Chirvase, J. Parisi, J.C. Hummelen, and V. Dyakonov. Influence of nanomorphology on the photovoltaic action of polymer/fullerene composites. *Nanotechnology*, 15:1317–1323, 2004.
- [98] S.M. Tuladhar, D. Poplavskyy, S.A. Choulis, and J.R. Durrant. Ambipolar charge transport in films of methanofullerene and poly(phenylenevinylene)/methanofullerene blend. *Advanced Functional Materials*, 15:1171–1182, 2005.
- [99] J.E. Parmer, A.C. Mayer, B.E. Hardin, S.R. Scully, M.D. McGehee, M. Heeney, and I. McCulloch. Organic bulk heterojunction solar cells using poly(2,5-

- bis(3-tetradecylthiophen-2-yl)thieno[3,2-b]thiophene). *Applied Physics Letters*, 92:113309, 2008.
- [100] Y. Kim, S. Cook, S.M. Tuladhar, S.A. Choulis, J. Nelson, J.R. Durrant, D.D.C. Bradley, M. Giles, I. McCulloch, C.-S. Ha, and M. Ree. A strong regioregularity effect in self-organizing conjugated polymer films and high-efficiency polythiophene:fullerene solar cells. *Nature Materials*, 5:197–203, 2006.
- [101] J.-I. Nakamura, K. Murata, and K. Takahashi. Relation between carrier mobility and cell performance in bulk heterojunction solar cells consisting of soluble polythiophene and fullerene derivatives. *Applied Physics Letters*, 87:2005, 2005.
- [102] S. Scheinert and G. Paasch. Fabrication and analysis of polymer field-effect transistors. *Physica Status Solidi A*, 201:1263–1301, 2004.
- [103] C. Seoul and N.-H. Kim. Polymer light-emitting diodes based on poly(3-hexylthiophene). *Fibers and Polymers*, 1:25–31, 2000.
- [104] H. Sirringhaus, P.J. Brown, R.H. Friend, M.M. Nielsen, K. Bechgaard, B.M.W. Langeveld-Voss and A.J.H. Spiering, R.A.J Janssen, E.W. Meijer, P. Herwig, and D.M. de Leeuw. Two-dimensional charge transport in self-organized, high-mobility conjugated polymers. *Nature*, 401:685–688, 1999.
- [105] T. Erb, U. Zhokhavets, G. Gobsch, S. Raleva, B. Stühn, P. Schilinsky, C. Waldauf, and C.J. Brabec. Correlation between structural and optical properties of composite polymer/fullerene films for organic solar cells. *Advanced Functional Materials*, 15:1193–1196, 2005.
- [106] M. Reyes-Reyes, K. Kim, and D.L. Carroll. High-efficiency photovoltaic devices based on annealed poly(3-hexylthiophene) and 1-(3-methoxycarbonyl)-propyl-1-phenyl-(6,6) $C_{61}$  blends. *Applied Physics Letters*, 87:083506, 2005.
- [107] E. Wang, L. Wang, L. Lan, W. Zhuang, J. Peng, and Y. Cao. High-performance polymer heterojunction solar cells of a polysilafuorene derivative. *Applied Physics Letters*, 92:033307, 2008.

- [108] M.O. Reese, A.J. Morfa, M.S. White, N. Kopidakis, S.E. Shaheen, G. Rumbles, and D.S. Ginley. Pathways for the degradation of organic photovoltaic P3HT:PCBM based devices. *Solar Energy Materials & Solar Cells*, 92:746–752, 2008.
- [109] R. De Bettignies, J. Leroy, M. Firon, and C. Sentein. Accelerated lifetime measurements of P3HT:PCBM solar cells. *Synthetic Metals*, 156:510–513, 2006.
- [110] A.P. Yuen, J.S. Preston, A.-M. Hor, R. Klenker, E.Q. Macabebe, E.E. van Dyk, and R.O. Loutfy. Blend composition study of poly(3,3''-didodecylquaterthiophene)/[6,6]-phenyl C<sub>61</sub> butyric acid methyl ester solution processed organic solar cells. *Journal of Applied Physics*, 105:016105, 2009.
- [111] P. Vemulamada, G. Hao, T. Kietzke, and A. Sellinger. Efficient bulk heterojunction solar cells from regio-regular- poly(3,3''-didodecyl quaterthiophene)/PC<sub>70</sub>BM blends. *Organic Electronics*, 9:661–666, 2008.
- [112] G. Wantz, F. Lefevre, M.T. Dang, D. Laliberté, P.L. Brunner, and O.J. Dautel. Photovoltaic solar cells using poly(3,3''-didodecylquaterthiophene). *Solar Energy Materials & Solar Cells*, 92:558–563, 2008.
- [113] B.C. Thompson, B.J. Kim, D.F. Kavulak, K. Sivula, C. Mauldin, and J.M.J. Fréchet. Influence of alkyl substitution pattern in thiophene copolymers on composite fullerene solar cell performance. *Macromolecules*, 40:7425–7428, 2007.
- [114] A.J. Moulé, S. Allard, N.M. Kronenberg, A. Tsami, U. Scherf, and K. Meerholz. Effect of polymer nanoparticle formation on the efficiency of polythiophene based bulk-heterojunction solar cells. *The Journal Of Physical Chemistry C*, 112:12583–12589, 2008.
- [115] L. Lüer, H.-J. Egelhaaf, D. Oelkrug, G. Cerullo, G. Lanzani, B.-H. Huisman, and D. de Leeuw. Oxygen-induced quenching of photoexcited states in polythiophene films. *Organic Electronics*, 5:83–89, 2004.

- [116] M.S.A. Abdou and S. Holdcroft. Solid-state photochemistry of  $\pi$ -conjugated poly(3-alkylthiophenes). *Canadian Journal of Chemistry*, 73:1893–1901, 1995.
- [117] R.F. Salzman, J. Xue, B.P. Rand, A. Alexander, M.E. Thompson, and S.R. Forrest. The effects of copper phthalocyanine purity on organic solar cell performance. *Organic Electronics*, 6(5-6):242–246, 2005.
- [118] X. Yan, H. Wang, and D. Yan. An investigation on air stability of copper phthalocyanine-based organic thin-film transistors and device encapsulation. *Thin Solid Films*, 515:2655–2658, 2006.
- [119] P. Vanlaeke, A. Swinnen, I. Haeldermans, G. Vanhoyland, T. Aernouts, D. Cheyns, C. Deibel, J.D’Haen, P. Heremans, J. Poortmans, and J.V. Manca. P3HT/PCBM bulk heterojunction solar cells: Relation between morphology and electro-optical characteristics. *Solar Energy Materials & Solar Cells*, 90:2150–2158, 2006.
- [120] R.F. Bailey-Salzman, B.P. Rand, and S.R. Forrest. Near-infrared sensitive small molecule organic photovoltaic cells based on chloroaluminum phthalocyanine. *Applied Physics Letters*, 91:013508, 2007.
- [121] M. Brumbach, D. Placencia, and N.R. Armstrong. Titanyl phthalocyanine/ $C_{60}$  heterojunctions: Band-edge offsets and photovoltaic device performance. *The Journal of Physical Chemistry C*, 112:3142–3151, 2008.
- [122] J.D. Lee and H.B. Kim. Xerographic properties of metal/metal-free phthalocyanine composites in a double-layered photoconductor. *Korean Journal of Chemical Engineering*, 26:673–678, 2009.
- [123] D. Placencia, W. Wang, R.C. Shallcross, K.W. Nebesny, M. Brumbach, and N.R. Armstrong. Organic photovoltaic cells based on solvent-annealed, textured titanyl phthalocyanine/ $C_{60}$  heterojunctions. *Advanced Functional Materials*, 19:1913–1921, 2009.

- [124] M.Y. Chan, S.L. Lai, M.K. Fung, C.S. Lee, and S.T. Lee. Doping-induced efficiency enhancement in organic photovoltaic devices. *Applied Physics Letters*, 90:023504, 2007.
- [125] S.L. Lai, M.F. Lo, M.Y. Chan, C.S. Lee, and S.T. Lee. Impact of dye interlayer on the performance of organic photovoltaic devices. *Applied Physics Letters*, 95:153303, 2009.
- [126] T. Taima, J. Sakai, T. Yamanari, and K. Saito. Doping effects for organic photovoltaic cells based on small-molecular-weight semiconductors. *Solar Energy Materials & Solar Cells*, 93:742–745, 2009.
- [127] T. Taima, J. Sakai, T. Yamanari, and K. Saito. Realization of large open-circuit photovoltage in organic thin-film solar cells by controlling measurement environment. *Japanese Journal of Applied Physics*, 45:L995–L997, 2006.
- [128] A.K. Pandey and J.-M. Nunzi. Rubrene/fullerene heterostructures with a half-gap electroluminescence threshold and large photovoltage. *Advanced Materials*, 19:3613–3617, 2007.
- [129] V. Sundar, J. Zaumseil, V. Podzorov, E. Menard, R.L. Willett, T. Someya, M.E. Gershenson, and J.A. Rogers. Elastomeric transistor stamps: Reversible probing of charge transport in organic crystals. *Science*, 303:1644–1646, 2004.
- [130] R. O. Loutfy and C. K. Hsiao. Surface dye sensitization of an organic photoconductor: Photosensitization of phthalocyanine in schottky barrier cells. *Photographic Science and Engineering*, 24:155–160, 1980.
- [131] S. Seo, B.-N. Park, and P.G. Evans. Ambipolar rubrene thin film transistors. *Applied Physics Letters*, 88:232114, 2006.
- [132] M. Vogel, S. Doka, Ch. Breyer, M.Ch. Lux-Steiner, and K. Fostiropoulos. On the function of a bathocuproine buffer layer in organic photovoltaic cells. *Applied Physics Letters*, 89:163501, 2006.

- [133] Y. Hirose, A. Kahn, V. Aristov, P. Soukiassian, V. Bulovic, and S.R. Forrest. Chemistry and electronic properties of metal-organic semiconductor interfaces: Al, Ti, In, Sn, Ag, and Au on PTCDA. *Physical Review B*, 54:13748–13758, 1996.
- [134] P. Peumans and S.R. Forrest. Very-high-efficiency double-heterostructure copper phthalocyanine/C<sub>60</sub> photovoltaic cells. *Applied Physics Letters*, 79:126–128, 2001.
- [135] Y. Harada, T. Takahashi, S. Fujisawa, and T. Kajiwara. Application of photoelectron spectroscopy to the study of photochemical reactions of solids: photooxidation of rubrene (5,6,11,12-tetraphenylnaphthacene). *Chemical Physics Letters*, 62:283–286, 1979.
- [136] Y. Nakayama, S. Machida, T. Minari, K. Tsukagishi, Y. Noguchi, and H. Ishii. Direct observation of the electronic states of single crystalline rubrene under ambient condition by photoelectron yield spectroscopy. *Applied Physics Letters*, 93:173305, 2008.
- [137] D. Käfer and G. Witte. Growth of crystalline rubrene films with enhanced stability. *Physical Chemistry Chemical Physics*, 7:2850–2853, 2005.
- [138] F. Yang, R.R. Lunt, and S.R. Forrest. Simultaneous heterojunction organic solar cells with broad spectral sensitivity. *Applied Physics Letters*, 92:053310, 2008.
- [139] B.P. Rand, J. Xue, F. Yang, and S.R. Forrest. Organic solar cells with sensitivity extending into the near infrared. *Applied Physics Letters*, 87:233508, 2005.
- [140] R. Koeppe, O. Bossart, G. Calzaferri, and N.S. Sariciftci. Advanced photon-harvesting concepts for low-energy gap organic solar cells. *Solar Energy Materials & Solar Cells*, 91:986–995, 2007.

- [141] R. O. Loutfy, A. M. Hor, G. DiPaola-Baranyi, and C. K. Hsiao. Electrophotographic photoreceptors incorporating aggregated phthalocyanines. *Journal of Imaging Science*, 29:116–121, 1985.
- [142] R.O. Loutfy, A.M. Hor, and A. Rucklidge. Near infrared photoreceptor devices incorporating evaporated chloroindium phthalocyanine. *Journal of Imaging Science*, 31:31–37, 1987.
- [143] O. Okada and M.L. Klein. Molecular dynamics studies of titanyl phthalocyanine crystals. *Journal of the Chemical Society, Faraday Transactions*, 92:2463–2467, 1996.
- [144] L. Shen, G. Zhu, W. Guo, C. Tao, X. Zhang, C. Liu, W. Chen, S. Ruan, and Z. Zhong. Performance improvement of  $\text{TiO}_2$ /P3HT solar cells using CuPc as a sensitizer. *Applied Physics Letters*, 92:073307, 2008.
- [145] E.M.J. Johansson, A. Yartsev, H. Rensmo, and V. Sündstrom. Photocurrent spectra and fast kinetic studies of P3HT/PCBM mixed with a dye for photoconversion in the near-IR region. *Journal of Physical Chemistry C*, 113:3014–3020, 2009.
- [146] S.A. Jenekhe and S. Yi. Highly photoconductive nanocomposites of metallophthalocyanines and conjugated polymers. *Advanced Materials*, 12:1274–1278, 2000.
- [147] H. Yonehara, H. Etori, M.K. Engel, M. Tsushima, N. Ikeda, T. Ohno, and C. Pac. Fabrication of various ordered films of oxotitanium(iv) phthalocyanine by vacuum deposition and their spectroscopic behavior. *Chemistry of Materials*, 13:1015–1022, 2001.
- [148] J. Mizuguchi, G. Rihs, and H.R. Karfunkel. Solid-state spectra of titanylphthalocyanine as viewed from molecular distortion. *The Journal of Physical Chemistry*, 99:16217–16227, 1995.

- [149] T. Del Cano, V. Parra, M.L. Rodriguez, R.F. Aroca, and J.A. De Saja. Characterization of evaporated trivalent and tetravalent phthalocyanines thin films: different degree of organization. *Applied Surface Science*, 246:327–333, 2005.
- [150] H.S. Nalwa, T. Saito, A. Kakuta, and T. Iwayanagi. Third-order nonlinear optical properties of polymorphs of oxotitanium phthalocyanine. *The Journal of Physical Chemistry*, 97:10515–10517, 1993.
- [151] T. Saito, W. Sisk, T. Kobayashi, S. Suzuki, and T. Iwayanagi. Photocarrier generation processes of phthalocyanines studied by photocurrent and electroabsorption measurements. *The Journal of Physical Chemistry*, 97:8026–8031, 1993.
- [152] T. Tsuzuki, Y. Kuwabara, N. Noma, Y. Shirota, and M.R. Willis. Effect of morphology on photovoltaic properties of titanyl phthalocyanine. *Japanese Journal Of Applied Physics*, 35:L447–L450, 1996.
- [153] J.C. Conboy, E.J.C Olson, D.M. Adams, J. Kerimo, A. Zaban, B.A. Gregg, and P.F. Barbara. Impact of solvent vapor annealing on the morphology and photophysics of molecular semiconductor thin films. *Journal of Physical Chemistry B*, 102:4516–4525, 1998.
- [154] W. Wang, X. Li, S. Wang, and W. Hou. The preparation of high photosensitive TiOPc. *Dyes and Pigments*, 72:38–41, 2007.

# Appendix A

## Software Programs

### A.1 MATLAB code for solving equation (1.2)

```

close all;
clear all;
clc;

%%%%Cell Parameters%%%%
Rs=1;          %series resistance
Rsh=1e10;      %shunt resistance
A=0.079;       %active area in cm^2
Js=5e-9;       %reverse current in A/cm^2
Jpv = 10e-3;   %lossless shorted photocurrent,
               %integral of {incoming*EQE*dE}, in A/cm^2
n=1;
%%%%Cell Parameters%%%%

%%%%Numerical Parameters%%%%
h=0.0125;      %step size
V=-0.4:h:0.4;  %voltage sweep range
delta=1e-9;    %acceptable current error in iteration
%%%%Numerical Parameters%%%%

N=length(V);
J=ones(1,length(V));
Jsimp=ones(1,length(V));
error=ones(1,length(V));

```

```

itcount=ones(1,length(V));
i=0;
q=1.6e-19;
k=1.38e-23;
T=300;
coeff=n*q/k/T;

for i=1:N
    J(i)=-Jpv;
end
i=0;

for i=1:N
    m=0;
    while (error(i)>delta)
        m=m+1;
        bracket = coeff*(V(i)-J(i)*A*Rs);
        f=-1*Js*exp(bracket)+J(i)+J(i)*Rs/Rsh+Jpv+Js-V(i)/A/Rsh;
        fprime = 1+A*Rs*Js*coeff*exp(coeff*(V(i)-J(i)*A*Rs))+ Rs/Rsh;
        Jnext = J(i) - f/fprime; %Newton-Raphson
        error(i)=abs(Jnext-J(i));
        J(i)=Jnext;
    end
    itcount(i)=m;
end
i=0;
for i=1:N
    Jsimp(i)=(Jpv - Js*(exp(coeff*V(i)) -1))*-1;
end

for i=1:N
    Jma(i)=J(i)*1000;
end

```

## A.2 LabVIEW Virtual Instrument for EQE

Figure A.1 is a screenshot of the front panel of the LabVIEW virtual instrument used to acquire short circuit current for photovoltaic devices and reference optical power at tunable wavelengths. The source VI file is available electronically.

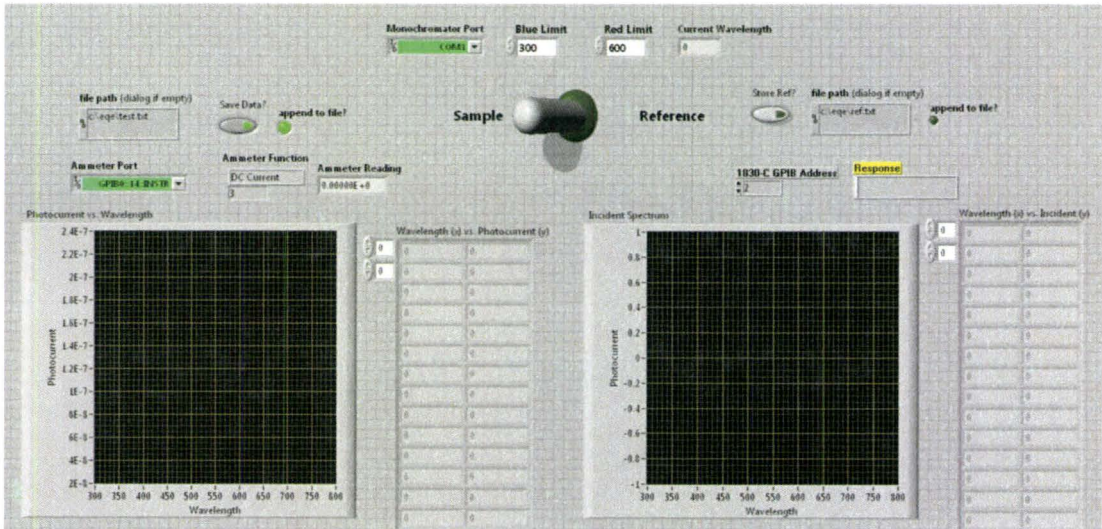


Figure A.1: Screenshot of LabVIEW program used to measure EQE

### A.3 LabVIEW Virtual Instrument for Long Term Decay

Figure A.2 is a screenshot of the front panel of the LabVIEW virtual instrument used to acquire I-V curves for photovoltaic devices at defined intervals of time. The source VI file is available electronically.

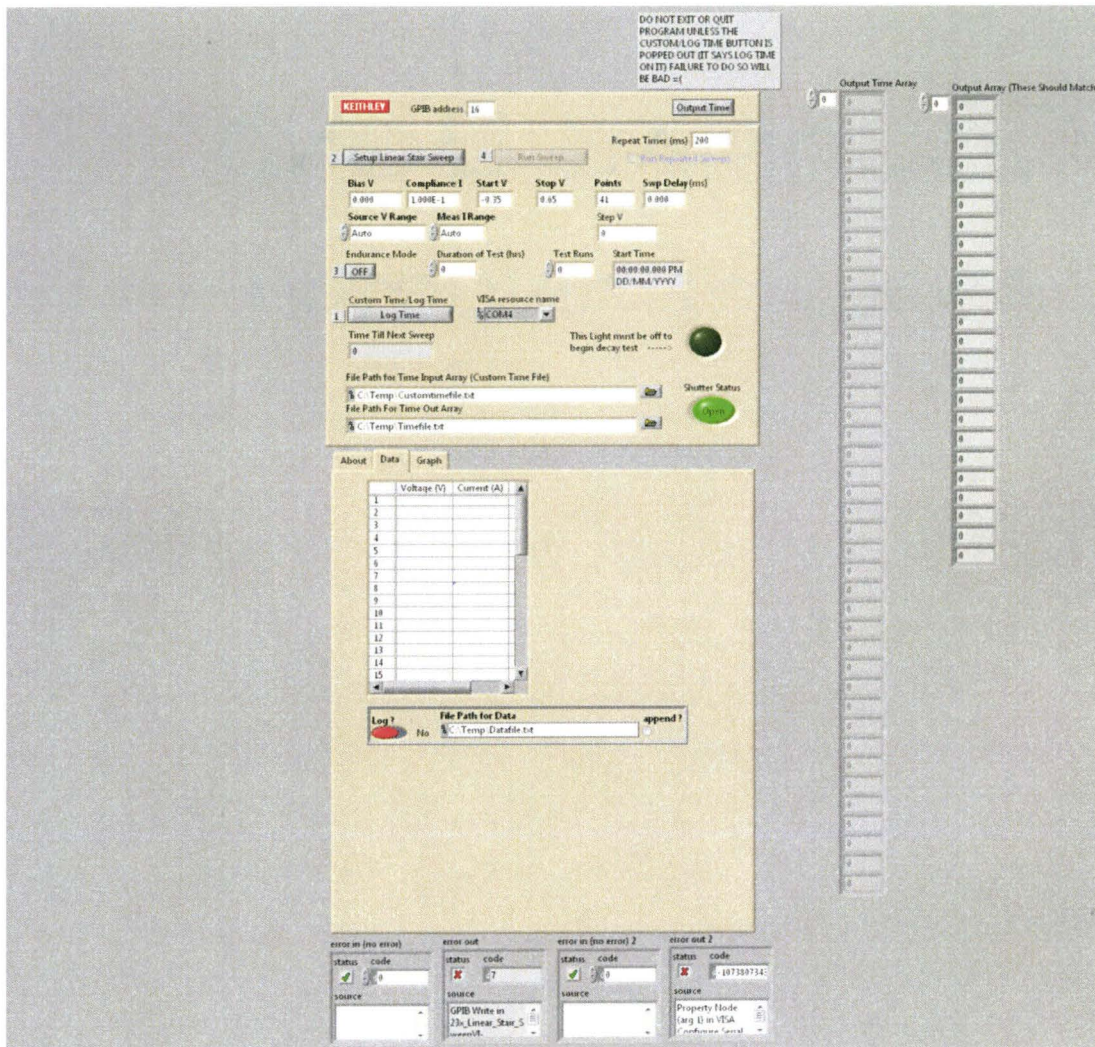


Figure A.2: Screenshot of LabVIEW program used to measure long term decay I-V

## A.4 MATLAB code for formatting decay data

```

clear all
close all
clc
%% Define Cell Area And Irradiation Power
Area = 0.069; %cm^2
Irr = 0.1; %W/cm^2
%% Import Data

%Define Filenames here please
Datafile = 'DecayData.txt';
Timefile = 'DecayTime.txt';
Exportfile = 'exportname';
importfile(Datafile);
importfile(Timefile);
DecayTime = transpose(DecayTime);
%% Definition of Data Length and Size Parameters

%Define parameter m here
%*** m is the number of swept points in a given voltage sweep***
m = 41;

%Define n here
%***** n is assumed to be the number of time points*****
n = length(DecayTime);

%% Array Formatting Variables

A = DecayData(:,1);
B = DecayData(:,2);
k = 0;

%***** j is your time counting variable *****
%***** i is your sweepwise counting variable*****

for j = 1 : n
    for i = 1 : m*2
        %***** Tabulate Voltages *****
        Voltage(j,i) = A(i+k);
        %***** Tabulate Currents *****
        Current(j,i) = B(i+k);
    end
end

```

```

    end
    % ***** Column Placement Tracker *****
    k = i+k;
end

%% Calculating the Voc

for j = 1 : n
    for i = m+2 : m*2
        Control1 = Current(j,i)*Current(j,i-1);
        if Control1 <= 0
            currentdiff = (Current(j,i)-Current(j,i-1));
            voltagediff = (Voltage(j,i)-Voltage(j,i-1));
            slope = currentdiff/voltagediff;
            intercept = Current(j,i)-slope*Voltage(j,i);
            Voc(j)=(-1*intercept)/slope;
            Rs(j) = inv(slope);
        end
    end
end

%% Calculating Isc and Jsc (non-normalized Isc)
for j = 1 : n
    for i = m+1 : m*2
        if Voltage(j,i) == 0
            Isc(j) = abs(Current(j,i));
            Jsc(j) = Isc(j)/Area;
        end
    end
end

%% Calculating the Maximum Power Point (Vmp and Jmp)
for j = 1 : n
    for i = m+2 : m*2-1
        P1 = abs(Voltage(j,i)*Current(j,i));
        P2 = abs(Voltage(j,i-1)*Current(j,i-1));
        P3 = abs(Voltage(j,i)*Current(j,i));
        P4 = abs(Voltage(j,i+1)*Current(j,i+1))
        if P1 > P2 && P3 > P4
            Vmp(j) = Voltage(j,i);
            Jmp(j) = abs(Current(j,i)/Area);
        end
    end
end

```

```

end
end

%% Calculating Fill Factor, Normalized Isc and Cell Efficiency
for j = 1 : n
    FF(j) = 100*(Vmp(j)*Jmp(j))/(Voc(j)*Jsc(j));
    NormIsc(j) = Isc(j)/max(Isc);
    eta(j) = (FF(j)*Voc(j)*Isc(j))/(Area*Irr);
end

%% Creating an Excel Friendly Output

M = zeros(n,10);
N = zeros(n+1,m*2);
N(1,:) = Voltage(1,:);
for j = 1 : n
    M(j,1) = DecayTime(j);
    M(j,2) = eta(j);
    M(j,3) = FF(j);
    M(j,4) = Voc(j);
    M(j,5) = Jsc(j);
    M(j,6) = NormIsc(j);
    M(j,7) = Isc(j);
    M(j,8) = Vmp(j);
    M(j,9) = Jmp(j);
    M(j,10) = Rs(j);
    if j > 1
        for i = 1 : m*2
            N(j,i) = Current(j,i);
        end
    end
end
end

xlswrite(Exportfile, M, 'Cell Data','A2');
XlsWrite(Exportfile, N, 'Voltage Sweeps','B1');

```

